

On the Selective Synchronization of Some Dynamical Systems that Exhibit Chaos

Dumitru N. Deleanu

Maritime University of Constanta, 104, Mircea cel Batran street, 905600,
Constanta, Romania
(E-mail: dumitrudeleanu@yahoo.com)

Abstract. Over the last two decades, a considerable number of methods have been proposed for synchronizing chaotic systems. Most of them have concentrated on studying continuous synchronization. Different from this, impulsive synchronization requires small synchronizing impulses which are sampled from the state variables of the drive system at discrete moments. This drastically reduces the amount of information transmitted from the master system to the slave one, which makes this approach more attractive in chaos-based secure communication and other real-life applications. In the paper, we present and apply an efficient impulsive synchronization scheme, called selective synchronization, to selectively use only those time periods of driving signals which strong synchronizing effect to the driven system. By doing this, one can synchronize chaotic systems which cannot be synchronized by continuous schemes under similar conditions. Numerical examples are given to illustrate the effectiveness of the proposed scheme.

Keywords: Selective synchronization, Conditional Lyapunov exponents, Discrete and continuous-time chaotic systems.

1 Introduction

Nowadays, chaos synchronization is a topic of huge interest in the nonlinear science, owing to its observation in a large variety of phenomena of different nature or to its various potential applications (Feki [3], Pecora and Carroll[11], Womelsdorf and Fries[12], Yang and Chua[13]). Many reviews on chaos synchronization are currently available (Boccaletti *et al.*[1], Mosekilde *et al.*[9]). A considerable number of methods have been proposed for synchronizing chaotic systems. The most widely used techniques are continuous synchronization schemes, including Pecora-Carroll method, back-stepping design technique, active and adaptive synchronization schemes, sliding mode control technique, and so on (Chen and Lu[2], Kanishi *et al.*[6], Zhang[14]). In all these approaches, two or more chaotic systems are coupled to each other continuously such that the synchronization errors can be controlled for converge to zero.

7th CHAOS Conference Proceedings, 7-10 June 2014, Lisbon Portugal

C. H. Skiadas (Ed)

© 2014 ISAST



More recently, experimental and numerical evidences showed that synchronization can be achieved using intermittent coupling. Two approaches, impulsive and selective synchronization, have attracted the attention of the researchers in the field. In an impulsive synchronization scheme only samples of state variables, called synchronization impulses, are used to synchronize the chaotic systems. The bandwidth or time slot needed to transmit synchronization signals dramatically reduced in impulsive synchronization when compared to continuous synchronization (Itoh *et al.*[4], Panas *et al.*[10]). In a selective synchronization scheme, the synchronizing signal is chosen in the time periods when the Lyapunov exponents of variational synchronization error system are negative. Since only driving signals in the time periods when synchronization error can be reduced are selected and those in the time periods when the synchronization error can be increased are not used, the selective synchronization scheme are capable to achieve synchronization even in the cases when the continuous synchronization schemes fail to work (Itoh *and al.*[5]).

Because there is little work about this kind of synchronization, the aim of the present paper is to bring additional numerical evidences to those existing in the literature. In order to prove that selective scheme can synchronize chaotic systems which cannot be synchronized by a continuous approach under similar conditions, we numerically simulated the two-dimensional chaotic Lorenz map and a three-dimensional flow, which has a broad spectrum of chaotic behaviors with the Lorenz and the Chen systems as the extremes of the spectrum.

2 Selective Synchronization of Chaotic Systems: Basic Idea.

In this section, we briefly discuss the selective synchronization of two identical chaotic systems (hereafter, called master and slave) by using notations specific to a discrete system only.

Suppose that the state variables of the dynamical system can be separated into two parts, $\mathbf{x}(n)$ and $\mathbf{y}(n)$. The general form of the master system is as follows

$$^{(m)} \begin{cases} \mathbf{x}_m(n+1) = \mathbf{f}(\mathbf{x}_m(n), \mathbf{y}_m(n)) \\ \mathbf{y}_m(n+1) = \mathbf{g}(\mathbf{x}_m(n), \mathbf{y}_m(n)) \end{cases} \quad (1)$$

where $\mathbf{x} \in R^p$ and $\mathbf{y} \in R^q$ are the state variables, while \mathbf{f} and \mathbf{g} are continuous nonlinear functions. Consider now that the samples of the state variables \mathbf{y}_m are sent to the slave system. This happens when the master signal is detected to be more likely to decrease the synchronization errors. For these time periods, the slave system is governed by

$$^{(s_1)} \begin{cases} \mathbf{x}_s(n+1) = \mathbf{f}(\mathbf{x}_s(n), \mathbf{y}_s(n)) \\ \mathbf{y}_s(n+1) = \mathbf{y}_m(n) \end{cases} \quad (2)$$

while for the time periods when the two systems evolve independently the slave system is described by

$$({s}_2) \quad \begin{cases} \mathbf{x}_s(n+1) = \mathbf{f}(\mathbf{x}_s(n), \mathbf{y}_s(n)) \\ \mathbf{y}_s(n+1) = \mathbf{g}(\mathbf{x}_s(n), \mathbf{y}_s(n)) \end{cases} \quad (3)$$

The variational system are given by

$$\mathbf{u}(n+1) = \frac{\partial \mathbf{f}}{\partial \mathbf{x}}(\mathbf{x}(n), \mathbf{y}(n)) \cdot \mathbf{u}(n) \quad (4)$$

or by

$$\begin{bmatrix} \mathbf{u}(n+1) \\ \mathbf{v}(n+1) \end{bmatrix} = \begin{bmatrix} \frac{\partial \mathbf{f}}{\partial \mathbf{x}}(\mathbf{x}(n), \mathbf{y}(n)) & \frac{\partial \mathbf{f}}{\partial \mathbf{y}}(\mathbf{x}(n), \mathbf{y}(n)) \\ \frac{\partial \mathbf{g}}{\partial \mathbf{x}}(\mathbf{x}(n), \mathbf{y}(n)) & \frac{\partial \mathbf{g}}{\partial \mathbf{y}}(\mathbf{x}(n), \mathbf{y}(n)) \end{bmatrix} \quad (5)$$

where $\mathbf{u}(n) = \mathbf{x}_m(n) - \mathbf{x}_s(n)$ and $\mathbf{v}(n) = \mathbf{y}_m(n) - \mathbf{y}_s(n)$. According to Pecora and Carroll, the master and slave systems will synchronize if all the conditional Lyapunov exponents of the variational system are negative.

Practically, the master signal will be transmitted to the slave system if all the eigenvalues of the variational system have modulus smaller than unity (for maps) or have negative real parts (for flows).

3 Systems description and numerical simulations

As models for our numerical study on selective synchronization we consider here two typical nonlinear dynamical systems which exhibit chaotic behavior. They are as follows:

3.1. Lorenz map

The Lorenz discrete-time system is given by difference equations

$$x(n+1) = (1+ab)x(n) - b x(n)y(n), \quad y(n+1) = (1-b)y(n) + b x^2(n) \quad (6)$$

with a and b parameters. This system is chaotic for $a=1.05$ and $b=0.75$, as shown in Figure 1(d) (its maximal Lyapunov exponent is $\lambda_{\max} = 0.258$). This map was iterated for 32,000 times and the first 2,000 iterations were discarded. We transmitted impulses sampled from y state variable of the master system to the slave system every time the condition $|1+ab-b y_m(n)| < d$ was fulfilled.

The variable d was used as a controlling parameter indicating the percentage of the used driving signal (see Figure 1(b)). It was found that the synchronization error has vanished not only for $d = 1$, but for $d \in [0.495, 1.795]$. With just few

exceptions, encountered at the borders of this interval, the conditional Lyapunov exponent (CLE) was negative, as depicted in Figure 1(a). There was a small range, $d \in [0.495, 0.511]$, where desynchronization bursts were presented although the CLE was negative. The logarithm of the synchronization time (in number of iterations) is reported in Figure 1(c). The criterion for synchronization was selected to be $|x_m(n) - x_s(n)| + |y_m(n) - y_s(n)| < \varepsilon$, with $\varepsilon = 10^{-6}$. It is worth noting that just 18% of driving signal was used for synchronization in the case $d = 0.511$.

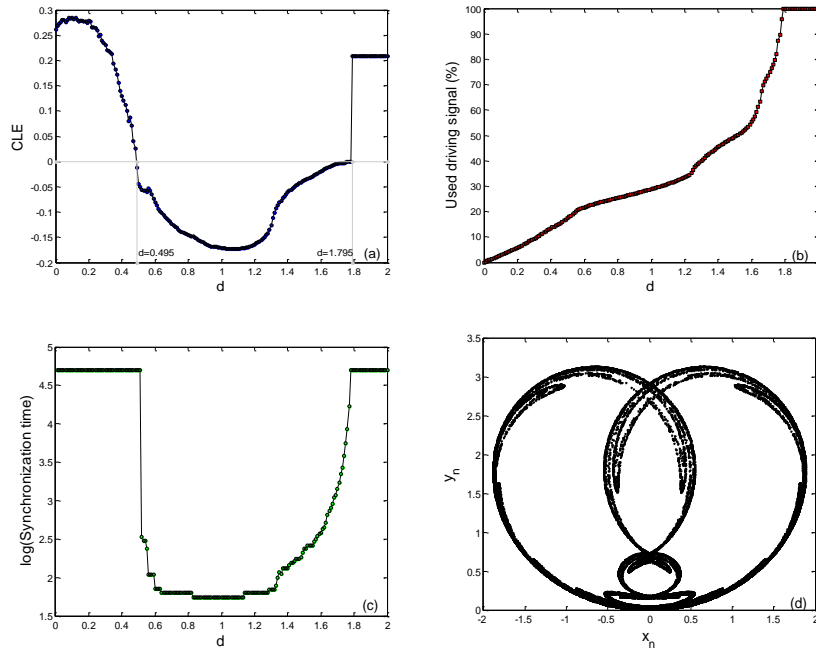


Fig. 1. Selective synchronization of two identical Lorenz maps
 a) Conditional Lyapunov exponent versus d ; b) Used driving signal versus d ;
 c) Logarithm of the synchronization time versus d ; d) (x, y) phase-plane.

For $d = 1.4$, the identical synchronization was achieved in 133 iterations, using 45/55% of driving signal (see Figure 2(a)). A series of simulations was performed to verify if the above-mentioned percentage can be reduced by keeping the two systems in a synchronized state.

To do this, we first switched-off the connection between master and slave systems every time a random sub-unitary variables had values greater than 0.75. Sometimes, the two systems were synchronized and other times they run independently, as shown in Figures 2(b) and 2(c). The unused driving signals are represented by yellow color. Secondly, we cut the driving signal in the range

$d \in [1, 1.4]$ by maintaining the restrictive condition on the random variable, and succeeded to synchronize the two systems using just about 36% of driving signal (see Figure 2(d)).

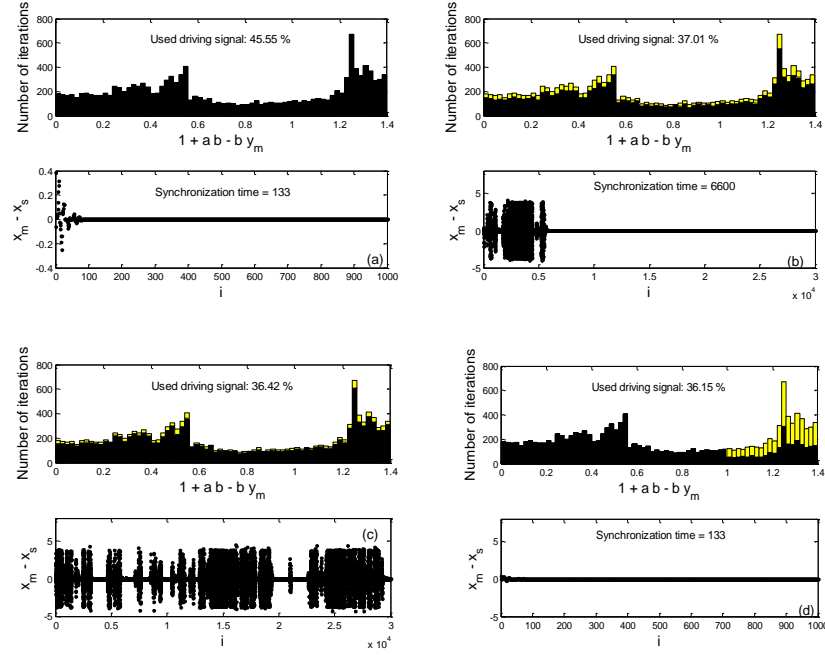


Fig. 2. Selective synchronization of two identical Lorenz maps for $d=1.4$

3.2. The unified chaotic system

Recently, Lu *et al.* [7, 8] found a unified three-dimensional continuous dynamical system that has a broad spectrum of chaotic behaviors with the Lorenz and Chen systems as two extremes cases. It is described by

$$\begin{cases} \dot{x} = (25\alpha + 10)(y - x) \\ \dot{y} = (28 - 35\alpha)x - xz + (29\alpha - 1)y, \quad \alpha \in [0, 1] \\ \dot{z} = xy - \frac{8 + \alpha}{3}z \end{cases} \quad (7)$$

When $\alpha \in [0, 0.8)$, the system (7) is called the generalized Lorenz system (for $\alpha = 0$, it is the Lorenz system); when $\alpha = 0.8$, it becomes the generalized Lu system; when $\alpha \in (0.8, 1]$, the system (7) is called the generalized Chen system

(for $\alpha = 1$, it is the Chen system). Some of these situations are plotted in Figure 3.

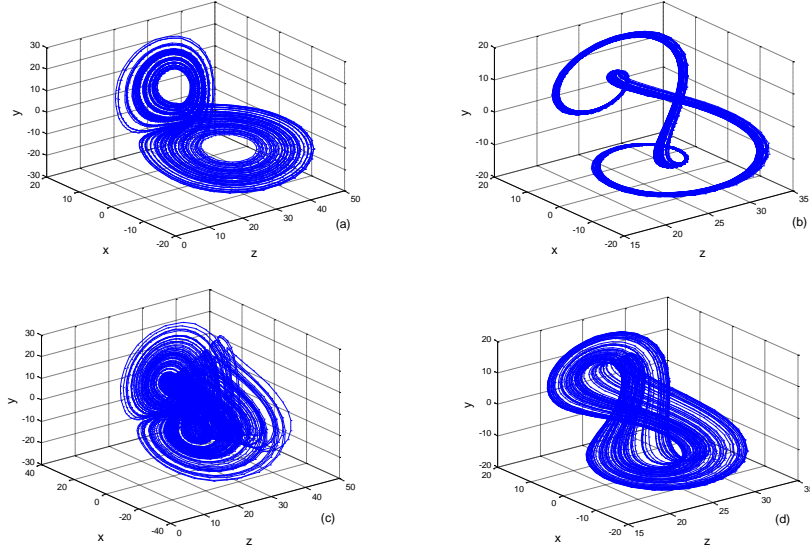


Fig. 3. The unified chaotic attractor. a) $\alpha = 0$, b) $\alpha = 0.58$, c) $\alpha = 0.8$, d) $\alpha = 1$

As α changes continuously from 0 to 1, the resulting system (7) remains to be chaotic, as illustrated in Figure 4 (left panel), where only the first and the third Lyapunov exponents are plotted (the second is equal to zero).

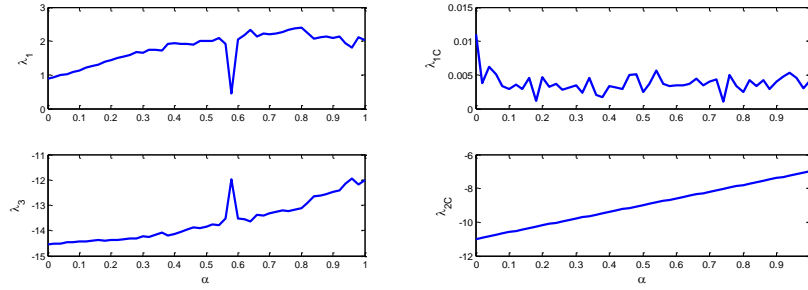


Fig. 4. Left: The dependence of the first and the third Lyapunov exponents of the unified system (7) on α ; Right: The dependence of the first and the third conditional Lyapunov exponents of the unified system (7) on α .

To synchronize two identical unified systems, we transmitted impulses sampled from z state variable of the master system to the slave system every time the condition $z_m > d$ was verified. The variable d acts again as a controlling parameter. For $d = 27 - 6\alpha$, the eigenvalues of the variational system have negative real parts. As in the case of Lorenz map, a continuous transmission of driving signal cannot synchronize the two systems because the maximal conditional Lyapunov exponent is greater than zero (see Figure 4 (right panel)).

Table 1. Synchronization time and used driving signal for a successful selective synchronization of two unified chaotic systems (7)

| α | d | Used driving signal (%) | Synchronization time |
|----------|---------|-------------------------|----------------------|
| 0.0 | 19.5–24 | 58.6–41.6 | 18.9–86.9 |
| 0.58 | 17.5–26 | 87.9–24.1 | 60–98.9 |
| 0.8 | 14–20.5 | 90.1–69.3 | 23.3–78 |
| 1.0 | 22.5–24 | 58.3–48.0 | 47.6–68.1 |

First, we focused our attention on the selective synchronization of two identical systems (7) for $\alpha \in \{0.0, 0.58, 0.8, 1.0\}$. The case $\alpha = 0.58$ was selected because it presents the smallest maximal Lyapunov exponent, as shown in Figure 4(a).

In every situation, we succeeded to find a range for d so the two systems evolve in a synchronized manner. The plots for synchronization time and used driving signal versus d are given in Figure 5. Additionally, some relevant values for these parameters are presented in Table 1.

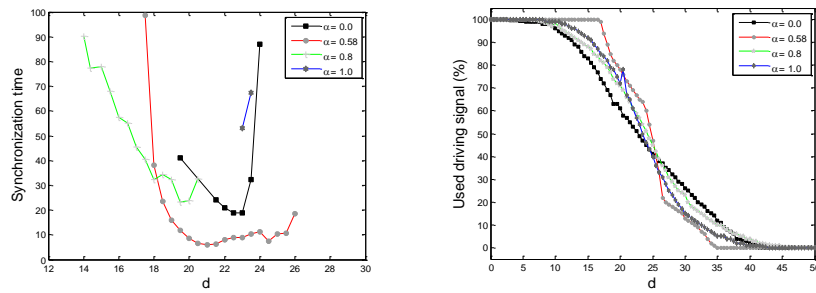


Fig. 5. Selective synchronization of two unified chaotic systems (7).

Synchronization time (left panel) and used driving signal (right panel) versus d for selected α .

Secondly, we chose 25 equidistant values for α between 0 and 1, and repeated the previous numerical investigation. The obtained results are reported in Figure 6, where ranges for d and the used driving signal are displayed for every considered α , if the synchronization was realized.

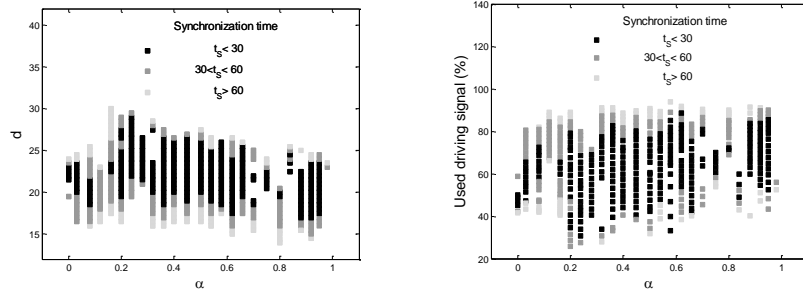


Fig. 6. Selective synchronization of two unified chaotic systems (7). d (left panel) and used driving signal (right panel) versus α

Finally, we settled $\alpha = 0.0$ and wanted to find the maximal amount of information needed to be transferred to the slave system so the synchronization can be achieved. For $d = 23$, the two systems synchronized in 18.8 s by using 45.2% of driving signal (see Figure 7(a)). For $d > 27$, both the eigenvalues of the variation system have negative real parts. We tried to discard so many possible driving signals points in the range $z_m \in [23, 27]$, by maintaining the two systems in a synchronized state. The result was that more than 80% of the driving signals may be neglected without destroying the synchronization (see Figure 7(b)).

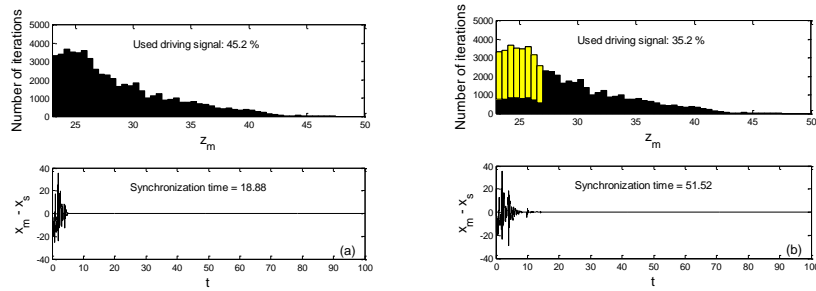


Fig. 7. Selective synchronization of two unified chaotic systems (7) for $\alpha = 0.0$.

Conclusions

In the paper we have shown that chaotic systems can be synchronized by using a selective scheme, where only those driving signals with strong synchronizing effect are sent to the slave system. Two important merits of this approach, highlighted by properly chosen examples, are as follows:

- a) The amount of information transmitted from the master system to the slave system is significantly reduced, which makes the scheme more safe and efficient in some sort of applications like secure communications;
- b) It can synchronize chaotic systems that cannot be synchronized by a continuous scheme under similar conditions.

We also discussed the performance of selective synchronization scheme from the viewpoints of synchronization time and used driving signal. Computer simulation results, based on Lorenz chaotic map and on a unified continuous chaotic system which has the Lorenz and Chen systems as extreme cases, are given to demonstrate the effectiveness of the selective synchronization scheme.

References

1. S. Boccaletti, J. Kurths, G. Osipov, D.L. Valledares and C.S. Zhou. The synchronization of chaotic systems. *Physics Reports*, 366, 1-101, 2002.
2. S.H. Chen and J. Lu. Synchronization of an uncertain unified system via adaptive control. *Chaos, Solitons and Fractals*, 14, 643-647, 2002.
3. M. Feki. An adaptive chaos synchronization scheme applied to secure communication. *Chaos, Solitons and Fractals*, 18, 141-148, 2003.
4. M. Itoh, T. Yang and L.O. Chua. Experimental study of impulsive synchronization of chaotic and hyperchaotic circuits, *Int. J. of Bifurcation and Chaos*, 9, 1, 1393-1424, 1999.
5. M. Itoh, T. Yang and L.O. Chua. Conditions for impulsive synchronization of chaotic and hyperchaotic systems. *Int. J. of Bifurcation and Chaos*, 11, 2, 551-560, 2001.
6. K. Kanishi, M. Hirai and H. Kokame. Sliding mode control for a class of chaotic systems. *Physical Letters A*, 245, 511-517, 1998.
7. J. Lu, G. Chen and S. Zhang. Controlling in between the Lorenz and the Chen systems. *Int. J. of Bifurcation and Chaos*, 12, 6, 1417-1422, 2002.
8. J. Lu, G. Chen, S. Zhang and S. Celikovsky. Bridge the gap between the Lorenz system and Chen system. *Int. J. of Bifurcation and Chaos*, 12, 11, 2917-2926, 2002.
9. E. Mosekilde, Y. Maistrenko and D. Postnov. *Chaotic Synchronization. Application to living system*. World Scientific, New Jersey, 2002.
10. A.I. Panas, T. Yang and L.O. Chua. Experimental results of impulsive synchronization between two Chua's circuits. *Int. J. of Bifurcation and Chaos*, 8, 3, 639-644, 1998.
11. L.M. Pecora and T.L. Carroll. Synchronization in chaotic systems. *Physical Review Letters*, 64, 8, 821-824, 1990.

12. T. Womelsdorf and P. Fries. The role of neuronal synchronization in selective attention. *Current Opinion in Neurobiology*, 17, 1-7, 2007.
13. T. Yang and L.O. Chua. Application of chaotic digital code-division multiple access (CDMA) to cable communication systems. *Int. J. of Bifurcation and Chaos*, 8, 8, 1657-1669, 1998.
14. Y. Zhang. Controlling Lu system using back-stepping design. *Chaos, Solitons and Fractals*, 15, 897-904, 2003.

Impact evaluation of third-order dispersion in strongly DM soliton interactions

Francisco J. Diaz-Otero¹, Pedro Chamorro-Posada², Francisco J. Fraile-Peláez³

^{1,3} Departamento de Teoría de la Señal y Comunicaciones, Universidad de Vigo ETSI Telecomunicación, Campus Universitario s/n 36310 Vigo, Spain. (phone:+34-986-818671; e-mail: fjdiaz@com.uvigo.es).

² Departamento de Teoría de la Señal y Comunicaciones e Ingeniería Telemática Universidad de Valladolid, ETSI Telecomunicación, Campus Miguel Delibes s/n 47011 Valladolid, Spain; e-mail: pedcha@tel.uva.es.

Abstract: We study the interaction between a pair of gaussian pulses by means of a variational approximation propagating in a strongly dispersion managed (DM) optical fiber with periodically spaced lumped amplification. Results are studied for a prototypical model with two neighboring pulses equally spaced in time. By means of the ordinary differential equations (ODEs) obtained through the variational method and its associated parameters, it is shown that the location of the amplifier significantly affects the energy enhancement and pulsewidth evolution of each DM pulse. Besides, suitably positioning the amplifier can lead to extend the interaction distance between both pulses. Moreover, for higher bit-rate transmission systems we need to include the effect of third order dispersion (TOD) in the variational model. We find that TOD usually reduces the interaction distance between both solitons. However, there is a net increase in the interaction distance as we place an amplifier at specific positions of the dispersion map period for some values of the dispersion difference. We study this result in terms of energy enhancement and pulsewidth evolution and, finally, compare the variational approximation predictions for the single-channel systems with direct simulations of the underlying partial differential equations and find an excellent agreement.

Keywords: Optical solitons, Dispersion management, variational approximation, third order dispersion, optical fiber communication

1. Introduction

It is well known that periodically alternating the sign of the group-velocity dispersion along an optical fiber, a technique called Dispersion Management (DM), can extend greatly the transmission distance and has become a fundamental technology for high-speed soliton transmission in long-haul optical communication links [1], [2]. The potential offered by this technique comes from the fact that there is an energy enhancement compared with that of the conventional soliton [3], [4], [5], [6]. This periodic compensation of the group-

7th CHAOS Conference Proceedings, 7-10 June 2014, Lisbon Portugal
C. H. Skiadas (Ed) □

©2014 ISAST



velocity dispersion in a long fiber-optic telecommunication link raises the signal-to-noise ratio (SNR) and reduces the noise induced timing jitter and four wave mixing (FWM).

However, there are several system penalties associated with DM propagation in a single frequency channel. One of the most important arises from a large pulse stretching accompanied with an overlap of neighboring pulses that causes a reduction in the interaction distance [7]. Besides, as transmission bit rates move to higher standards of the synchronous digital hierarchy (SDH), the impact of third order dispersion (TOD) effects becomes increasingly important, even for a single channel, due to the even greater reduction of pulse width [8, 9]. Now, in this work, we extend previous analyzes of the effect of the TOD on the interaction length [10] to the case where lumped amplification is present in the transmission link and compare the results with those mentioned in terms of energy enhancement and pulsewidth evolution.

Our study is based in an ODE model obtained by means of a variational method [11] which takes into account third order dispersion [12]. Using a set of ODEs which capture the general evolution of the main parameters of each pulse in an approximate manner, with different amplifier locations and considering only two pulses transmitted in the system, we obtain conditions for stable pulse transmission under strong dispersion management regime, in terms of energy, chirp and pulsewidth. After that, we extend the analysis taking into account interaction distances between two pulses with and without TOD and with different amplifier locations. Finally, these results are verified versus direct numerical simulations.

Previous results found that the amount of interaction between stretching pulses is dependent on the amplifier position in an unit cell of the dispersion map [13]. Now we find that, besides the enhancement of interaction distance due to a careful election in the location of the amplifier, there is also an improve in the collapse distance for certain values of averaged TOD along the line.

2. Variational approximation

We analyze a DM optical fiber made up of alternating segments of equal length with normal and anomalous dispersion. We insert lumped amplifiers in different locations within the unit cell of the dispersion map with intervals the same as the period of the variation of the dispersion. These amplifiers are moved inside the unit cell in each simulation in order to examine the effect of changing their position in terms of energy enhancement and pulsewidth evolution, taking into account the effect of third order dispersion. The normalised complex envelope of two adjacent optical pulses, where $l = 1, 2$, $u(z, t) = u_1(z, t) + u_2(z, t)$, evolves in a periodic dispersion map, neglecting the phase-dependent effects and taking

7th CHAOS Conference Proceedings, 7-10 June 2014, Lisbon Portugal

C. H. Skiadas (Ed) □

©2014 ISAST



into account only the SPM and XPM induced by the Kerr effect, according to a system of two coupled generalised NLS equations

$$j \frac{\partial u_l}{\partial Z} + \frac{1}{2} D(Z) \frac{\partial^2 u_l}{\partial T^2} + S(Z) |u_l|^2 u_l + 2 S(Z) |u_{3-l}|^2 u_l - j \delta \frac{\partial^3 u_l}{\partial T^3} = 0.$$

$$l = 1, 2.$$

where $\delta(Z)$ models the effect of TOD and $D(Z)$, T and Z represent the fibre dispersion, the retarded time and propagation distance, respectively. $S(Z)$ accounts for the effects of gain and loss. $D(Z)$ defines the dispersion map and is a periodic function of the propagation distance with alternating values D_+ and D_- in sections of fiber with lengths Z_+ and Z_- and average value D_{av} . $\Delta D = D_+ - |D_-|$ and $Z_0 = Z_+ + Z_-$ is the map period. TOD effects arise from $d^3 \beta / d\omega^3$ where $\beta(\omega)$ is the mode propagation constant at frequency ω . For the sake of simplicity, we assume a constant value for the TOD parameter δ . Numerical simulations performed for different values of δ periodically changing with Z have shown that the relevant parameter is its average value. We also assume that interaction behavior is dictated by self-phase modulation (SPM) and cross-phase modulation (XPM) effects alone. This model is only valid in the strong dispersion management regime ($|\Delta D| > 10$) due to the fast oscillating movement of both pulses.

The variational method [11] permits to reduce the full complexity of the generalized NLS equation to that of system of ODEs which capture the most relevant features of the evolving solutions in an approximate manner. We assume that under strong dispersion management ($\Delta D Z_0 > 10$; $\Delta D Z_0 < 45$) the pulse is well approximated by a Gaussian shape [15] and use the ansatz

$$u_l(Z, T) = \sqrt{\frac{E_l}{\sqrt{\pi}}} \sqrt{p_l(Z)} \exp \left[\frac{-p_l(Z)^2}{2} (1 - j C_l(Z)) (T - T_l(Z))^2 - j \omega_l(Z) (T - T_l(Z)) + j \theta_l(Z) \right]$$

where E_l , $p_l(Z)$, $C_l(Z)$, $\omega_l(Z)$, $T_l(Z)$, $\theta_l(Z)$ are the energy, inverse pulse width, linear chirp, centre frequency, centre position and phase of the pulse, respectively.

Skipping routine details, we obtain the equations of motion [12]

7th CHAOS Conference Proceedings, 7-10 June 2014, Lisbon Portugal
C. H. Skiadas (Ed) □

©2014 ISAST



$$\begin{aligned}
\frac{dp_l}{dZ} &= -C_l p_l^3 (D - 6\delta\omega_l), \\
\frac{dC_l}{dZ} &= (1 + C_l^2) p_l^2 (D - 6\delta\omega_l) - \frac{p_l S(Z)}{\sqrt{2\pi}} (E_l \\
&\quad + 2E_{3-l} p_l^3 (1 - \tau_l^2) \exp\left(\frac{-\tau_l^2}{2}\right)), \\
\frac{dT_l}{dZ} &= -D\omega_l + 3\delta\omega_l^2 + \frac{3}{2} \delta(1 + C_l^2) p_l^2, \\
\frac{d\omega_l}{dZ} &= \frac{2E_{3-l} S(Z)}{\sqrt{2\pi}} \tau_l p_l^2 \exp\left(\frac{-\tau_l^2}{2}\right). \quad \square
\end{aligned}$$

where

$$\begin{aligned}
\tau_l &= P \Delta T_l, \\
\Delta T_l &= T_l - T_{3-l}, \\
P &= \frac{\sqrt{2} p_l p_{3-l}}{\sqrt{p_l^2 + p_{3-l}^2}}. \quad \square
\end{aligned}$$

And

$$\begin{aligned}
S(Z) &= g_0 \exp(-2\Gamma|Z, Z_0|) \\
g_0 &= \frac{2\Gamma Z_a}{1 - \exp(-2\Gamma Z_a)}.
\end{aligned}$$

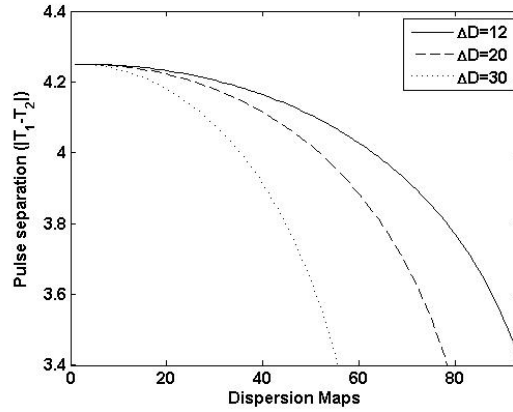


Fig. 1. Pulse separation versus transmission distance for three different values of ΔD . The amplifiers are located at $Z_a = 0$, $Z_+ = Z_- = 0.5$ and $D_{av} = 1$ with initial pulse separation $|T_1 - T_2| = 4.25$.



3. Results and discussion

The main effect observed in the above equations, in terms of mutual interaction between both pulses, is the change in the pulse frequency, which is translated to the time shift via the dispersion. Besides, considering strong dispersion management, the interaction is independent of the initial phase difference. The mechanism of this mutual interaction can be described as follows, taking into account only the XPM effect during the collision: The simultaneous presence of two pulses produces a shift of their center frequencies, caused by XPM, and a corresponding displacement of their center positions due to group velocity dispersion in the transmission medium. These two closely adjacent pulses attract each other and collide. We will measure this effect in terms of the interaction distance (Z_i) defined as $|T_1 - T_2| = 0.5$.

We know that TOD induces two main effects in DM soliton propagation: an asymmetric distortion in the shape of the pulse and energy radiation. For the sake of simplicity we have neglected these effects in this variational approximation. As we introduce TOD effects in the ODE system described, the evolution equations derived in the previous section reveal a correction of the effective dispersion as $D_{eff} = D - 6\delta\omega$ and a change in the transverse velocity of each pulse as $V_l = -D\omega_l + 3\delta\omega_l^2$. With the values obtained in these equations, we study the effect of pulse separation, pulse position evolution and energy enhancement in order to explain the changes in interaction distance versus the amplifier location, as we change the amplifier location and consider TOD effects.

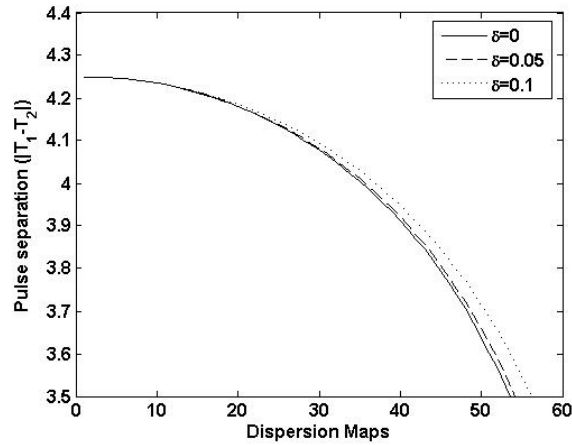


Fig. 2. Pulse separation versus transmission distance for three different values of δ . The amplifiers are located at $Z_a = 0$, $Z_+ = Z_- = 0.5$ and $D_{av} = 1$ with initial pulse separation $|T_1 - T_2| = 4.25$.



3.1 Pulse separation

In the ODE equations obtained, and demanding that the pulse's width returns to the original values after passing one DM period for stationary pulse evolution, we set $E_2 = 0$ and solve the ODES keeping only the results of the parameters for the $l = 1$ pulse. We consider $p(0) = 1$ pulses launched in a normalized map with $Z_+ = Z_- = 0.5$ and $D_{av} = 1$ with initial pulse separation $|T_1 - T_2| = 4.25$.

With those values we can obtain a complete picture of the four main parameters of the pulse: pulsewidth evolution, chirp and center position. In Figure 1 we can see an example of pulse separation in terms of interaction distance, versus transmission distance. The values of dispersion difference are $\Delta D = 12, 20, 30$ in the strong dispersion management regime. The amplifiers are located in the middle of the dispersion cell unit. The input pulse energy of a conventional soliton with the same average dispersion $D_{av} = 1$ is $E_0 = 2.5086$ and the energy of the DM solitons with $\Delta D = 12, 20, 30$ are $E_0 = 2.6646, 2.9128, 3.3947$. We can see that the interaction distance, at which the pulse separation becomes lower than the half-FWHM pulse width ($|T_1 - T_2| \leq 0.5$) decreases significantly as ΔD grows, mainly because a large amount of overlap between the pulses when they stretch. If we add TOD to the equations and find the interaction distance for a fixed dispersion difference $\Delta D = 30$, we find that for some values of δ there is a significant increasing in the interaction distance.

In Figure 2 we can see that the interaction distance grows from $Z_i = 54$ with $\delta = 0$ to $Z_i = 57$ with $\delta = 0.1$. This occurs mainly due to an enhancement in the displacement of the center position of both pulses. This effect is shown in Figure 3. Numerical analysis obtained by the numerical integration of the full PDE are shown in Figure 4, showing good agreement with our variational approximation. Finally, in Figure 5 we can see the stable propagation of a single pulse with a lumped amplifier located at the middle of the dispersion map period with TOD.



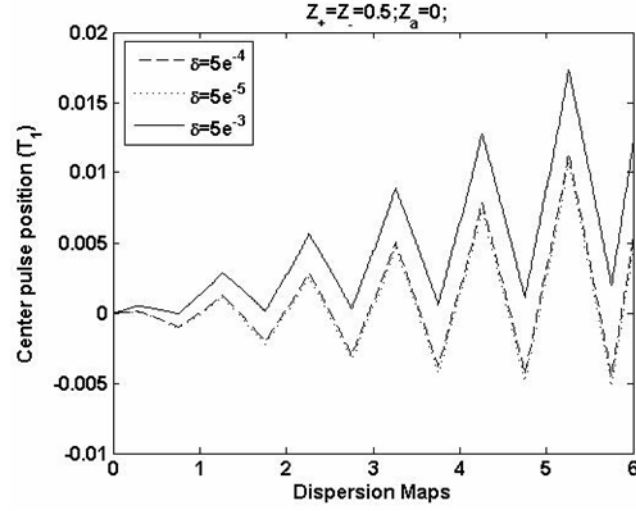


Fig. 3. Evolution of the center pulse position versus transmission distance for three different values of δ . The amplifiers are located at $Z_a = 0$, $Z_+ = Z_- = 0.5$ and $D_{av} = 1$.

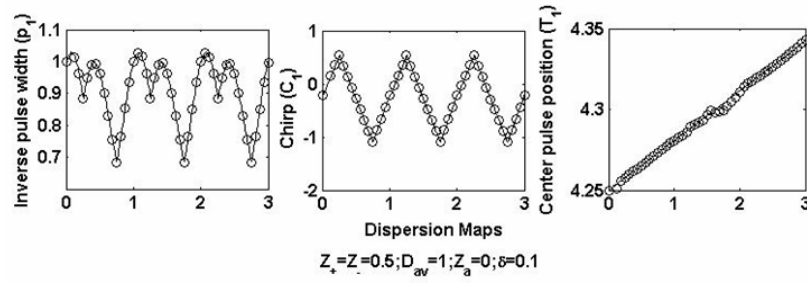


Fig. 4. Evolution of the main parameters of the pulse as obtained both through the ODE system and the full integration of the PDE.



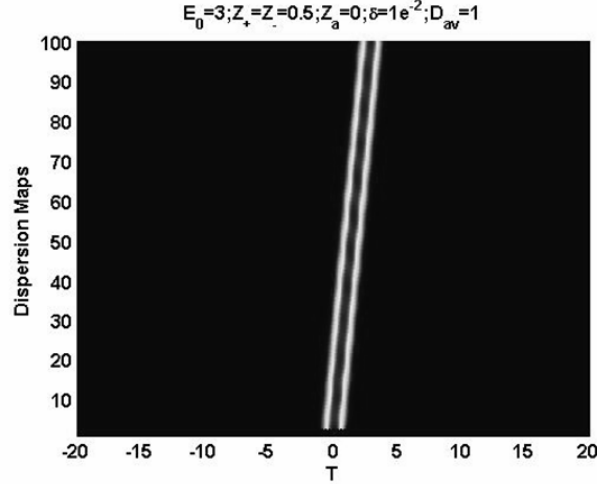


Fig. 5. Evolution of the intensity of the pulse for $\Delta D = 30$ and an amplifier located at $Z_a = 0$ with $Z_+ = Z_- = 0.5$ and $\delta = 0.01$.

3.2 Pulsewidth evolution

Figure 6 shows the interaction distance when the amplifier location is varied within the dispersion map for $\Delta D = 30$. The amplifier location is measured starting from the middle of the anomalous dispersion map. $Z_a = 0.25$ and $Z_a = 0.75$ means that the amplifier is located at the beginning or the end of the normal dispersion map. $Z_a = 0.5$ means that the amplifier is located at mid-point of the normal dispersion map. This Figure shows clearly that the interaction distance can be extended by suitably positioning the amplifier as explained in reference [13]. The interaction distance is smaller when the amplifier is located at the beginning ($Z_a = 0.25$) or the end ($Z_a = 0.75$) of the dispersion cell unit, than when it is located at the middle of the anomalous ($Z_a = 1$) or normal ($Z_a = 0.5$) fiber segment.



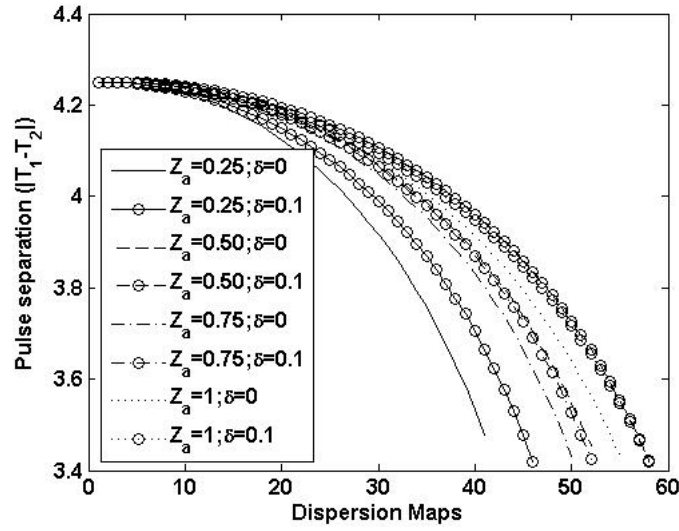


Fig. 6. Pulse separation versus transmission distance for different amplifier locations with and without TOD ($\delta = 0, 0.05$). $\Delta D = 30$ and initial pulse separation $|T_1 - T_2| = 4.25$.

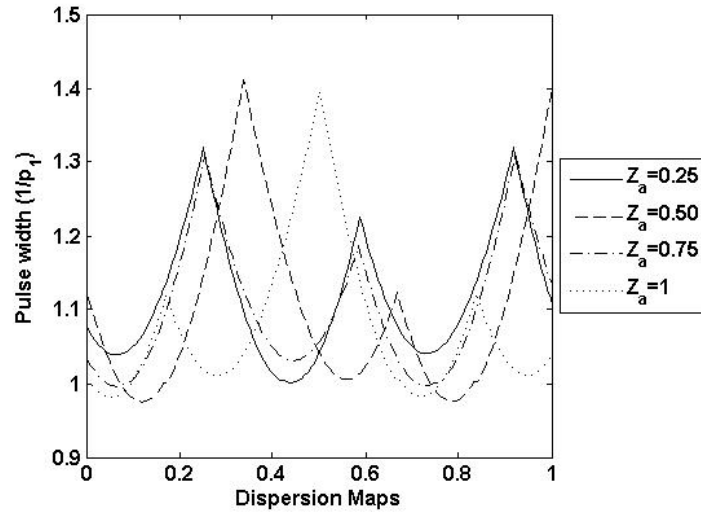


Fig. 7. Inverse pulsewidth evolution calculated by the variational approximation for different amplifier locations within the dispersion map.



This can be understood by the pulsewidth evolution along the fiber, as shown in Figure 7, which shows a single pulse in the steady state. For each curve in this Figure, the origin of the distance is set at the location of the amplifier.

We can see that the maximum pulse stretching occurs at distances closer to the amplifier, where the pulses have larger amplitude, $Z_a = 0.25$ and $Z_a = 0.75$, beginning and end of the dispersion cell unit, respectively, causing larger pulse-to-pulse interaction. Besides, most of the frequency change is induced near the junction between the anomalous and normal segments of the fiber where maximum pulse stretching occurs. Now, it can be easily seen that if we add the effect of third-order dispersion to the above pictures, as in Figure 6, with a significant amount of TOD, we can obtain an enhancement in the interaction distance, for some specific values of dispersion difference and amplifier locations. This improvement in the interaction distance is not due to energy or chirp, but mainly due to a greater displacement of the pulse center position as shown in Figure 3.

3.3 Energy enhancement

In Figure 8 we show the interaction distance of two neighboring pulses and the energy enhancement versus the amplifier location in a dispersion unit cell for an initial normalized pulse separation $|T_1 - T_2| = 4.25$ and dispersion difference $\Delta D = 30$. This Figure shows clearly that the interaction distance is dependent on the amplifier location. And it also shows that short interaction distances accompany large energy enhancements. This is because we have pulse stretching when power is high and the energy enhancement is large. So, although, as explained in [13], small pulse-to-pulse interaction and large energy enhancement are not achieved simultaneously, we can position the amplifier location so we can increase the interaction distance and reduce the interaction, with a small degradation of the energy enhancement. Besides, as shown in Figure 8, for some locations of the amplifier and some values of TOD, we can even decrease further, as explained in above paragraphs, the pulse-to-pulse interaction, without any further degradation of the energy enhancement.

4. Conclusion

In summary, we have analyzed interaction distance, pulsewidth evolution and energy enhancement for two pulse interaction propagating in strongly dispersion managed single channeled optical transmission systems by means of a variational approximation. The energy enhancement obtained for the DM soliton contributes to an extension of the interaction distance for some values of the dispersion difference.



We have found that the interaction distance can be extended by positioning the amplifier location at some specific places inside the dispersion cell unit. Besides, as we move to higher bit-rate transmission hierarchies, we must take into account third-order dispersion effects even for a single channel system. If we include TOD effects in the variational approximation, the evolution equations that describe the four main parameters of each pulse: inverse of the pulsewidth, chirp, center position and center frequency, show a change in chirp and center position. This enhancement of center pulse position helps to increase even further the interaction distance for some positions of the amplifier.

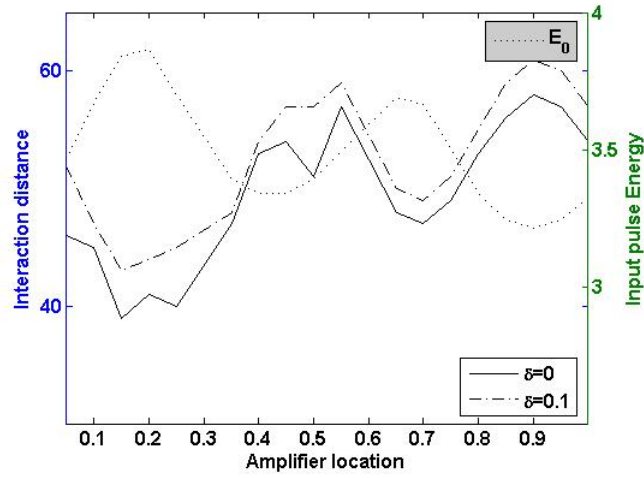


Fig. 8. Interaction distance of two neighboring pulses with initial pulse separation $|T_1 - T_2| = 4.25$ and energy enhancement factor of a single pulse in the steady state for different amplifier locations in the dispersion map with and without TOD ($\delta = 0, 0.1$) and $\Delta D = 30$.

Acknowledgements

This work has been supported by the Spanish Government and European Regional Development Fund (ERDF) under projects CSD2008-00068 and TACTICA.

References

1. L.F. Mollenauer and J.P. Gordon, *Solitons in optical fibers: fundamentals and applications*, Amsterdam/Boston, Elsevier/Academic Press, 2006.

7th CHAOS Conference Proceedings, 7-10 June 2014, Lisbon Portugal
C. H. Skiadas (Ed) □

©2014 ISAST



2. B. Malomed, *Soliton Management in periodic systems*, Springer, 2006.
3. N. J. Smith, F. M. Knox, N. J. Doran, K. J. Blow, and I. Bennion, *Enhanced power solitons in optical fibers with periodic dispersion management*, *Elect. Lett.*, 32, 1996, pp.54-55.
4. N. J. Smith, N. J. Doran, F. M. Knox, and W. Forysiak, *Energy-scaling characteristics of solitons in strongly dispersion-managed fibers*, *Opt. Lett.*, 21, 1996 pp. 1981-1983.
5. T.-S. Yang and W. L. Kath, *Analysis of enhanced-power solitons in dispersion-managed optical fibers*, *Opt. Lett.*, 22, 1997 pp. 985-987.
6. M. Matsumoto, *Theory of stretched-pulse transmission in dispersion managed fibers*, *Opt. Lett.*, 22, 1997 pp. 1238-1240.
7. T. Inoue, H. Sugahara, A. Maruta and Y. Kodama, *Interactions Between Dispersion Managed Solitons in Optical-Time-Division-Multiplexed Systems*, *IEEE Phot. Tech. Lett.*, 22, 2000, pp. 299.
8. T. Lakoba and G. Agrawal, *Effects of third-order dispersion on dispersion-managed solitons*, *J. Opt. Soc. Am B.*, 16, 1999, pp. 1332.
9. S. Mookherjee and A. Yariv, *Hamiltonian dynamics of breathers with third-order dispersion*, *J. Opt. Soc. Am. B*, 18, 2001, pp. 1150.
10. F. J. Diaz-Otero, P. Chamorro-Posada and J.C. Garcia-Escartin, *Dispersion-managed soliton interactions in the presence of third-order dispersion*, II International Conference on Advanced Optoelectronics and Lasers, CAOL Proceedings 2005, pp. 1531-1555.
11. D. Anderson, *Variational approach to nonlinear pulse propagation in optical fibers*, *Phys. Rev. A*, 27, 1983, pp. 3135.
12. Francisco J. Diaz-Otero, Pedro Chamorro-Posada, *Interchannel Soliton Collisions in Periodic Dispersion Maps in the Presence of Third Order Dispersion*, *J. Nonlin. Math. Phys.*, 15 Supp. 3, 2008, pp. 137-143.
13. M. Matsumoto, *Analysis of Interaction Between Stretched Pulses Propagating in Dispersion-Managed Fibers*, *Phot. Tech. Lett.*, 10, 1998, pp. 373-375.
14. K. Hizanidis, B. Malomed, H. Nistazakis and D. Frantzeskakis, *Stabilizing soliton transmission by third-order dispersion in dispersion compensated fibre links*, *Pure Appl. Opt.*, 7, 1998, L57-L62.
15. H. Sugahara, H. Kato, T. Inoue, A. Maruta and Y. Kodama, *Optimal dispersion management for a wavelength division multiplexed optical soliton transmission system*, *J. Lightwave Tech.*, 17, 1999, pp. 1547.
16. M. Ablowitz, G. Biondini, A. Biswas, A. Docherty, T. Hirooka and S. Chakravarty, *Collision-induced timing shifts in dispersion-managed soliton systems*, *Opt. Lett.*, 27, 2002, pp. 318-320.
17. G. P. Agrawal, *Nonlinear fiber optics*, 3rd ed., San Diego: Academic Press, 2001.

7th CHAOS Conference Proceedings, 7-10 June 2014, Lisbon Portugal

C. H. Skiadas (Ed) □

©2014 ISAST



Multifractal and Energy Parameters Can Underlie an Express Diagnostics of the Human Motor Dysfunction

Olga E. Dick

Physiology of Russian Academy of Science, St. Petersburg, Russia
E-mail: glazov.holo@mail.ioffe.ru

Abstract. The aim is to determine characteristics of tremor determined as fast involuntary shaking and arising during the performance of the motor task by healthy subjects and patients with akinetic–rigid form of Parkinson’s disease. The motor task is to keep the force by hands under isometric conditions (without finger movement in space). The tremor (the fast component) isolated from the registered trajectory of the isometric force varies by the amplitude for healthy and parkinsonian subjects but it poorly differs by frequency making difficulties in distinguishing frequency spectra. The wavelet multilevel decomposition and multifractal analysis allowed us to compare the numerically expressed energy and multifractal parameters of tremor instead of the registered trajectories. At each decomposition level the energy parameters of physiological tremor are less than for parkinsonian tremor. The parkinsonian impairment degree correlates with deviation of the parameter values from the values obtained for the healthy persons. Antiparkinsonian drug administration in the dose usual for the parkinsonian patients leads to a decrease of differences between both the energy and multifractal parameters for the healthy and parkinsonian subjects. Thus, the considered energy and multifractal characteristics can underlie an express diagnostics of the human motor dysfunction and determine the strategy of selection of optimal drugs for relieving parkinsonian tremor.

Keywords: Parkinson’s disease, Tremor, Wavelet decomposition, Multifractal.

1 Introduction

Involuntary shaking (tremor) of a body part can accompany some motor tasks, e.g., sustaining effort of fingers [1]. The mechanism underlying these involuntary oscillations appears to be related to discharges in feedback loops between motor cortical areas and basal ganglia and in the transcortical loop between the somatosensory and motor cortical areas [1, 2, 3]. Tremor may result from mechanical resonance in muscles and mobile parts of the skeleton, with the resonance frequency depending on the stretching strength applied to the limbs [4]. Under normal conditions, involuntary shaking has a small amplitude and does not impair motor performance [5]. The dispersion of frequency of involuntary oscillations from 8 to 12 Hz indicates asynchronous firing of individual motor units and a delay of the spread of impulses along feedback

7th CHAOS Conference Proceedings, 7-10 June 2014, Lisbon Portugal

C. H. Skiadas (Ed)

© 2014 ISAST



loops [6, 7]. If a task requires fine control of the steady positions of fingers, tremor in the 16–50 Hz range is added [8]. The appearance of high frequency oscillations is usually related to the involvement of sensory information processing.

Pathological tremor disrupting the movement performance or posture maintenance is specified by a higher amplitude than physiological tremor has. It is related to an increasing synchronization of motor units. For example, synchronization of neurons in the nuclei of the thalamus and basal ganglia, from which descending signals are indirectly transmitted to the muscles explains the large tremor of 3–6 Hz typical for patients with Parkinson's disease [1]. We studied tremor arising during keeping the force by hands under isometric conditions (without finger movement in space). Sometimes, especially in the case of akinetic–rigid parkinsonian form this considerably nonstationary tremor does not differ noticeably in frequency in comparison with healthy subjects [9].

The aim of the work is to find scores giving evaluation of differences in involuntary shaking of fingers by performing a motor task by a healthy subject and a patient with Parkinson's disease. For estimating the nonstationary signal features we use methods of nonlinear dynamics, namely, wavelet transform and multifractal analysis, which allow us to compare the numerically expressed energy parameters and scaling exponents of tremor. This analysis may serve as the basis for a diagnostics of the human motor dysfunction.

2 The experimental procedure

We used the results of testing 12 healthy subjects aged 43–54 years and 10 parkinsonian patients with bilateral akinesia and tremor aged 45–62 years. The motor task was to control the isometric muscle effort with the strength of muscle contraction shown by the positions of marks on a monitor. The subjects sat in front of a monitor standing on a table and pressed on platforms containing stress sensors with their fingers. The sensors transformed the pressure strength of the fingers of each hand into an electric signal. The rigidity of the platforms made it possible to record the effort in the isometric mode, i.e., without noticeable movement of fingers at the points of contact with the sensors. The isometric effort was recorded for 30 s in tests of two types: in the first test, the subject's fingers sustained an upward muscle effort, with the back of each hand pressing against the base of the platform; in the second test, the effort was downward. In both cases, the subject's arms were straightened.

The patients with Parkinson's disease did not take any drugs before the test on the day of testing. Usually, these patients received nakom, an antiparkinsonian preparation containing levodopa and carbidopa (a decarboxylase inhibitor) at doses of 200 and 50 mg, respectively, three times a day to compensate for dopamine deficiency.

The recorded trajectory of isometric effort consisted of a slow trend and a fast involuntary component (tremor), which was isolated from the recorded trajectory using the MATLAB software.

3 Wavelet transform and multifractality

3.1 Estimation of parameters of the energy spectral density of tremor

The algorithm of multilevel wavelet decomposition and reconstruction of a signal allows to represent the analyzed signal as the sum

$$x(t_i) = A_m(t_i) + D_m(t_i) + \dots + D_1(t_i),$$

where the component $A_m(t_i)$ gives the coarse approximation to the initial signal at the m^{th} level of decomposition and $D_1(t_i)$, ... and $D_m(t_i)$ determine details. The component $D_1(t_i)$ characterizes details at the highest frequencies. Thus, the algorithm permits to elucidate features of the signal at various frequencies. The central frequency of the wavelet corresponding to the j^{th} level of decomposition was calculated as $f_r f_s / 2^j$, $j = 1, \dots, m$, where $f_s = 50$ Hz is the sampling frequency and $f_r = 0.71$ is the central frequency of the mother Daubechies wavelet db_4 used in this work. To analyze the tremor details we used the method for estimating parameters of the energy spectral density of a signal [9].

Let $S(f)$ be the energy spectral density of the component $D(t)$ equal to the square of the Fourier transform:

$$S(f) = \left| \int D(t) e^{-2\pi i f t} dt \right|^2.$$

Then the total energy accumulated in the frequency range $[f_1, f_2]$ is

$$e = \int_{f_1}^{f_2} S(f) df.$$

As an energy parameter of the energy spectral density we use the value

$$k = e_{\max} / ((f_2 - f_1) f_{\max}),$$

where f_{\max} is the frequency value corresponding to e_{\max} and the frequencies f_1 and f_2 correspond to values $0.05 * S_{\max}$ and $0.95 * S_{\max}$. Thus, the frequency range $[f_1, f_2]$ specifies the energy spectrum kept after 5% filtration of noise.

The parameter k describes the relation between the maximal accumulation of the signal energy, the frequency corresponding to the maximum of the energy spectral density, and the frequency range $[f_1, f_2]$ at which the energy is accumulated.

3.2 Estimation the global wavelet spectrum of the tremor

To evaluate the difference between physiological and pathological tremors, we used the wavelet transform modulus maxima (WTMM) method [10] based on the continuous wavelet transform of a time series describing the examined tremor $x(t)$:

$$W(a, t_0) = a^{-1} \int_{-\infty}^{+\infty} x(t) \psi^* ((t - t_0)/a) dt,$$

where a and t_0 are the scale and space parameters, $\psi((t - t_0)/a)$ is the wavelet function obtained from the basic wavelet $\psi(t)$ by scaling and shifting along the time, symbol $*$ means the complex conjugate. As the basic wavelet we use the complex Morlet wavelet:

$$\psi(t) = D \exp(-0.5t^2) [\exp(-i\omega_0 t) - \exp(-0.5\omega_0^2)],$$

where the function

$$D = \frac{\pi^{-1/4}}{\sqrt{1 - 2 \exp(-0.75\omega_0^2) + \exp(-\omega_0^2)}}.$$

The value $\omega_0 = 2\pi$ gives the simple relation between the scale a and the frequency f : $f = 1/a$.

The modulus of the wavelet spectrum $|W(f, t_0)|$ characterizes the presence and intensity of the frequency f at the moment t_0 in the signal and $|W(f, t_0)|^2$ describes the instantaneous distribution of the tremor energy over frequencies, that is, the local spectrum of the signal energy at the time t_0 .

The value

$$E(f) = \int_{t_1}^{t_2} |W(f, t_0)|^2 dt_0$$

determines the global wavelet spectrum, i.e., the integral distribution of the wavelet spectrum energy over frequency range on the time interval $[t_1, t_2]$.

3.3 Estimation the tremor multifractality

Information about possible multifractal feature of the signal and its localization t_0 reflects in the asymptotic behavior of coefficients $|W(a, t_0)|$ at small a values and large f values, respectively. The faster the wavelet coefficients

decrease at $f \rightarrow \infty$, the more regular the signal is around that point. Abnormal small decrease of the wavelet coefficients at $a \rightarrow 0$ in a neighborhood of the point t_0 testifies about singularity of the signal at the point. Thus, the rate of the change of the modulus of the wavelet coefficients enables to analyze the presence or absence of singularities of the signal.

The degree of singularity of the signal $x(t)$ at the point t_0 is described by the Hölder exponent, $h(t_0)$, the largest exponent such that the analyzed signal in a neighborhood of the point t_0 can be represented as the sum of the regular component (a polynomial $P_n(t)$ of order $n < h(t_0)$) and a member describing a non - regular behavior [10]:

$$x(t) = P_n(t) + c|t - t_0|^{h(t_0)}.$$

The value $h(t_0)$ is the measure of singularity of the signal at the point t_0 since the smaller $h(t_0)$ value, the more singular the signal.

In view of the simple dependence $W(a, t_0) \sim a^{h(t_0)}$ at $a \rightarrow 0$ [10], the Hölder exponent can be calculated by

$$h(t_0) \sim \log_{10} W(a, t_0) / \log_{10} a.$$

However, with increasing the scale a the influence of neighbouring nonregularities can lead to inaccuracy, that is why we determined the Hölder exponents on the basis of statistical description of local singularities by partition functions [11].

The algorithm consists of the following procedures.

- 1) The continuous wavelet transform of the time series is used.
- 2) A set $L(a)$ of lines of local modulus maxima of the wavelet coefficients is found at each scale a
- 3) The partition functions are calculated by the sum of q - powers of the modulus maxima of the wavelet coefficients along the each line at the scales smaller the given value a :

$$Z(q, a) = \sum_{l \in L(a)} \left(\sup_{a^* \leq a} |W(a^*, t_l(a^*))| \right)^q,$$

$t_l(a^*)$ determines the position of the maximum corresponding to the line l at this scale

- 4) By the fact that the partition function is $Z(q, a) \sim a^{\tau(q)}$ at $a \rightarrow 0$ [11], the scaling exponent can be extracted as

$$\tau(q) \sim \log_{10} Z(q, a) / \log_{10} a.$$

5) Choosing different values of the power q one can obtain a linear dependence $\tau(q)$ with a constant value of the Hölder exponent

$$h(q) = d\tau(q)/dq = \text{const}$$

for monofractal signals and nonlinear dependence $\tau(q) = qh(q) - D(h)$ with large number of the Hölder exponents for multifractal signals.

6) The singularity spectrum (distribution of the local Hölder exponents) is calculated from the Legendre transform [11]:

$$D(h) = qh(q) - \tau(q).$$

Using the global wavelet spectra and the WWTM algorithm for the different tremor recording we obtain the maximum of the global tremor energy (E_{\max}) and two multifractal parameters:

a) the width of the singularity spectrum

$$\Delta h = h_{\max} - h_{\min},$$

where h_{\max} and h_{\min} are the maximal and minimal values of the Holder exponent corresponding to minimal and maximal tremor fluctuation, respectively;

b) the asymmetry of the singularity spectrum

$$\Delta = |\Delta_2 - \Delta_1|,$$

where $\Delta_1 = h_{\max} - h_0$ and $\Delta_2 = h_0 - h_{\min}$, $h_0 = h(q = 0)$.

Smaller Δh indicates that the time series tends to be monofractal and larger Δh testifies the enhancement of multifractality. The asymmetry parameter Δ characterizes where, in the region of strong singularities ($q > 0$) or in the region of weak singularities ($q < 0$), the singularity spectrum is more concentrated.

To compare the mean values in each of the examined group of subjects the Student criterion was applied.

4 Results and discussion

Two components of oscillations of the isometric force trajectory of the human hand, namely, slow trend and tremor, are given in Fig. 1 for the healthy subject (Fig. 1a) and for the parkinsonian patient before (Fig. 1b) and after nakom medication (Fig. 1c). The amplitude of parkinsonian tremor is nearly twice larger than physiological tremor isolated for the healthy subject. Two hours after nakom medication the parkinsonian tremor reduced by amplitude to the values specified for the healthy subject. The differences in slow components were not essential.

The right column of Fig. 1 shows the curves $\tau(q)$ (Fig. 1d), $h(q)$ (Fig. 1e) and the singularity spectra $D(h)$ for the same subjects. The nonlinear dependence

$\tau(q)$ indicates the large number of Hölder exponents. These dependences and the form of singularity spectrum $D(h)$ testifies the multifractality of both physiological and parkinsonian tremor. However, the Hölder exponents differ for the two subjects. The differences are maximal at weak fluctuations ($q < 0$).

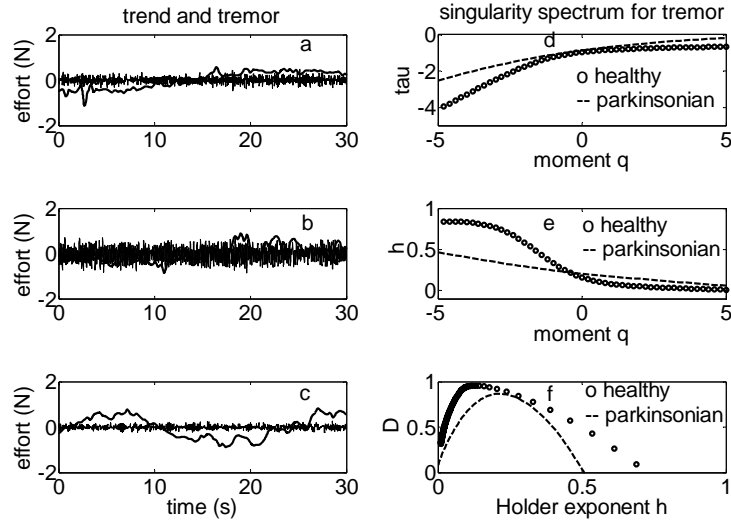


Fig. 1. Examples of two components of the isometric force trajectory of the human hand (slow trend and tremor) for a healthy subject (a) and for a patient with Parkinson disease before the drug administration (b) and after (c). Multifractal curves for tremor: $\tau(q)$ (d), $h(q)$ (e) and singularity spectra $D(h)$.

The healthy tremor is characterized by the largest width Δh and, therefore, by the significant degree of multifractality. The decline in the width of the singularity spectrum shows a reduction of nonuniformity of the parkinsonian tremor and a fall in the multifractality degree.

The singularity spectrum asymmetry Δ is also larger for healthy tremor and for parkinsonian one the value of Δ is close to 0.1.

The decrease of the both parameters in tremor of patients with Parkinson's disease is due to decreasing contribution of weak fluctuations (for $q < 0$).

In healthy tremor the singularity spectrum is expanded so that the dynamics of persistent sequences exhibits both anticorrelated (for $h < 0.5$) and correlated (for $h > 0.5$) behavior.

The decrease of h_{\max} in parkinsonian tremor as compared with the physiological one testifies about the enhancement of the anticorrelation degree so that the tremor tend to become more random and less smooth. The consequent values are anticorrelated ($h < 0.5$), i.e., persistent sequences in pathological tremor are

characterized by stochastically up - down patterns in which large values are more likely to be followed by small values and vice versa.

Antiparkinsonian drug administration leads to the increase of the multifractal parameters increasing both the width and the asymmetry of the singularity spectrum.

The energy parameter k enhances with increasing the decomposition level (Fig. 2). For the healthy tremor the means of k values are less than for the parkinsonian one on all the levels. The differences between the parameter k values for the healthy and parkinsonian subjects reduce with increasing the decomposition level. Maximal differences (in three orders) are observed at the first level that is for the high frequency details. This level specifies frequencies located near 17.8 Hz. At the last decomposition level the means of k values distinguish much less. But even at the fourth level with frequencies close to 2.2 Hz the values differ.

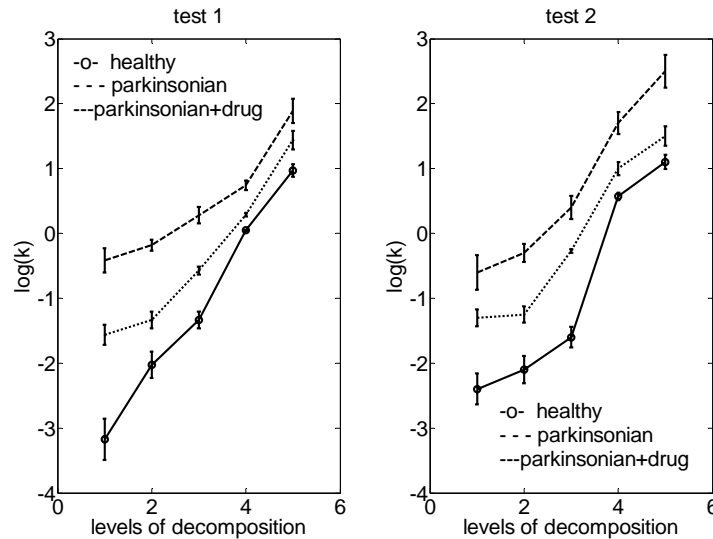


Fig.2 Dependences of mean values of the energy parameter k on the decomposition level. The solid line corresponds to the healthy tremor, the dashed lines specifies the parkinsonian tremor before and after nakom administration.

Antiparkinsonian drug administration in the dose usual for the parkinsonian patients leads to a decrease of differences between means of k for the healthy and parkinsonian subjects at all the decomposition levels. This testifies that two hours after medication of the drug compensating deficit of dopamine in basal ganglia tremor arising during maintenance of isometric force by the parkinsonian subject becomes similar to physiological tremor by the energy parameter of the spectral density of the tremor detail components.

Calculation of the instantaneous frequency - time distributions $|W(f, t_0)|^2$ and global wavelet spectra $E(f)$ enables us to find the enormous enhancement (about in 300 times) of the maximal global energy E_{\max} in parkinsonian tremor as compared with the healthy one (Fig.3).

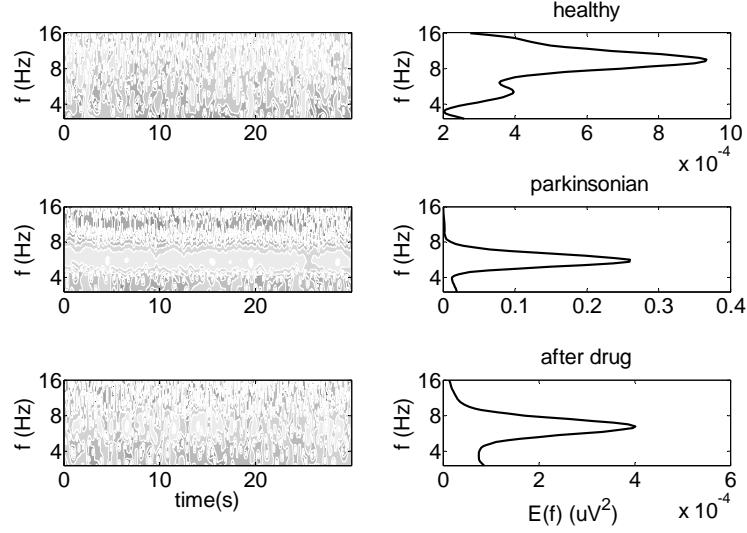


Fig. 3. Examples of the instantaneous frequency-time distributions of the tremor energy $|W(f, t_0)|^2$ (left column) and global wavelet spectra $E(f)$ (right column) for the same subjects as in Fig.1.

The maximal value E_{\max} of physiological tremor is in the frequency range of alpha rhythm [8, 14] Hz. For the pathological tremor E_{\max} is shifted in the theta range [4, 7.5] Hz. Two hours later after antiparkinsonian drug medication the energy value dramatically reduces to the value specified for the healthy volunteers.

The similar dynamics of the energy and multifractal parameters is observed for all the examined subjects. It enables us to use the common practice of averaging the recordings of all subjects for testing significant variations among the groups. The values of E_{\max} , Δh and Δ averaged by subjects in every group are given in Table 1. The significant distinctions between the states (pathological or physiological tremor) are identified by all the three parameters ($p=0.02$, $p=0.03$ and $p=0.01$, respectively).

| state | test | hand | E_{\max}^* 10^{-4} | Δh | Δ | clinical manifes- tation of tremor |
|--|------|-------|---------------------------|-----------------|-----------------|---|
| healthy | 1 | right | 7.5 ± 0.3 | 0.75 ± 0.06 | 0.37 ± 0.03 | no |
| | | left | 6.8 ± 0.2 | 0.82 ± 0.07 | 0.42 ± 0.04 | |
| | 2 | right | 8.7 ± 0.3 | 0.78 ± 0.07 | 0.38 ± 0.04 | |
| | | left | 7.9 ± 0.3 | 0.69 ± 0.05 | 0.45 ± 0.05 | |
| parkinsonian | 1 | right | 2150 ± 115 | 0.34 ± 0.03 | 0.14 ± 0.03 | yes |
| | | left | 2397 ± 146 | 0.29 ± 0.02 | 0.19 ± 0.01 | |
| | 2 | right | 1976 ± 101 | 0.38 ± 0.02 | 0.11 ± 0.01 | |
| | | left | 2110 ± 131 | 0.41 ± 0.03 | 0.15 ± 0.01 | |
| parkinsonian 2 hours after drug medication (68% patients) | 1 | right | 5.2 ± 0.1 | 0.81 ± 0.08 | 0.51 ± 0.05 | no |
| | | left | 8.2 ± 0.3 | 0.86 ± 0.07 | 0.56 ± 0.05 | |
| | 2 | right | 9.3 ± 0.3 | 0.71 ± 0.07 | 0.41 ± 0.04 | |
| | | left | 7.3 ± 0.2 | 0.74 ± 0.07 | 0.54 ± 0.04 | |
| parkinsonian 2 hours after drug medication (32% patients) | 1 | right | 1870 ± 106 | 0.43 ± 0.03 | 0.13 ± 0.01 | yes |
| | | left | 1687 ± 92 | 0.35 ± 0.02 | 0.17 ± 0.01 | |
| | 2 | right | 1933 ± 113 | 0.42 ± 0.02 | 0.22 ± 0.01 | |
| | | left | 1881 ± 103 | 0.37 ± 0.02 | 0.15 ± 0.01 | |

Table 1. Comparison of the mean values, averaging over subjects inside the every examined group. The subject's fingers sustained an upward muscle effort (test 1) and downward effort (test 2).

Our results demonstrate that clinical manifestation of tremor is correlated with the significant enhancement of the maximal global energy and the decrease of the width and the asymmetry of the singularity spectrum. The disappearance of the clinical features of the pathological tremor in 68 % of the examined patients is accompanied by approximation of the multifractal and energy parameters to the values obtained for the healthy subjects.

We have shown that parkinsonian damage of the brain leads to the characteristic breakdown or modification in the long-range correlations of neuronal activity that can be a useful indicator of a dysfunctional network in the central nervous system.

The long-range correlations can be related to fractality of intracellular process defining the amplitude and the velocity of the action potential propagation. So, the long-range correlations of sequences of life time of ion channels and dynamics of change in the membrane - binding calcium concentration have been shown in [12]. The long-term memory in ion channel dynamics leads to the memory in fluctuations of a nerve fiber excitability [13]. An increase of the

number of excitable fibers during propagation of rhythmical impulses is accompanied by a decrease of the long-range correlations in sequences of the action potential amplitudes and an increase of correlations in the velocities of the action potential propagation [14]. It may underlie the reduction of the long-term memory for parkinsonian disruption of the central control by movements as evidenced by the increasing synchronization and decrease of the multifractality of involuntary oscillations.

Conclusions

Our examination of differences in physiological and pathological tremor arising during the maintenance of isometric force by hands of a healthy subject and a subject with Parkinson's disease demonstrates that the energy parameters and multifractal characteristics can serve as estimations of the human motor dysfunction since their values reflect the degree of deviation of pathological involuntary oscillations from the normal ones.

References

1. J. H. McAuley, C. D. Marsden. Physiological and pathological tremors and rhythmic central motor control. *Brain*, 123, 8, 1545-1567, 2000.
2. C. D. Marsden. Origins of normal and pathological tremor. In: Findley L. J., Capildeo R. (eds) *Movement disorders: tremor*. MacMillan Press, London, 37-84, 1984.
3. B. Vallbo, J. Wessberg. Organization of motor output in slow finger movements in man, *J. Physiol.*, 469, 673-691, 1993.
4. S. F. Farmer, M. Swash, D. A. Ingram, J. A. Stephens. Changes in motor unit synchronization following central nervous lesions in man, *J. Physiol.*, 463, 83-105, 1993.
5. R. Elble. Physiologic and essential tremor, *Neurology*, 36, 225-231, 1986.
6. S. Grillner. The motor infrastructure: from ion channels to neuronal networks, *Nature Reviews Neuroscience*, 4, 573- 586, 2003.
7. J. H. McAuley, J. C. Rothwell, C. D. Marsden. Frequency peaks of tremor, muscle vibration and electromyographic activity at 10 Hz, 20 Hz and 40 Hz during human finger muscle contraction may reflect rhythmicities of central neural firing, *Exp. Brain Res.*, 114, 525-541, 1997.
8. G. P. Van Galen, R. R. Van Doorn, L. R. Schomaker. Effects of motor programming on the power spectral density function of finger and wrist movements, *J. Exper. Psychol.*, 16, 755- 765, 1990.
9. O. E. Dick, S. P. Romanov, A. D. Nozdrachev. Energy and Fractal Characteristics of Physiological and Pathological Tremors of the Human Hand, *Human Physiology*, 36, 2, 203-210, 2010.
10. J. F. Muzy, E. Bacry, A. Arneodo. Multifractal formalism for fractal signals: the structure-function approach versus the wavelet-transform modulus-maxima method, *Phys. Rev. E*, 47, 875-884, 1993.
11. Arneodo, E. Bacry, J. F Muzy. The thermodynamics of fractals revisited with wavelets. *Physica A*, 213, 232-275, 1995.

12. W. A. Varanda, L. S. Liebovitch, J. N. Figueroa, R. A. Nogueira. Hurst analysis applied to the study of single calcium - activated potassium channel kinetics. J. Theor. Biol., 206, 343- 353, 2000.
13. S. B. Lowen, L. S. Liebovitch, J. A. White. Fractal ion – channel behaviour generates fractal firing patterns in neuronal models. Phys. Rev. E., 59, 5970 – 5980, 1999.
14. R. Brazhe, G. V. Maksimov. Self – organized critical gating of ion channels: on the origin of long – term memory in dwell time series. Chaos, 16, 33129 - 33135, 2006.

Acknowledgements

A part of the work was supported by the Program of Presidium of RAS “*Fundamental sciences for medicine in 2014 year*”

Algorithms of Estimating Reachable Sets of Nonlinear Control Systems with Uncertainty

Tatiana F. Filippova¹ and Oxana G. Matviychuk²

¹ Department of Optimal Control of the Institute of Mathematics and Mechanics of the Ural Branch of Russian Academy of Sciences and Ural Federal University, Ekaterinburg, Russian Federation

(E-mail: ftf@imm.uran.ru)

² Department of Optimal Control of the Institute of Mathematics and Mechanics of the Ural Branch of Russian Academy of Sciences and Ural Federal University, Ekaterinburg, Russian Federation

(E-mail: vog@imm.uran.ru)

Abstract. The problem of estimating reachable sets of nonlinear dynamical control systems with quadratic nonlinearity and with uncertainty in initial states is studied. We assume that the uncertainty is of a set-membership kind when we know only the bounding set for unknown items and any additional statistical information on their behavior is not available. We present approaches that allow finding ellipsoidal estimates of reachable sets. The algorithms of constructing such ellipsoidal set-valued estimates and numerical simulation results are given in two cases, for control systems with classical controls and for measure driven (impulsive) control systems.

Keywords: Nonlinear Control Systems, Uncertainty, State Estimation, Ellipsoidal Calculus, Funnel Equations, Trajectory Tubes, Simulation.

1 Introduction

In this paper we study control systems with unknown but bounded uncertainties related to the case of a set-membership description of uncertainty (Bertsekas and Rhodes[1], Kurzhanski and Valyi[11], Schweppe[13], Walter and Pronzato[15]). The motivation to consider the set-membership approach is that in traditional formulations the characterization of parameter uncertainties requires assumptions on mean, variances or probability density function of errors. However in many applied areas ranged from engineering problems in physics to economics as well as to biological and ecological modeling it occurs that a stochastic nature of the error sequence is questionable. For instance, in case of limited data or after some non-linear transformation of the data, the presumed stochastic characterization is not always valid. Hence, as an alternative to a stochastic characterization a so-called bounded-error characterization, also called set-membership approach, has been proposed and intensively developed in the last decades.

7th CHAOS Conference Proceedings, 7-10 June 2014, Lisbon Portugal
C. H. Skiadas (Ed)

© 2014 ISAST



The solution of many control and estimation problems under uncertainty involves constructing reachable sets and their analogs. For models with linear dynamics under such set-membership uncertainty there are several constructive approaches which allow finding effective estimates of reachable sets. We note here two of the most developed approaches to research in this area. The first one is based on ellipsoidal calculus (Chernousko[2], Kurzanski and Valyi[11]) and the second one uses the interval analysis (Walter and Pronzato[15]).

Many applied problems are mostly nonlinear in their parameters and the set of feasible system states is usually non-convex or even non-connected. The key issue in nonlinear set-membership estimation is to find suitable techniques, which produce related bounds for the set of unknown system states without being too computationally demanding. Some approaches to the nonlinear set-membership estimation problems and discrete approximation techniques for differential inclusions through a set-valued analogy of well-known Euler's method were developed in Dontchev and Lempio[3], Veliov[14]. In this paper the modified state estimation approaches which use the special quadratic structure of nonlinearity of studied control system and use also the advantages of ellipsoidal calculus (Kurzanski and Valyi[11], Chernousko[2]) are presented.

2 Preliminaries

In this section we introduce the following basic notations. Let R^n be the n -dimensional Euclidean space and $x'y$ be the usual inner product of $x, y \in R^n$ with prime as a transpose, $\|x\| = (x'x)^{1/2}$. We denote as $B(a, r)$ the ball in R^n , $B(a, r) = \{x \in R^n : \|x - a\| \leq r\}$, I is the identity $n \times n$ -matrix. Denote by $E(a, Q)$ the ellipsoid in R^n , $E(a, Q) = \{x \in R^n : (Q^{-1}(x - a), (x - a)) \leq 1\}$ with center $a \in R^n$ and symmetric positive definite $n \times n$ -matrix Q .

Consider the following system

$$\dot{x} = Ax + f^{(1)}(x)d^{(1)} + f^{(2)}(x)d^{(2)}, \quad x_0 \in X_0, \quad t_0 \leq t \leq T, \quad (1)$$

where $x \in R^n$, $\|x\| \leq K$ ($K > 0$), $d^{(1)}$ and $d^{(2)}$ are n -vectors and $f^{(1)}, f^{(2)}$ are scalar functions,

$$f^{(1)}(x) = x'B^{(1)}x, \quad f^{(2)}(x) = x'B^{(2)}x,$$

with symmetric and positive definite matrices $B^{(1)}, B^{(2)}$. We assume also that $d_i^{(1)} = 0$ for $i = k + 1, \dots, n$ and $d_j^{(2)} = 0$ for $j = 1, \dots, k$ where k ($1 \leq k \leq n$) is fixed. This assumption means that the first k equations of the system (1) contain only the nonlinear function $f^{(1)}(x)$ (with some constant coefficients $d_i^{(1)}$) while $f^{(2)}(x)$ is included only in the equations with numbers $k + 1, \dots, n$.

We will assume further that X_0 in (1) is an ellipsoid, $X_0 = E(a, Q)$, with a symmetric and positive definite matrix Q and with a center a .

We will need some auxiliary results.

Lemma 1. *The following inclusion is true*

$$X_0 \subseteq E(a, k_1^2(B^{(1)})^{-1}) \cap E(a, k_2^2(B^{(2)})^{-1}) \quad (2)$$

where k_i^2 is the maximal eigenvalue of the matrix $(B^{(i)})^{1/2}Q(B^{(i)})^{1/2}$ ($i = 1, 2$).

Proof. The proof follows directly from the properties of quadratic forms and from the inclusions

$$E(a, Q) \subseteq E(a, k_1^2(B^{(1)})^{-1}), \quad E(a, Q) \subseteq E(a, k_2^2(B^{(2)})^{-1}),$$

which should be fulfilled with the smallest possible values of $k_1 \geq 0$ and $k_2 \geq 0$.

Lemma 2. *The following equalities hold true*

$$\max_{z' B^{(1)} z \leq k_1^2} z' B^{(2)} z = k_1^2 \lambda_{12}^2, \quad \max_{z' B^{(2)} z \leq k_2^2} z' B^{(1)} z = k_2^2 \lambda_{21}^2, \quad (3)$$

where λ_{12}^2 and λ_{21}^2 are maximal eigenvalues of matrices $(B^{(1)})^{-1/2} B^{(2)} (B^{(1)})^{-1/2}$ and $(B^{(2)})^{-1/2} B^{(1)} (B^{(2)})^{-1/2}$ respectively.

Proof. The formulas follow from direct computations of maximal values in (3).

Theorem 1. (Filippova[6]) *For all $\sigma > 0$ and for $X(t_0 + \sigma) = X(t_0 + \sigma, t_0, X_0)$ we have the following upper estimate*

$$X(t_0 + \sigma) \subseteq E(a^{(1)}(\sigma), Q^{(1)}(\sigma)) \cap E(a^{(2)}(\sigma), Q^{(2)}(\sigma)) + o(\sigma)B(0, 1), \quad (4)$$

where $\sigma^{-1}o(\sigma) \rightarrow 0$ when $\sigma \rightarrow +0$ and

$$a^{(1)}(\sigma) = a(\sigma) + \sigma k_1^2 \lambda_{12}^2 d^{(2)}, \quad a^{(2)}(\sigma) = a(\sigma) + \sigma k_2^2 \lambda_{21}^2 d^{(1)}, \quad (5)$$

$$a(\sigma) = (I + \sigma A)a + \sigma a' B^{(1)} a d^{(1)} + \sigma a' B^{(2)} a d^{(2)}, \quad (6)$$

$$Q^{(1)}(\sigma) = (p_1^{-1} + 1)(I + \sigma R)k_1^2(B^{(1)})^{-1}(I + \sigma R)' + (p_1 + 1)\sigma^2 \|d^{(2)}\|^2 k_1^4 \lambda_{12}^4 \cdot I, \quad (7)$$

$$Q^{(2)}(\sigma) = (p_2^{-1} + 1)(I + \sigma R)k_2^2(B^{(2)})^{-1}(I + \sigma R)' + (p_2 + 1)\sigma^2 \|d^{(1)}\|^2 k_2^4 \lambda_{21}^4 \cdot I, \quad (8)$$

$$R = A + 2d^{(1)}a' B^{(1)} + 2d^{(2)}a' B^{(2)} \quad (9)$$

and p_1, p_2 are the unique positive solutions of related algebraic equations

$$\sum_{i=1}^n \frac{1}{p_1 + \alpha_i} = \frac{n}{p_1(p_1 + 1)}, \quad \sum_{i=1}^n \frac{1}{p_2 + \beta_i} = \frac{n}{p_2(p_2 + 1)} \quad (10)$$

with $\alpha_i, \beta_i \geq 0$ ($i = 1, \dots, n$) being the roots of the following equations

$$\det((I + \sigma R)k_1^2(B^{(1)})^{-1}(I + \sigma R)' - \alpha\sigma^2 \|d^{(2)}\|^2 k_1^4 \lambda_{12}^4 \cdot I) = 0, \quad (11)$$

$$\det((I + \sigma R)k_2^2(B^{(2)})^{-1}(I + \sigma R)' - \beta\sigma^2 \|d^{(1)}\|^2 k_2^4 \lambda_{21}^4 \cdot I) = 0. \quad (12)$$

We may formulate now the following scheme that gives the external estimate of trajectory tube $X(t)$ of the system (1) with given accuracy.

Algorithm 1. Subdivide the time segment $[t_0, T]$ into subsegments $[t_i, t_{i+1}]$ where $t_i = t_0 + ih$ ($i = 1, \dots, m$), $h = (T - t_0)/m$, $t_m = T$.

- Given $X_0 = E(a, Q)$, take $\sigma = h$ and define ellipsoids $E(a^{(1)}(\sigma), Q^{(1)}(\sigma))$ and $E(a^{(2)}(\sigma), Q^{(2)}(\sigma))$ from Theorem 2.

- Find the smallest (with respect to some criterion, Kurzhan-
ski and Valyi[11], Chernousko[2]) ellipsoid $E(a_1, Q_1)$ which contains the intersection

$$E(a^{(1)}(\sigma), Q^{(1)}(\sigma)) \cap E(a^{(2)}(\sigma), Q^{(2)}(\sigma)) \subseteq E(a_1, Q_1).$$

- Consider the system on the next subsegment $[t_1, t_2]$ with $E(a_1, Q_1)$ as the initial ellipsoid at instant t_1 .
- Next steps continue iterations 1-3. At the end of the process we will get the external estimate $E(a(t), Q(t))$ of the tube $X(t)$ with accuracy tending to zero when $m \rightarrow \infty$.

3 Main results

3.1 Control system under uncertainty

Consider the following control system in the form of differential inclusion (Kurzhan-
ski and Filippova[10])

$$\dot{x} \in Ax + f^{(1)}(x)d^{(1)} + f^{(2)}(x)d^{(2)} + P, \quad x_0 \in X_0 = E(a, Q), \quad t_0 \leq t \leq T, \quad (13)$$

with all previous assumptions being valid. We assume also that P is an ellipsoid, $P = E(g, G)$, with a symmetric and positive definite matrix G and with a center g .

In this case the estimate for $X(t_0 + \sigma)$ (the analogy of the formula (4)) takes the form.

Theorem 2. *The following inclusion is true*

$$\begin{aligned} X(t_0 + \sigma) \subseteq & E(a^{(1)}(\sigma), Q^{(1)}(\sigma)) \cap E(a^{(2)}(\sigma), Q^{(2)}(\sigma)) \\ & + \sigma E(g, G) + o(\sigma)B(0, 1), \end{aligned} \quad (14)$$

where $\sigma^{-1}o(\sigma) \rightarrow 0$ when $\sigma \rightarrow +0$ and the parameters $a^{(i)}, Q^{(i)}$ ($i = 1, 2$) are described in (5)–(9).

Proof. The inclusion follows from the Theorem 1 and from the properties of the trajectory tubes of related differential inclusions (see also techniques in Filippova[7]).

We should modify now the previous scheme (Algorithm 1) in order to formulate a new procedure of external estimating of trajectory tube $X(t)$ of the system (13).

Algorithm 2. Subdivide the time segment $[t_0, T]$ into subsegments $[t_i, t_{i+1}]$ where $t_i = t_0 + ih$ ($i = 1, \dots, m$), $h = (T - t_0)/m$, $t_m = T$.

- Given $X_0 = E(a, Q)$, take $\sigma = h$ and define ellipsoids $E(a^{(1)}(\sigma), Q^{(1)}(\sigma))$ and $E(a^{(2)}(\sigma), Q^{(2)}(\sigma))$ from Theorem 2.
- Find the smallest (with respect to some criterion (Kurzhan-
ski and Valyi[11], Chernousko[2]) ellipsoid $E(a^*, Q^*)$ which contains the intersection:

$$E(a^{(1)}(\sigma), Q^{(1)}(\sigma)) \cap E(a^{(2)}(\sigma), Q^{(2)}(\sigma)) \subseteq E(a^*, Q^*).$$

- Find the ellipsoid $E(a_1, Q_1)$ which is the upper estimate of the sum (Kurzhanski and Valyi[11], Chernousko[2]) of two ellipsoids, $E(a^*, Q^*)$ and $\sigma E(g, G)$:

$$E(a^*, Q^*) + \sigma E(g, G) \subseteq E(a_1, Q_1).$$

- Consider the system on the next subsegment $[t_1, t_2]$ with $E(a_1, Q_1)$ as the initial ellipsoid at instant t_1 .
- Next steps continue iterations 1-3. At the end of the process we will get the external estimate $E(a(t), Q(t))$ of the tube $X(t)$ with accuracy tending to zero when $m \rightarrow \infty$.

3.2 Examples

Consider three examples illustrating the techniques of ellipsoidal estimating. For simplicity we take here $d^{(2)} = 0$ so only one quadratic form is present at the right-hand side of the dynamic equations (13).

Example 1. Consider the following control system:

$$\begin{cases} \dot{x}_1 = 2x_1 + u_1, \\ \dot{x}_2 = 2x_2 + x_1^2 + x_2^2 + u_2, \end{cases} \quad x_0 \in X_0, \quad t \in [t_0, T]. \quad (15)$$

Here we take $t_0 = 0$, $T = 0.35$, $X_0 = B(0, 1)$ and put $P(t) \equiv U = B(0, 0.5)$ in the control constraint. The trajectory tube $X(t)$ and its external ellipsoidal estimate $E(a(t), Q(t))$ are given at Figure 1.

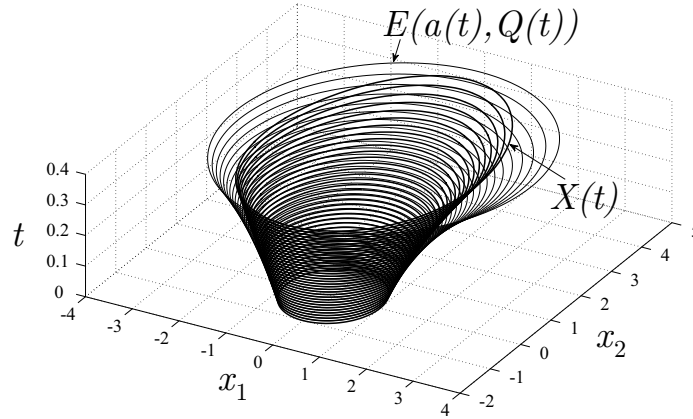


Fig. 1. Trajectory tube $X(t)$ and its ellipsoidal estimate $E(a(t), Q(t))$.

The following example illustrates the case where the reachable set may lose convexity with increasing time $t > t_0$. Nevertheless the related external estimate is also true.

Example 2. Consider the following control system:

$$\begin{cases} \dot{x}_1 = 2x_1 + u_1, \\ \dot{x}_2 = 2x_2 + 4x_1^2 + x_2^2 + u_2, \end{cases} \quad x_0 \in X_0, \quad t \in [t_0, T]. \quad (16)$$

Here we take $t_0 = 0$, $T = 0.25$, $X_0 = B(0, 1)$ and $P(t) \equiv U = B(0, 1)$. The trajectory tube $X(t)$ and its external ellipsoidal estimate $E(a(t), Q(t))$ are given at Figure 2.

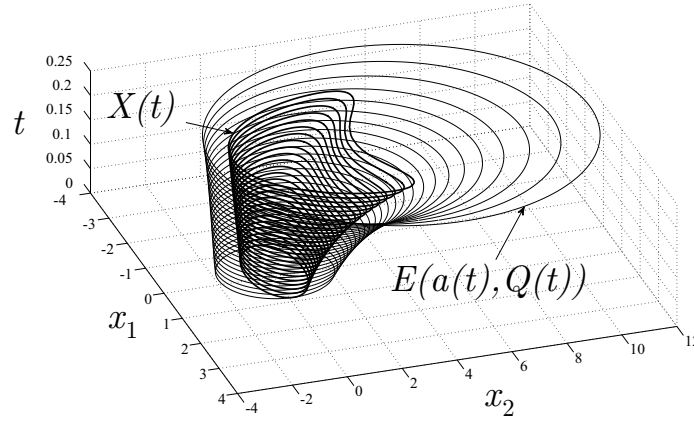


Fig. 2. Nonconvex-valued trajectory tube $X(t)$ and its external ellipsoidal estimate $E(a(t), Q(t))$.

The following example illustrates the main procedure of the new Algorithm 2 of Section 3.1.

Example 3. Consider the following control system with two quadratic forms in its dynamical equations:

$$\begin{cases} \dot{x}_1 = 1.5x_1 + x_1^2 + 2x_2^2 + u_1, \\ \dot{x}_2 = 1.5x_2 + 2x_1^2 + x_2^2 + u_2, \end{cases} \quad x_0 \in X_0, \quad t \in [t_0, T]. \quad (17)$$

Here we take $t_0 = 0$, $T = 0.3$, $X_0 = B(0, 1)$ and $U = B(0, 0.1)$. Steps of the Algorithm 2 of constructing the external ellipsoidal estimate $E(a(t), Q(t))$ of the reachable set $X(t)$ are shown at Figure 3.

The resulting ellipsoidal estimate $E(a(T), Q(T))$ is shown at Figure 4. A parameter ρ indicated at Fig. 4 depends on a type of the optimality criterion which we use in constructing the external ellipsoid $E(a^*, Q^*)$ at the iterations 2-3 of the first step of Algorithm 2, see also Kurzhanski and Valyi[11] and Chernousko[2]. Here we see that the reachable set $X(T)$ is nonconvex and is contained in the ellipsoid $E(a(T), Q(T))$ for any value of the parameter ρ as shown at Fig. 4.

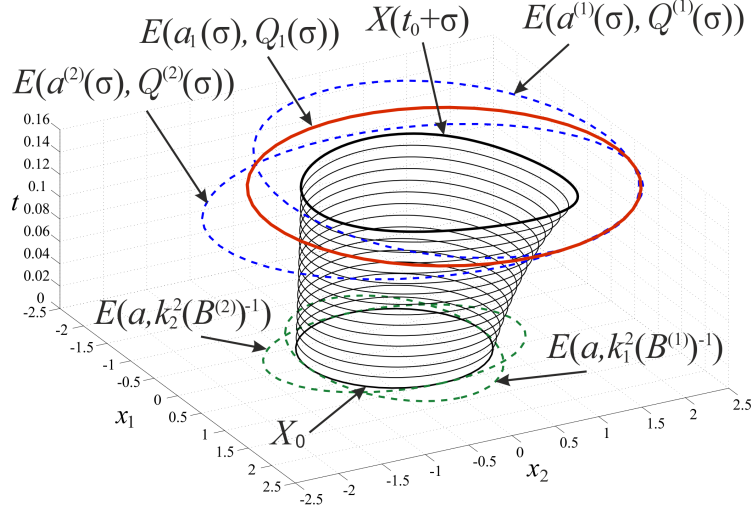


Fig. 3. Reachable set $X(t_0 + \sigma)$ and its estimate $E(a_1(\sigma), Q_1(\sigma))$ at the first step of Algorithm 2 (iterations 1-3).

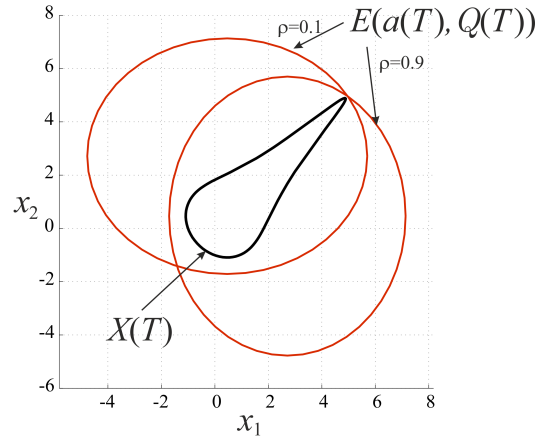


Fig. 4. Reachable set $X(T)$ and its external ellipsoidal estimate $E(a(T), Q(T))$.

3.3 Impulsive systems under uncertainty

Consider the following control system

$$dx(t) = (Ax(t) + \tilde{f}(x)d + u(t))dt + Bdv(t), \quad x \in R^n, \quad t_0 \leq t \leq T, \quad (18)$$

where $\tilde{f}(x) = x'\tilde{B}x$ with positive definite and symmetric matrix \tilde{B} , parameters d, B are n -vectors, $d, B \in R^n$. Here the function $v : [t_0, T] \rightarrow R$ is of bounded variation on $[t_0, T]$, monotonically increasing and right-continuous. We assume that $\mu > 0$ and

$$Var_{t \in [t_0, T]} v(t) = \sup_{\{t_i | t_0 \leq t_1 \leq \dots \leq t_k = T\}} \left\{ \sum_{i=1}^k |v(t_i) - v(t_{i-1})| \right\} \leq \mu.$$

We assume also

$$X_0 = E(a, k^2 \tilde{B}^{-1}) \quad (k \neq 0), \quad U = E(\hat{a}, \hat{Q}). \quad (19)$$

Consider the following auxiliary equation:

$$\frac{d}{d\eta} \begin{pmatrix} z \\ \tau \end{pmatrix} \in H(\tau, z), \quad (20)$$

$$z(t_0) = x_0 \in X_0 = E(a, k^2 \tilde{B}^{-1}), \quad \tau(t_0) = t_0, \quad t_0 \leq \eta \leq T + \mu,$$

$$H(\tau, z) = \bigcup_{0 \leq \nu \leq 1} \left\{ (1 - \nu) \begin{pmatrix} Az + \tilde{f}(z)d + E(\hat{a}, \hat{Q}) \\ 1 \end{pmatrix} + \nu \begin{pmatrix} B \\ 0 \end{pmatrix} \right\}. \quad (21)$$

Denote the reachable set of the system (20)–(21) as $W(t_0 + \sigma) = W(t_0 + \sigma; t_0, X_0 \times \{t_0\})$.

Theorem 3. (Filippova[4]) *The following inclusion holds true for $\sigma > 0$:*

$$W(t_0 + \sigma) \subseteq \bigcup_{0 \leq \nu \leq 1} \begin{pmatrix} E(a^+(\sigma, \nu), Q^+(\sigma, \nu)) \\ t_0 + \sigma(1 - \nu) \end{pmatrix} + o(\sigma)B^{n+1}(0, 1), \quad (22)$$

$$\lim_{\sigma \rightarrow +0} \sigma^{-1} o(\sigma) = 0.$$

Here

$$\begin{aligned} a^+(\sigma, \nu) &= a(\sigma, \nu) + \sigma(1 - \nu)\hat{a} + \sigma\nu B, \\ Q^+(\sigma, \nu) &= (p^{-1} + 1)Q(\sigma, \nu) + (p + 1)\sigma^2(1 - \nu)^2\hat{Q}, \end{aligned} \quad (23)$$

where $p = p(\sigma, \nu)$ is the unique positive root of the equation

$$\sum_{i=1}^n \frac{1}{p + \lambda_i} = \frac{n}{p(p + 1)},$$

and $\lambda_i = \lambda_i(\sigma, \nu) \geq 0$ satisfy the equation $|Q(\sigma, \nu) - \lambda\sigma^2(1 - \nu)^2\hat{Q}| = 0$,

$$\begin{aligned} a(\sigma, \nu) &= a + \sigma(1 - \nu)(Aa + (a'\tilde{B}a)d + k^2d), \\ Q(\sigma, \nu) &= k^2(I + \sigma R)\tilde{B}^{-1}(I + \sigma R)', \quad R = (1 - \nu)(A + 2da'\tilde{B}). \end{aligned} \quad (24)$$

The following lemma explains the construction of the auxiliary differential inclusion (20).

Lemma 3. *(Filippova[4]) The set $X(T) = X(T, t_0, X_0)$ is the projection of $W(T + \mu)$ at the subspace of variables z :*

$$X(T) = \pi_z W(T + \mu).$$

Different variants of algorithms of ellipsoidal estimating for the system similar to (18) basing on the above results are given in Filippova and Matviychuk[9], Matviychuk[12],

Theorem 3 can be generalized to the case of a more complicated form

$$\begin{aligned} dx(t) &= (Ax(t) + f^{(1)}(x)d^{(1)} + f^{(2)}(x)d^{(2)} + u(t))dt + Bdv(t), \\ x &\in R^n, \quad t_0 \leq t \leq T, \end{aligned} \quad (25)$$

where $B \in R^n$, $Var_{t \in [t_0, T]} v(t) \leq \mu$, $d^{(1)}, d^{(2)} \in R^n$ and

$$f^{(1)}(x) = x'B^{(1)}x, \quad f^{(2)}(x) = x'B^{(2)}x.$$

The above generalization is based on a combination of the techniques described above and the results of Filippova[7].

4 Conclusions

The paper deals with the problems of state estimation for uncertain dynamical control systems for which we assume that the initial system state is unknown but bounded with given constraints.

The solution is studied through the techniques of trajectory tubes of related differential inclusions with their cross-sections $X(t)$ being the reachable sets at instant t to control system.

Basing on the results of ellipsoidal calculus developed earlier for linear uncertain systems we present the modified state estimation approaches which use the special nonlinear structure of the control system and allow to construct the external ellipsoidal estimates of reachable sets.

Acknowledgements

The research was supported by the Russian Foundation for Basic Researches (RFBR) under Project 12-01-00043a and by Fundamental Research Program "Dynamical Systems and Control Theory" (Project 12-P-1-1019) of the Presidium of Russian Academy of Sciences (RAS) with the support of Ural Branch of RAS.

References

1. D. P. Bertsekas and I. B. Rhodes. Recursive state estimation for a set-membership description of uncertainty. *IEEE Transactions on Automatic Control*, 16: 117-128, 1971.
2. F. L. Chernousko. State Estimation for Dynamic Systems. CRC Press. Boca Raton, 1994.
3. A. L. Dontchev and F. Lempio. Difference methods for differential inclusions: a survey. *SIAM Review*, 34:263-294, 1992.
4. T. F. Filippova. Sensitivity problems for impulsive differential inclusions. In: *Proc. of the 6th WSEAS International Conference on Applied Mathematics, Corfu Island, Greece, August 17-19*, pages 1-6, Greece, 2004.
5. T. F. Filippova. Set-valued solutions to impulsive differential inclusions. *Mathematical and Computer Modelling of Dynamical Systems*, vol. 11, no.2 , 149-158, 2005.
6. T. F. Filippova. Estimates of Trajectory Tubes of Uncertain Nonlinear Control Systems. *Lect. Notes in Comput. Sci.*, 5910:272-279, 2010.
7. T. F. Filippova. Trajectory tubes of nonlinear differential inclusions and state estimation problems. *J. of Concrete and Applicable Mathematics, Eudoxus Press, LLC*, 8:454-469, 2010.
8. T. F. Filippova. Set-valued dynamics in problems of mathematical theory of control processes. *International Journal of Modern Physics, Series B (IJMPB)*, vol. 26, no. 25, 1-8, 2012.
9. T. F. Filippova and O. G. Matviychuk. Reachable Sets of Impulsive Control System with Cone Constraint on the Control and Their Estimates *Lect. Notes in Comput. Sci.*, 7116:123-130, 2012.
10. A. B. Kurzhanski and T. F. Filippova. On the theory of trajectory tubes a mathematical formalism for uncertain dynamics, viability and control. In A. B. Kurzhanski, editor, *Advances in Nonlinear Dynamics and Control: a Report from Russia, Progress in Systems and Control Theory*, 17:22-188. Birkhauser, Boston, 1993.
11. A. B. Kurzhanski and I. Valyi. Ellipsoidal Calculus for Estimation and Control. Birkhauser, Boston, 1997.
12. O. G. Matviychuk. Estimation Problem for Impulsive Control Systems under Ellipsoidal State Bounds and with Cone Constraint on the Control. *AIP Conf. Proc.*, 1497:3-12, 2012.
13. F. Schweppe. Uncertain Dynamic Systems. Prentice-Hall, Englewood Cliffs, New Jersey, 1973.
14. V. M. Veliov. Second order discrete approximations to strongly convex differential inclusion. *Systems and Control Letters*, 13:263-269, 1989.
15. E. Walter and L. Pronzato. Identification of parametric models from experimental data. Springer-Verlag, Heidelberg, 1997.

Mode locking, chaos and bifurcations in Hodgkin-Huxley neuron forced by sinusoidal current

Himanshu Gangal¹ and Gaurav Dar²

¹ BITS Pilani K K Birla Goa Campus, Goa, India
(E-mail: himanshugangal@gmail.com)

² BITS Pilani K K Birla Goa Campus, Goa, India
(E-mail: gdar@goa.bits-pilani.ac.in)

Abstract. The action potentials in a sinusoidally forced Hodgkin-Huxley neuron are known to possess mode locked or chaotic oscillations depending on the values of forcing parameters. We have numerically studied the spiking dynamics of the sinusoidally forced Hodgkin-Huxley neuron by making fine variations in the amplitude while keeping the frequency fixed. We find that the dynamics of the neuron is far richer than previously known. Increasing the resolution of forcing amplitude (I_0) uncovers $1/m$ mode locked oscillations with increasingly larger values of m . Moreover, a mode locked oscillation of type $1/m$ can exist over multiple disconnected intervals of forcing amplitude. Chaotic oscillations are found interspersed with mode locked oscillations. By varying I_0 we have further explored the transition between qualitatively different types of oscillations. On increasing I_0 , every $1/m$ mode locked oscillation is found to go through a sequence of period doubling bifurcations giving rise to $1/2m, 1/4m, \dots$ mode locked oscillations and finally chaos. Chaotic oscillations further undergo a transition to a $1/m'$ mode locked oscillation through a tangent bifurcation. The observed spiking patterns in mode-locked oscillations are unusual and encode the stimulus strength.

Keywords: Hodgkin-Huxley model, Neurons, Bifurcation.

1 Introduction

Hodgkin Huxley model serves as a paradigm for axonal membranes of spiking neurons. The model arose from the electrophysiological experiments of Hodgkin-Huxley with squid giant axons. Consequently, a lot of experimental work with squid axons and theoretical work with the Hodgkin-Huxley (HH) model has been carried out.

A nerve membrane is an excitable system. An appropriate stimulus evokes a strong response (action potential) resulting in a train of spikes in the membrane potential. For forcing by a steady current, a subcritical Hopf bifurcation causes the rest state of the neuron to become unstable giving rise to a periodic train of spikes (a limit cycle) (Xie *et. al.*[1]). Periodically varying stimuli evoke a rich variety of response. Mode-locked (periodic), chaotic, and quasiperiodic oscillations of membrane voltage have been found in experiments with squid giant axons (Kaplan *et. al.* [2], Matsumoto *et. al.*[3], Aihara and Matsumoto[4], Guttman *et. al.*[5]) and in numerical simulations of the HH model (Lee[6], Borkowski[8], Borkowski[7], Parmananda *et. al.*[9]).

A periodically stimulated neuron does not fire action potentials unless the forcing amplitude is above a threshold value. The threshold amplitude depends on the forcing frequency. The firing threshold curve (in forcing parameter space) of a HH neuron under sinusoidal forcing has been explored extensively. Firing onset occurs through a variety of bifurcation mechanisms (Lee[6]). The firing region in parameter space is dominated by mode locked oscillations of the type 1/1, 1/2, and 1/3 while there is a smaller region that exhibits chaotic oscillations. Bifurcations mechanisms that bring about a change in the mode-locking ratio of the periodic oscillations have not been explored so far. Our work explores this question.

In their simulations Lee[6] carried out a characterization of the HH neuron's firing response in the forcing amplitude-frequency parameter space. However, there exists a strip in parameter space lying between the 1/1 and 1/2 mode locked regions that has not been explored adequately. In order to uncover the bifurcations between various mode-locked oscillations, it is imperative to carry out an exhaustive investigation of this strip. We have found that a complex structure of interwoven periodic and chaotic dynamics connected by period doubling and tangent bifurcations exist in this strip.

2 Hodgkin-Huxley Model

The Hodgkin-Huxley model of an axon describes the dynamics of its membrane voltage (V), activation variable (m) and the inactivation variable (h) of its sodium channels, and the activation variable (n) of its potassium channels. The model consists of the following set of four coupled differential equations

$$C \frac{dV}{dt} = -\bar{G}_{Na} m^3 h (V - V_{Na}) - \bar{G}_K n^4 (V - V_K) - \bar{G}_L (V - V_L) + I_{ext}, \quad (1)$$

$$\frac{dm}{dt} = \alpha_m (1 - m) - \beta_m m, \quad (2)$$

$$\frac{dh}{dt} = \alpha_h (1 - h) - \beta_h h, \quad (3)$$

$$\frac{dn}{dt} = \alpha_n (1 - n) - \beta_n n, \quad (4)$$

where,

$$\alpha_m = \frac{0.1(25 - V)}{\exp[(25 - V)/10] - 1}, \quad \beta_m = 4 \exp[-V/18], \quad (5)$$

$$\alpha_h = 0.07 \exp[-V/20], \quad \beta_h = \frac{1}{\exp[(30 - V)/10] + 1}, \quad (6)$$

$$\alpha_n = \frac{0.01(10 - V)}{\exp[(10 - V)/10] - 1}, \quad \beta_n = 0.125 \exp[-V/80]. \quad (7)$$

Capacitance of the axonal membrane $C = 1\mu F/cm^2$. The reversal potentials of sodium, potassium, and leakage channels are $V_{Na} = 115mV$, $V_K = -12mV$, and $V_L = 10.5995mV$ respectively. The maximal conductances of the membrane for sodium, potassium, and leakage currents are $\bar{G}_{Na} = 120mS/cm^2$, $\bar{G}_K = 36mS/cm^2$, $\bar{G}_L = 0.3mS/cm^2$ respectively. In our work we stimulate the neuron with a sinusoidal current $I_{ext} = I_0 \sin(2\pi\nu_f t)$, where I_0 is the forcing amplitude and ν_f is its frequency.

In our work we choose the frequency $\nu_f = 50Hz$ and the amplitude I_0 is varied in the range $1.6\mu A/cm^2 - 2.0\mu A/cm^2$. At the lower and upper end of this range, the neuron exhibits 1/1 and 1/2 mode locked spiking oscillations (Lee [6]). By carrying out fine variations in the amplitude over this range, we have uncovered a complex dynamical structure between these two periodic spiking oscillations.

We carry out numerical simulations of the Hodgkin-Huxley equations (Eq. 1- 4) using the fourth order Runge-Kutta method. We choose the time step dt in our simulations as $dt = T_f/1000$.

3 Results

Dynamics of forced nonlinear systems are often studied by sampling their phase space trajectory stroboscopically. Following this approach, we sample the phase space trajectory of the HH model once every time period of the sinusoidally varying external current. Doing so, yields a sequence of voltage values $V_0, V_1, V_2, \dots, V_i, \dots$. For periodic oscillations, a repetitive sequence will be present. Let T be the time taken for the neuron's phase space trajectory to complete one full cycle. For periodic oscillations $T_f/T = 1/m$. We will characterize periodic oscillations by this ratio and refer to these as $1/m$ mode locked oscillations. The repetitive sequence of voltage values for a $1/m$ oscillation will contain m distinct values.

We have plotted the stroboscopically generated voltage sequences against the forcing amplitude as a bifurcation parameter. The resulting bifurcation plot is shown in Figure 1 over the amplitude range $I_0 = (1.6 - 2.0)\mu A/cm^2$. Two ends of the plot display the 1/2 and 1/1 mode locked oscillations, known from Lee's work (Lee [6]). This interval is believed to contain a rich dynamical structure (Lee [6], Parmananda *et. al.* [9]) but very few details are known.

Figure 1 shows that the amplitude interval between the known 1/1 and 1/2 oscillations contain many more periodic oscillations. Infact, the interval is dominated by periodic oscillations. On increasing the forcing amplitude from $I_0 = 1.6\mu A/cm^2$ onwards we observe $1/2, 1/3, 1/4, 1/5, \dots, 1/m, 1/(m+1), \dots$ mode locked oscillations. A $1/m$ oscillation contains m branches in the bifurcation diagram. A new branch gets added to the bifurcation diagram on crossing over from a $1/m$ to a $1/(m+1)$ oscillation. Figure 1 suggests the presence of a $1/m$ mode locked oscillation for every positive integer m .

The amplitude interval lying between $1/m$ and $1/(m+1)$ oscillations described above contains a rich dynamical structure not discernible in Fig. 1. We see an instance of this richness on magnifying the amplitude interval lying between $1/3$ and $1/4$ mode locked oscillations (see Fig. 2(a)). This interval

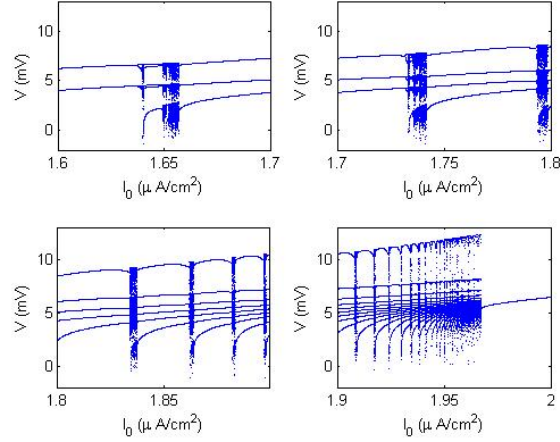


Fig. 1. Bifurcation diagram with variation in forcing amplitude I_0 with forcing frequency fixed to $\nu = 50Hz$.

contains a myriad of periodic and chaotic oscillations. The region between every $1/m$ and $1/(m+1)$ oscillations of Fig. 1 contain such periodic and chaotic oscillations.

In Fig. 2(a)-(b) we observe that the $1/3$ mode locked oscillations (on the extreme left of the figure) undergo a cascade of period doubling bifurcations giving rise to a sequence of $1/6, 1/12, \dots$ oscillations finally converging to chaos. Similar period doubling bifurcations are present in other periodic windows in Fig. 2(a). In general, starting from a $1/n$ periodic window, period doublings will result in $1/(2n), 1/(4n), \dots$ oscillations. Each successive periodic oscillation obtained through period doubling takes double the time to go around its phase space trajectory once. Each cascade of period doublings finally converges to chaos.

Periodic windows in Fig. 2(a) emerge from chaotic oscillations through a tangent bifurcation. The bifurcation is identified by plotting a return map between V_i and V_{i+n} if a $1/n$ mode locked oscillation results from the bifurcation. Close to tangent bifurcation, the return map has n curve segments tangent to a 45° line. After the tangent bifurcation occurs the return map crosses the 45° line at $2n$ points. Half of these points lie on a stable trajectory and the other half like on an unstable trajectory. All periodic windows arise in the same manner. Once a periodic oscillation is created through a tangent bifurcation, the subsequent changes in the qualitative dynamics of the membrane voltage arise from period doubling bifurcation.

Typical spike sequences generated due to sinusoidal forcing are depicted in Figs. 3 and 4. Figure 3(a) shows a $1/3$ mode locked oscillation obtained with forcing parameters chosen from the large region of $1/3$ oscillations in Lee's paper. Here a spike occurs once every three cycles of forcing. In our work we have found a novel set of spike patterns.

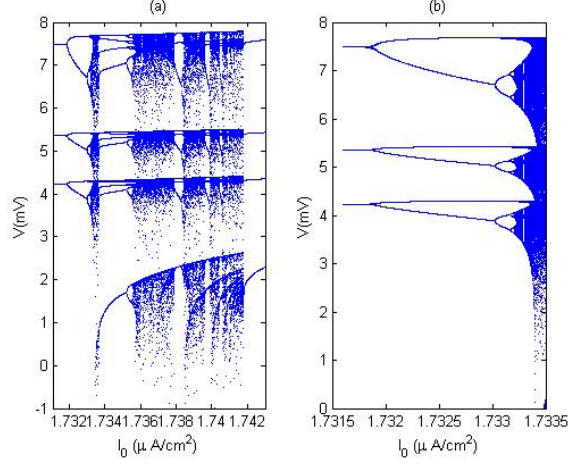


Fig. 2. (a) Bifurcation diagram for the amplitude interval lying between the 1/3 and 1/4 mode locked oscillation of Fig. 1. (b) Panel (a) figure is further magnified over its initial amplitude interval to depict period doubling.

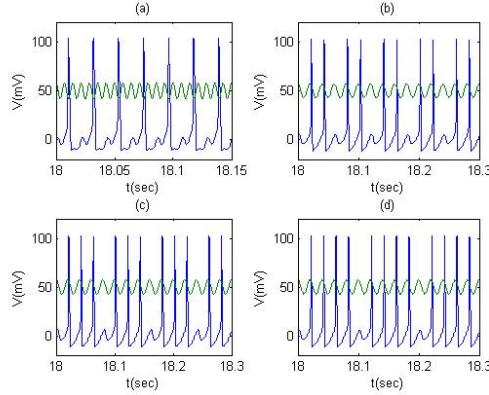


Fig. 3. Some typical spike sequences for periodic oscillations. Each figure gives the result for a different I_0 (in units of $\mu A/cm^2$) and $\nu = 50Hz$. The sinusoidal curve in each figure indicates the profile of this current (a) $I_0 = 4$, (b) $I_0 = 1.7$, (c) $I_0 = 1.78$, (d) $I_0 = 1.82$. Repeating units of spike sequences in (a)-(d) are of form $\{1..\}$, $\{2.\}$, $\{3.\}$, and $\{4.\}$ respectively.

The spike sequences in Fig. 3(b)-(d) are representative of the $1/m$ periodic oscillations that dominate the amplitude interval in Fig. 1. In each of these periodic oscillations, we find that a spike occurs consecutively over $(m - 1)$ forcing cycles, following which there is no spike in the m^{th} forcing cycle. We will represent this spike pattern by $\{(m - 1).\}$, with $(m - 1)$ representing the group of consecutive $(m - 1)$ spikes and the dot $'.'$ representing the missing spike in the m^{th} forcing cycle. The $\{(m - 1).\}$ pattern repeats itself every m forcing cycles and thus we will regard it as a repeating unit. The 1/3 and

1/4 mode locked oscillations in Figs. 3(b) and (c) have $\{2.\}$ and $\{3.\}$ as their repeating units respectively. In contrast, the 1/3 oscillation [Fig. 3(a)] from Lee's work has a repeating unit of the form $\{1..\}$.

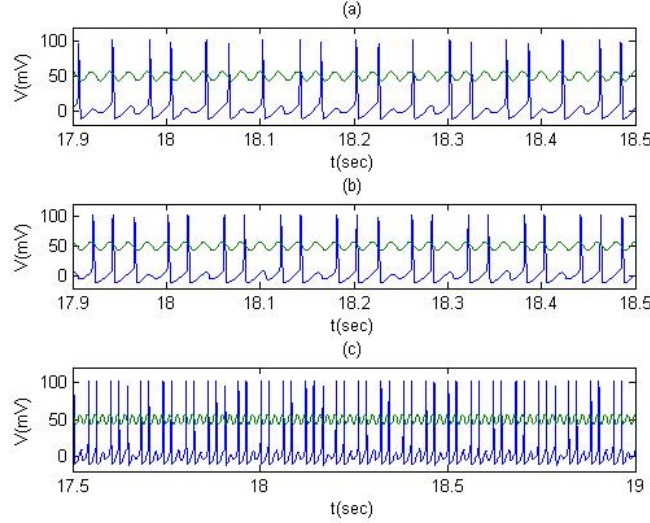


Fig. 4. Each figure gives the result for a different I_0 (in units of $\mu A/cm^2$) and $\nu = 50Hz$. (a) and (b) show some typical spike sequences of the fundamental oscillation of a periodic window. Here $I_0 = 1.6518$ in (a) and $I_0 = 1.7345$ in (b). In (c) we see an intermittent spike sequence for $I_0 = 1.73365$. A few sequences $\{3.2.2.2.\}$ appear intermittently here.

Figure 4 shows spike patterns of oscillations in periodic windows. Here the repeating units have a form different from the ones in Fig. 3. A typical repeating unit is of the form $\{m_1.m_2.m_3.\}$, with multiple groups of spikes, whereas oscillations in Fig. 3 contain only one group of spikes. Here we have shown three groups of spikes containing m_1 , m_2 , and m_3 spikes each separated by a missing spike. However, the number of groups can be more or less (but not less than two) than represented by $\{m_1.m_2.m_3.\}$. Figure 4(a) and (b) shows a 1/8 and 1/13 oscillations with repeating units $\{2.2.1.\}$, and $\{3.2.2.2.\}$ respectively.

Figure 5 shows the typical changes in $V(t)$ that accompany period doubling bifurcations. As an illustrative example we choose the period doubling cascade starting from the 1/3 mode locked oscillation in Fig. 2. The repeating unit is $\{2.\}$ here. We find that the number of spikes per group remain unchanged (equal to two) across all period doubling bifurcations starting from the 1/3 oscillation. However, the amplitudes of spikes undergoes a change. Hence, the repeating unit for 1/6, and 1/12 are $\{2.2.\}$ and $\{2.2.2.2.\}$ respectively. Likewise, in a period doubling of any other periodic oscillation with a repeating unit $\{m_1.m_2.m_3.\}$, every period doubling doubles the length of the repeating unit to $\{m_1.m_2.m_3.m_1.m_2.m_3.\}$.

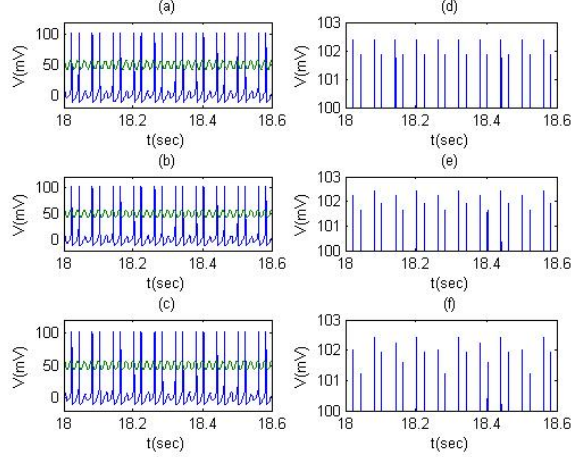


Fig. 5. Changes in the repeating unit of spike sequences across a period doubling bifurcation are shown here. All the figures are plotted for $\nu = 50Hz$ and I_0 is in units of $\mu A/cm^2$ (a) $I_0 = 1.731$ gives $1/3$ mode locking (b) $I_0 = 1.7324$ gives $1/6$ mode locking, and (c) $I_0 = 1.73315$ gives $1/12$ mode locking, (d)-(e) show the variation in spike amplitude for (a)-(c) respectively by plotting $V(t)$ on a smaller scale.

A tangent bifurcation is known to be preceded by intermittency. We find that intermittency occurs through an interesting set of changes in spike patterns as we approach the bifurcation point on varying the forcing amplitude A . Far from the bifurcation point $V(t)$ is chaotic. The spike sequence is of the same form as that for periodic oscillations. However, there exists no repetitive sequence for chaotic oscillations. As the amplitude is brought closer to the bifurcation point the frequency of a specific spike sequence $\{m_1.m_2.m_3.\}$ within the chaotic sequence increases. Once the tangent bifurcation occurs $\{m_1.m_2.m_3.\}$ becomes the repeating unit. Every periodic window arises through a similar increase in the frequency of some unit.

4 Discussion

In the paper we presented a few results of stimulating a HH neuron by a sinusoidal current in the regime where it evokes action potentials. We found a complex structure of $1/m$ mode locked and chaotic oscillations between the $1/1$ and $1/2$ oscillations of Lee's work(Lee[6]). Chaotic oscillations arise through the period doubling route to chaos. Periodic windows emerge through a tangent bifurcation preceded by an intermittent spike sequence. Starting from $1/2$ mode locked oscillations, period doubling cascade gives rise to $1/4, 1/8, \dots$ mode locked oscillations. Across a period doubling bifurcation, spike sequences do not undergo any change. However, the amplitudes of the spikes undergo an alteration. Intermittent spike sequences before a tangent bifurcation contain glimpses of the spike sequences that are finally realized in the periodic oscilla-

tion across the bifurcation. Infact, the neuron enters the $1/1$ oscillation through a tangent bifurcation.

In our work the ratio $1/m$ for a periodic oscillation is the ratio of time taken for one forcing cycle to the time taken for the neuron to go once around its closed orbit in phase space. In going around the limit cycle once the neuron may fire several spikes. However, in literature $1/m$ usually implies that the neuron fires one spike in every m cycles of forcing.

The spike sequences presented in our paper are distinct from those obtained earlier. Spikes are organized in groups where each group may contain a different number of spikes. These sequences of spikes alone can carry information about the forcing amplitude. Implying that no knowledge of the rate of spiking or that of the interspike interval is necessary to extract information about the forcing parameters.

Acknowledgments

This work was supported by computing facilities acquired from funds provided by the BITS Seed grant and DST-FIST grant

References

1. Yong Xie, Luonan Chen, Yan Mei Kang, and Kazuyuki Aihara. Controlling the onset of Hopf bifurcation in the Hodgkin-Huxley model. *Physica Review E*, 77, 061921, 2008.
2. Daniel T. Kaplan, John R. Clay, Timothy Manning, Leon Glass, Michael R. Guevara, and Alvin Shrier. Subthreshold Dynamics in Periodically Stimulated Squid Giant Axons. *Physical Review Letters*, 76, 4074, 1996.
3. Gen Matsumoto, Kazuyuki Aihara, Michinori Ichikawa, and Akira Tasaki . Periodic and nonperiodic responses of membrane potentials in squid giant axons during sinusoidal current stimulation. *J. Theoret. Neurobio.*, 3, 1-14, 1984.
4. Kazuyuki Aihara, Gen Matsumoto. Chaotic oscillations and bifurcations in squid giant axon. In A.V. Holden, editor, *Chaos*, pages 257-269, Princeton, 1986. Princeton University Press.
5. Guttman R, Feldman L, Jakobsson E. Frequency entrainment of squid axon membrane. *J. Membr. Bio.* 21;56(1):9-18, 1980.
6. Sang-Gui Lee and Seunghwan Kim . Bifurcation analysis of mode-locking structure in a Hodgkin-Huxley neuron under sinusoidal current. *Physical Review E*, 73, 041924, 2006.
7. L. S. Borkowski . Bistability and resonance in the periodically stimulated Hodgkin-Huxley model with noise. *Physical Review E*, 83, 051901, 2011.
8. L. S. Borkowski . Response of a Hodgkin-Huxley neuron to a high-frequency input . *Physical Review E*, 80, 051914, 2009.
9. P. Parmananda, Claudia H. Mena, and Gerold Baier. Resonant forcing of a silent Hodgkin-Huxley neuron. *Physical Review E*, 66, 047202, 2002

Gauge Field Turbulence as a Cause of Inflation in Chern-Simons Modified Gravity

David Garrison¹

Department of Physics, University of Houston-Clear Lake, 2700 Bay Area Blvd.,
Houston, TX, USA

(E-mail: garrison@uhcl.edu)

1

Abstract. In this paper, we study the dynamics of the Chern-Simons Inflation Model proposed by Alexander, Marciano and Spergel. According to this model, inflation begins when a fermion current interacts with a turbulent gauge field in a space larger than some critical size. This mechanism appears to work by driving energy from the initial random spectrum into a narrow band of frequencies, similar to the inverse energy cascade seen in MHD turbulence. In this work we focus on the dynamics of the interaction using phase diagrams and a thorough analysis of the evolution equations. We show that in this model inflation is caused by an over-damped harmonic oscillator driving waves in the gauge field at their resonance frequency.

Keywords: Turbulence modeling, Cosmology, Chern-Simons Modified Gravity, Simulation, Chaotic simulation.

1 Introduction

According to accepted cosmological theory, the early universe went through a period of inflation where its size increased by at least 60 e-folds in a small fraction of a second [9]. There is a wealth of observational data providing evidence that inflation occurred [1]. In addition, Inflation is needed to satisfy several fundamental problems in cosmology such as the flatness and horizon problems. Unfortunately, most theories of inflation involve the existence of a scalar field and are difficult to distinguish by observation or experiment. Also, there are still many unanswered questions about where the scalar field came from or why it disappeared after inflation ended. Recently, Alexander et al. [3] suggested a new theory of cosmic inflation based on Chern-Simons modified gravity [4] Unlike scalar field theories of inflation, the theory proposed by Alexander et al. utilizes the interaction between a gauge field and fermion current to drive inflation and does not depend on the existence of a scalar field. This is not the only theory of inflation derived from a vector field interaction [6] but it is unique in that it involves elements that are known to exist in practice and not just in theory.

^{7th} CHAOS Conference Proceedings, 7-10 June 2014, Lisbon Portugal

¹ C. H. Skiadas (Ed)



The Chern-Simons Inflation theory works by suggesting that the energy density from the interaction between the gauge field and fermion current behaves like vacuum energy. This is possible in Chern-Simons modified gravity. The gauge field starts with a random white noise spectrum but then the energy is transported to a few low frequency modes. In the early version of the paper by Alexander et al, the spatial parts of the gauge field and fermion current were used to derive the energy density. They later changed that and based the energy density on the temporal parts of the gauge field and fermion current. This author believes that the motivation for this change may have been the belief that the spatial part of the fermion current dropped to zero too quickly to be effective in driving inflation. We find this to not be the case. We also find that the temporal part of the gauge field and fermion current may not be sufficient to drive a 60 e-fold increase in scale factor.

Our code utilizes the Adler-Bell-Jackiw (ABJ) chiral anomaly [2,5] to model the decrease in fermion current associated with changes in the scale factor and gauge field. This is a small quantum mechanical violation of the conservation of axial-vector current. This violation occurs due to tunneling of fermions from one vacuum to another and is partially responsible for the gentle ending of the inflation event. It is the means by which the gauge field converts to leptons during inflation resulting in lepto-genesis. As the current decreases during inflation, the negative pressure driving inflation should decrease as well unless the decrease in current is offset by an increase in the gauge field.

The overall goal of the study presented here is to understand the dynamics of the system and strengthen our physical interpretation of the theory presented here. The author's previous paper on the Numerical Simulation of Chern-Simons Inflation [7] served to prove the feasibility of the theory. Additional work is being planned to more thoroughly study the version of the theory involving the temporal part of the gauge field and fermion current both alone and in conjunction with the spatial part. In the following sections, we will describe in more detail what we believe is the most promising model of Chern-Simons Inflation as well as the results of computer simulations of this model. In the final section, we will discuss these results and how they may be used in future research.

2 Model and Simulations

The code utilized in these simulations is based on the Cactus framework [8] used for Numerical Relativity research. While Cactus is an extremely sophisticated code containing millions of lines of code, all the physics is contained in code written by the author. This code has been thoroughly tested and the results are self-consistent and reliable.

The inflation model developed by Alexander, Marciano and Spergel utilizes a gauge field which interacts with fermions in the early universe to produce an effective scalar field that generates inflation [3]. See the recent article by Garrison and Underwood for a complete description of how the numerical equations for this model are derived [7].

For the numerical calculation, we use natural units but later evaluate the data in terms of SI units so that the results can be easily compared to the established values. In order to use this model in our code, we separated the equations of motion for the gauge field, ABJ chiral anomaly, Chern-Simons term and the Friedman equations into a system of first order in time differential equations.

$$\frac{d\mathbf{A}}{dt} = \frac{\mathbf{Z}}{a} \quad (1)$$

$$\frac{d\mathbf{Z}}{dt} = \mathbf{J}a^3 + \nabla^2 \mathbf{A}/a - a^2 \frac{\dot{\theta}}{M_*} \mathbf{B} \quad (2)$$

$$\frac{dJ^0}{dt} = \frac{\mathbf{E} \cdot \mathbf{B}}{4\pi^2 a^2} - \nabla \cdot \mathbf{J} - 2HJ^0 \quad (3)$$

$$\frac{dD}{dt} = \frac{\mathbf{E} \cdot \mathbf{B}}{4a^3 M_*^2} - 3HD - 2\frac{m^2}{M_*} \theta \quad (4)$$

$$\frac{d\theta}{dt} = DM_* \quad (5)$$

$$\frac{da}{dt} = aH \quad (6)$$

$$\frac{dH}{dt} = \frac{8\pi}{3} \bar{\rho}/a - H^2 \quad (7)$$

Here the gauge field is represented with \mathbf{A} , the current is \mathbf{J} , a is the scale factor and H is the Hubble parameter. Current is assumed to depend simply on the charge density according to the equation $\mathbf{J} = J^0 \mathbf{v}$. \mathbf{E} represents the hyper charged electric field, $\mathbf{E} \equiv \dot{\mathbf{A}}$. \mathbf{B} is the hyper charged magnetic field, $\mathbf{B} \equiv \nabla \times \mathbf{A}$ term. M_* is the mass scale identified with the UV cut-off scale of the effective field theory and θ is responsible for CP violation. m is on the order of the GUT energy scale. Finally, The average energy density is calculated as $\bar{\rho} = \frac{1}{N} \sum_{k=1}^N \frac{E_k^2 + B_k^2}{2a^4} + |\mathbf{A}_k \cdot \mathbf{J}_k/a|$. Here N represents the total number of grid points in the computational domain. The scale factor and Hubble parameter therefore depend on the average energy density and not the local field dynamics.

The initial gauge field was composed of a random (white noise) spectrum. In order to generate the initial gauge field, we used a random number generator to create a random spectrum with amplitude up to the calculated maximum amplitude, $|\mathbf{A}|$, in each direction. The magnitude of the gauge field was then held equal to the initial amplitude $|\mathbf{A}|$. The initial values for the variables used

in this study are given below.

$$|\mathbf{A}| = 1.0 \times 10^{-5} M_P \quad (8)$$

$$J^0 = 10^{-10} M_P^3 \quad (9)$$

$$\mathbf{v} = 10^{-10}(\hat{x} + \hat{y} + \hat{z}) \quad (10)$$

$$\frac{\dot{\theta}}{M_*} = 2.18 \times 10^{-5} M_P \quad (11)$$

$$a = 1.0 \quad (12)$$

$$H = \sqrt{\frac{8\pi}{3} |\mathbf{A} \cdot \mathbf{J}|} \quad (13)$$

$$\mathbf{Z} = Ha \times \text{random number}(-1, 1) \quad (14)$$

$$m = 4.15 \times 10^{-6} M_P \quad (15)$$

$$M_* = 4.15 \times 10^{-6} M_P \quad (16)$$

The code was then run on the University of Houston's Maxwell cluster using a variety of time-steps, grid sizes and resolutions in order to obtain consistent results. A fourth order finite differencing scheme was used to test convergence for high and low resolution simulations. Because the initial units were entered as Planck units, we assumed that the physical grid (horizon) size corresponded to Planck lengths and the timing output could be interpreted as Planck time.

3 Results

The previous article by Garrison and Underwood [7] focused on demonstrating the feasibility of the model and verifying that the apparent inverse energy cascade occurred as predicted. Previous data have shown that this is an interesting chaotic system which is highly dependent on initial conditions but numerically stable for a large range of initial data. As in the previous paper, Figure 1 shows the life-cycle of the evolution as our virtual universe experiences inflation. This is demonstrated by the scale factor and Hubble parameter.

Fig. 1. The scale factor and Hubble Parameter for the inflationary period (log scale).

Figure 2 shows how the gauge field increases and charge density decreases with time. The net result of this is that the dot product of the gauge field and charge density yields a nearly constant energy density (and therefore Hubble parameter) until inflation ends. The gauge field evolution equation is essentially an inhomogenous wave equation driven by the $\frac{\dot{\theta}}{M_*} \mathbf{B}$ term and the $\mathbf{J}a^3$ term. Understanding how inflation occurs is directly connected to the dynamics of these two terms. The first term is much more dynamic and could explain why inflation begins and ends. Also, given our initial conditions, the first term is $\sim 10^{-5} \mathbf{B}$ while the second term is $\sim 10^{-20}$ so the first term should normally dominate since \mathbf{B} starts around 10^{-9} and increases as quickly as the gauge field.

Fig. 2. The Gauge Field Amplitude and Charge Density (log scale).

Without the θ term Chern Simons modified gravity reduces to ordinary General Relativity and the effective vacuum energy disappears. Much of the gauge field dynamics is therefore the result of the θ term and its time derivatives. The phase diagram in Figure 3 shows that this term acts like a dampened driven harmonic oscillator. The frequency of this system is $\omega = \sqrt{2}m$ the dampening term is $\gamma = \frac{3}{2}H$ and the driving term is $F = \frac{\mathbf{E} \cdot \mathbf{B}}{4a^3 M_*}$. Given our initial conditions, $\omega \approx 10^{-6}$, $\gamma \approx 10^{-12} \rightarrow 10^{-5}$ and F is insignificant because $\mathbf{E} \cdot \mathbf{B}$ is unmeasurably small. This is therefore an under-damped harmonic oscillator that transitions into an over-damped harmonic oscillator as the Hubble parameter increases. The θ term vanishes quickly after γ exceeds ω and the gauge field's rate of growth slows while current continues to decrease at a constant rate resulting in a decreasing energy density and an end to inflation. Maintaining the Chern Simons term, $\frac{\dot{\theta}}{M_*}$, for as long as possible appears to be essential to the inflation process.

Fig. 3. Phase diagram of the θ and $\frac{\dot{\theta}}{M_*}$ terms.

In Figure 4, we see the spectrum of the gauge field as a function of time. Notice that the initial gauge field starts off with an evenly distributed spectrum and then sometime later the spectrum peaks at low frequencies to resemble an inverse energy cascade. Later the peak of the power spectrum moves to higher frequencies as the Chern Simons term decays. The peak follows the changing frequency of the Chern Simons term to maintain resonance until it decays to zero and inflation ends.

Fig. 4. Power Spectral Density of the gauge field at various times. The vertical axis is the log of the deviation from the mean. The horizontal axis is frequency in Plank units.

4 Conclusions

An important result of this study is that we now know why inflation only appears to occur when the computational grid is sufficiently large. Our analysis of the θ term's dynamics show that its natural oscillatory frequency is on the order of 10^{-6} . This corresponds to a grid size of about 10^6 units. If the computational grid is smaller than this minimum, the gauge field cannot come into resonance with the driver θ and explode in amplitude.

Information from this study may also be useful in better determining what initial conditions led to inflation in our universe. By varying the initial condi-

tions, the forcing term, dampening term and frequency of θ may be altered to extend our simulated inflation and better conform to observation.

References

1. P. A. R. Ade *et al.* [BICEP2 Collaboration]. BICEP2 I: Detection Of B-mode Polarization at Degree Angular Scales. arXiv:1403.3985 [astro-ph.CO], 2014.
2. S. Adler. Axial-Vector Vertex in Spinor Electrodynamics. *Physical Review*, 177, 1969.
3. S. Alexander, A. Marciano, and D. Spergel. Chern-Simons inflation and baryogenesis. *Journal of Cosmology and Astroparticle Physics*, 2013, 2013
4. S. Alexander and N. Yunes. Chern-Simons modified general relativity. *Physics Reports*, 480,1-2:1–55, 2009.
5. J. S. Bell and R. A. Jackiw. PCAC puzzle: $\pi^0 \rightarrow \gamma\gamma$ in the σ -model. *IL Nuovo Cimento*, 60A,4, 1969.
6. L. H. Ford. Inflation driven by a vector field. *Physical Review D*, 40,4:967–972, 1989.
7. D. Garrison and C. Underwood. A Numerical Simulation of Chern-Simons Inflation. *Advances in Astronomy*, 2013: 207218, 2013.
8. T. Goodale, G. Allen, G. Lanfermann, J. Massó, T. Radke, E. Seidel and J. Shalf. The Cactus Framework and Toolkit: Design and Applications, Vector and Parallel Processing – VECPAR’ 2002, 5th International Conference, Lecture Notes in Computer Science, Berlin: Springer, 2003. <http://edoc.mpg.de/3341>
9. A. H. Guth. Inflationary universe: a possible solution to the horizon and flatness problems. *Physical Review D*, 23,2:347–356, 1981.

Bifurcations and chaos in discrete-time gonorrhea model

Amalia Gkana¹ and Loukas Zachilas²

¹ Department of Economics, University of Thessaly, Volos, Greece
(E-mail: gkana@uth.gr)

² Department of Economics, University of Thessaly, Volos, Greece
(E-mail: zachilas@uth.gr)

Abstract. A deterministic epidemic model for the spread of gonorrhea is investigated in discrete-time by taking into account the interval between successive clinical cases. It is shown that the discrete-time dynamical system exhibits far more complex dynamics than its continuous analogues. Stability analysis is obtained in order to investigate the local stability properties of the fixed points; it is verified that there are phenomena of Fold and Flip bifurcations. Numerical simulation tools are used in order to illustrate the stability analysis results and find some new qualitative dynamics. We come across the phenomenon of “intermittency route to chaos”. The density of infected individuals goes through quasi-periodicity and a strange attractor appears in the system. Chaos control is obtained in order to see how the male latex condom use during sexual intercourse affects the incidence of gonorrhea. It is shown that male latex condom use stabilizes the chaotic vibrations of the system to a point where the number of infected individuals remains stable and is significantly small or zero, leading to the control of disease.

Keywords: Gonorrhea dynamics, Dynamical system, Bifurcations, Chaotic dynamics, Strange attractor, Chaos control, Serial interval, Male latex condom

1 Introduction

Gonorrhea is one of the oldest known human infections. The organism *Neisseria gonorrhoeae* was first described by Neisser in 1879 and cultivated in 1982 [25]. *Neisseria gonorrhoeae* causes an estimated 62 million cases of gonorrhea worldwide each year [16]. Furthermore, the financial impact of gonorrhea is high. Only the direct medical cost for gonorrhea treatment in the United States is estimated at \$1,051,000,000 annually [9]. Infections due to *Neisseria gonorrhoeae* are a major cause of pelvic inflammatory disease (PID) in the United States. PID can lead to serious outcomes in women such as tubal infertility, ectopic pregnancy, and chronic pelvic pain. In men gonorrhea can cause a painful condition called epididymitis in the tubes attached to the testicles [7]. Further, if left untreated, gonorrhea can also spread to the blood and cause disseminated gonococcal infection (DGI), a condition that can be life threatening. Moreover, the organism *Neisseria gonorrhoeae* has the ability to develop resistance against all clinically useful antibiotics. William Smith [31]

^{7th} CHAOS Conference Proceedings, 7-10 June 2014, Lisbon Portugal

C. H. Skiadas (Ed)

© 2014 ISAST



suggests that we are on the verge of a highly untreatable gonorrhea epidemic. Although gonorrhea was easily cured with antibiotics years ago, however bacteria develop resistance to treatments. Furthermore, the World Health Organization recently put out an alert with regards to the reported cases of resistance to cephalosporin antibiotics - the last treatment option against gonorrhea - in several countries including Australia, France, Japan, Norway, Sweden and the United Kingdom [40]. According to Dr. Manjula Lusti-Narasimhan from the Department of Reproductive Health and Research at WHO, gonorrhea is becoming a major public health challenge due to the high incidence of infections accompanied by dwindling treatment options. And after the failure from this last effective treatment, as there are no new therapeutic drugs in development, if gonococcal infections become untreatable the health implications will be significant. Mathematical models have been widely used from epidemiologists over the years to predict epidemics of infectious diseases. Hethcote and Yorke [20] monograph is an excellent work in the context of gonorrhea transmission dynamics and control. They used nonlinear differential equations to model the transmission dynamics of gonorrhea in a heterosexually-active population with two distinct levels of sexual activity. Continuous-time epidemic models have been widely used over the years in the investigation of the transmission of infectious diseases due to their mathematical tractability ([5], [22], [26]). However, discrete-time models are often directly applicable to time-series data and may represent contacts, which are restricted to a specific time or time period more accurately [4]. Therefore, it may be easier to compare the output of discrete-time models with statistical real-world data. Several works have based their models on difference equations in order to investigate the gonorrhea transmission dynamics ([13], [23]). However, discrete-time SIS epidemic models sometimes are capable of generating complex dynamics such as period-doubling and chaotic behavior, in contrast with continuous-time epidemic models. In this paper we study a discrete-time version of Hethcote and Yorke [20] gonorrhea model using discrete time steps, based on the duration of the serial interval of gonorrhea infection.

2 Basic Gonorrhea Model Description

Hethcote and Yorke [20] studied a continuous-time dynamical system for the spread of gonorrhea. They divided population into two groups, *females at risk* (N_f) and *males at risk* (N_m); and each group into two subgroups, *susceptible females* ($N_f S_f$) & *infective females* ($N_f I_f$) and *susceptible males* ($N_m S_m$) & *infective males* ($N_m I_m$). They modeled the dynamics of the spread of gonorrhea by the 4-dimensional system:

$$\begin{aligned} N_f \dot{S}_f &= -\lambda_f \cdot S_f \cdot N_m I_m + N_f I_f / d_f & N_m \dot{S}_m &= -\lambda_m \cdot S_m \cdot N_f I_f + N_m I_m / d_m \\ N_f \dot{I}_f &= \lambda_f \cdot S_f \cdot N_m I_m - N_f I_f / d_f & N_m \dot{I}_m &= \lambda_m \cdot S_m \cdot N_f I_f - N_m I_m / d_m \end{aligned} \quad (1)$$

where, the sexually active population N_f and N_m is constant and equals the number of susceptible plus the number of infective individuals ($N_f = S_f + I_f$ and $N_m = S_m + I_m$); λ_f and λ_m indicate the transmission rate of infection of susceptible females and males respectively; d_f and d_m indicate the average duration of infection for females and males respectively. Since the population is constant, the system (1) reduces to the 2-dimensional dynamical system:

$$\frac{dI_f}{dt} = \frac{\lambda_f}{r}(1 - I_f)I_m - \frac{I_f}{d_f}, \quad \frac{dI_m}{dt} = r\lambda_m(1 - I_m)I_f - \frac{I_m}{d_m} \quad (2)$$

where, $S_f = 1 - I_f$ and $S_m = 1 - I_m$ since the total population size remains constant and $r = N_f / N_m$. The limiting system (2) has two equilibrium points, a trivial and a non-trivial. If the nontrivial equilibrium point exists, it is asymptotically stable and gonorrhea dies out. If the nontrivial equilibrium point does not exist, then the trivial equilibrium point is asymptotically stable and gonorrhea remains endemic.

3 Discrete Gonorrhea Model

According to Ramani et al. [28], discretizing an epidemic model has the following advantages: (a) the epidemic statistics are collected from given time intervals, not continuously, (b) the discrete-time models provide natural simulators for the continuous-time models, (c) with discrete-time models one can use the entire arsenal of methods that have been developed for the study of mappings and lattice equations, either from integrability and/or chaos points of view. There are several ways to discretize a continuous-time model. However, the approach of discretizing the differential equations of a dynamical system has the advantage that can keep track of the known properties of the continuous time system [19].

Thus, in order to discretize Hethcote and Yorke model, we replace dI_f / dt and dI_m / dt by the difference quotients $(I_{n+1}^f - I_n^f) / \delta$ and $(I_{n+1}^m - I_n^m) / \delta$ in the dynamical system (2). Time is measured in “generations”. We obtain a deterministic discrete gonorrhea model defined by the 2-dimensional map:

$$I_{n+1}^f = I_n^f + \delta \left(\frac{\lambda_f}{r}(1 - I_n^f)I_n^m - \frac{I_n^f}{d_f} \right), \quad I_{n+1}^m = I_n^m + \delta \left(r\lambda_m(1 - I_n^m)I_n^f - \frac{I_n^m}{d_m} \right) \quad (3)$$

where, δ is the length of each discrete-time step, where the number of infective individuals grow by the addition of the newly infective individuals; I_n^f , I_n^m is the number of infective females and males in one time step respectively; I_{n+1}^f , I_{n+1}^m is the number of infective females and males at the next time step respectively; the infection rates of susceptible males and females (λ_f , λ_m) indicate the average number of individuals with whom an infectious individual makes adequate contact¹ during a unit time interval [3]. The map (3) has two fixed

¹ Adequate contact is a direct or indirect contact that is sufficient for transmission of infection, if the individual contacted is susceptible. The concept of a sufficient contact is

points, which are identical to the equilibrium points of the analogous continuous model (2), a disease-free equilibrium E_1 and an endemic equilibrium E_2 :

$$E_1 : (I_f^*, I_m^*) = (0, 0), \quad E_2 : (I_f^*, I_m^*) = \left(\frac{\lambda_f \lambda_m d_f d_m - 1}{\lambda_m d_m r + \lambda_f \lambda_m d_f d_m}, \frac{(\lambda_f \lambda_m d_f d_m - 1)r}{\lambda_f \lambda_m d_f d_m r + \lambda_f d_f} \right)$$

In order to study² the local behavior around each of the two fixed points, we calculate the Jacobian matrix at E_1, E_2 . If λ_1, λ_2 are the eigenvalues of the Jacobian matrix at each fixed point, then the fixed point is stable, if $|\lambda_1| < 1$ and $|\lambda_2| < 1$. By using Vieta's equations: $\lambda_1 + \lambda_2 = \text{Tr}(J)$, $\lambda_1 \cdot \lambda_2 = \text{Det}(J)$ (i.e. $\text{Tr}(J)$ and $\text{Det}(J)$ are the trace and the determinant of the Jacobian matrix) and applying Jury's conditions [21], the fixed point is linearly asymptotically stable if and only if:

$$-\text{Tr}J(I_f^*, I_m^*) < 1 + \text{Det}J(I_f^*, I_m^*), \quad \text{Tr}J(I_f^*, I_m^*) < 1 + \text{Det}J(I_f^*, I_m^*) \quad \text{and} \quad \text{Det}J(I_f^*, I_m^*) < 1$$

5 Numerical Simulations for the Discrete-Time Model

A series of numerical simulations³ (using the numerical simulation tools: *parametric basins of attraction*, *bifurcation diagrams*, *phase plots* and *Lyapunov exponent diagrams*) are introduced in order to illustrate the results of the analytical stability analysis and to find some new qualitative dynamics of the discrete-time model (3) as the parameters are varied. The rates of infection λ_m and λ_f should be different, because transmission efficiency is gender dependent. The average probability of transmission of gonococcal infection during a single sexual exposure (a) from an infectious woman to a susceptible man is estimated to be about 0.2 – 0.3, while (b) from an infectious man to a susceptible woman is about 0.5 – 0.7 [37]. Hence, we use the following values for the rate of infection parameters: $\lambda_f = 0.6$ and $\lambda_m = 0.25$. However, the probability of transmission of gonococcal infection is increased for individuals, who have ever had gonorrhea or other STI, for individuals who are street-involved youth and for individuals having sex with many partners, with sex workers, or with a partner coming from a country where gonorrhea is frequent [17]. The average durations of infection d_m and d_f have also to be different, because (a) 90% of all the men who have had gonococcal infection notice symptoms within a few days after exposure and promptly seek medical treatment, while (b) up to 75% of women with gonorrhea fail to have symptoms and remain untreated for some time [27]. In particular, when symptoms occur in men, they usually occur 3-5 days after sexual contact with an infected individual; while women, who develop symptoms, usually experience them within 10 days of sexual contact

necessary since transmission of infection sometimes does not occur during sexual intercourse between an infective and a susceptible [20].

² The results of the stability analysis have been exhibited by using the software package *wxMaxima 12.04.0* (<http://maxima.sourceforge.net/>).

³ Numerical simulations have been exhibited by using the software E&F Chaos 1.02 [12].

with an infected individual [38]. So we fix the average duration of infection for females and males at $d_f = 10$ and $d_m = 3$ respectively.

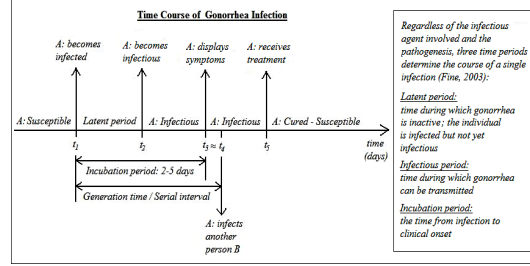


Fig. 1. Time course of a single gonorrhea infection; Individual A becomes infected, transmits the infection to individual B and receives treatment.

Gonorrhea affects males and females almost equally⁴. So we assume that the number of males and females at risk (N_m, N_f) is equal with ratio $r = 1$. We also assume that the initial number of infective individuals is the same both for males and females. Therefore, we use for initial conditions the values $(I_o^f, I_o^m) = (0.5, 0.5)$. Finally, in order to accurately describe the gonorrhea transmission dynamics, the size of the discrete time step should match the epidemiology of the disease [34]; that is, whether the dynamic of infection is a matter of days or hours. Thus, we assume that the discrete time step δ corresponds to the generation time of gonorrhea, that is, the time from the moment one person becomes infected until that person infects another person [29]. This time interval is well-known as the serial interval (Figure 1), that is, the time period between successive clinical cases [14]. In other words, this is the average time between the observation of symptoms of gonorrhea in one person and the observation of symptoms in another person that has been infected from the first. The serial interval is important in the interpretation of infectious disease surveillance and trend data, in the identification of outbreaks and in the optimization of quarantine and contact tracing [14]. Furthermore, the symptoms of gonorrhea usually appear two to five days after infection (i.e. incubation period) [25]. Thus, since an infected individual remains infectious until he/she receives treatment, we assume that infections occur during the infectious period (Figure 1). Moreover, although a range of values for the serial interval is possible, the average serial interval can be estimated as: *(average incubation period) + (half the average infectious period)*, assuming that the maximum infectiousness occurs at the middle of the infectious period [30]. So the serial interval could be estimated by the incubation period. Therefore we define the length of the discrete time step between infection and subsequent transmission as $2 < \delta < 5$ days. Using these values for our parameters, we observe that the dynamics of the basic model (2) alters significantly in discrete time for time

⁴ Global estimated incidence of gonorrhea, occurred in 1999, is 62.35 million infected people annually. Particularly gonorrhea affected 33.65 women and 28.70 men [39].

interval length between successive clinical cases ($2 < \delta < 4$) days, as the rate of infection of susceptible females increases (Figure 2).

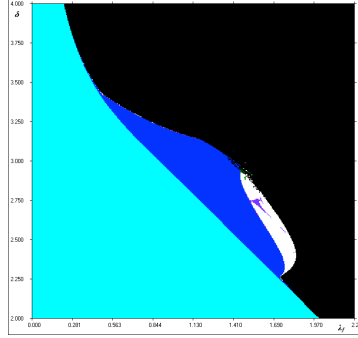


Fig. 2. The basins of attraction diagram for $\delta \in [2, 4]$ and $\lambda_f \in [0, 2.25]$.

For small values of the infection rate parameter ($0 < \lambda_f < 0.4$), the solutions converge either to a disease-free fixed point or to an endemic fixed point (light-blue area) for every value of time interval between clinical cases. For average values of the infection rate parameter ($0.4 < \lambda_f < 1.46$), as λ_f increases, the light-blue area is being replaced with the dark-blue area and the solutions converge to an attracting cycle of period 2. Moreover, for specific step size values ($2.25 < \delta < 3$), further increase in the infection rate parameter λ_f gives rise to non-periodic behavior (white area). For large values of the infection rate parameter ($\lambda_f > 1.85$) as the value of λ_f increases, any periodic and non-periodic behavior is being replaced with divergence to infinity (black area). This abrupt behavior is not meaningful, but it could be taken as some kind of catastrophe causing the extinction of the infected population. Thus, for sufficiently low infection rate of susceptible females, the behavior of solutions of the discrete-time model is qualitatively the same with the basic model. However, as the infection rate increases, the discrete-time model exhibits the same behavior as the continuous-time model only for certain short time interval between successive clinical cases of gonorrhea ($\delta < 2.25$).

Fixing the time period between clinical cases at $\delta = 2.65$ ($2 < \delta < 4$ days) and let the rate of infection of susceptible females parameter increasing in the interval $\lambda_f \in [0, 1.59]$, we observe bifurcations occurring in the system (Figure 3).

The value $\lambda_f \approx 0.1333$ is a bifurcation point at which a “fold” bifurcation occurs: For exceptionally small values of the varying parameter ($\lambda_f < 0.1333$), the disease-free fixed point $E_1: (0, 0)$ is locally asymptotically stable (stable node) and the endemic (negative) fixed point $E_2: (I_f^*, I_m^*)$ is unstable (saddle). Some solutions converge to the attracting disease-free fixed point; there are no infective individuals and gonorrhea dies out. Hence, the initial infective population sizes $(I_f^0, I_m^0) = (0.5, 0.5)$ lead to the extinction of the disease due to the low probability of infection. Near the value $\lambda_f \approx 0.1333$ both fixed points $E_1: (0, 0)$ and $E_2: (-0.0001, -0.0001)$ undergo a “fold” bifurcation and become non-hyperbolic with eigenvalues of the Jacobian matrix ($\lambda_1 = -0.1483$, $\lambda_2 =$

0.9999 \approx +1) and ($\lambda_1 = -0.1483$, $\lambda_2 = 1.0001 \approx +1$) respectively. Hence, for this critical value, the system has only one non-hyperbolic fixed point $E_1 \approx E_2$: (0, 0). For $0.1333 < \lambda_f < 1.1035$, the system has again two fixed points, the trivial and a non-trivial positive fixed point. The fixed points have exchanged their stability. The disease-free fixed point E_1 is now unstable (saddle), while the endemic fixed point E_2 is locally asymptotically stable (stable node). The initial infective population sizes $(I^f_0, I^m_0) = (0.5, 0.5)$ converge to the attracting endemic fixed point, where both infected males and females are fixed in time. Moreover, the number of infective females is larger than the number of infective males ($I^*_f > I^*_m$) likely due to the fact that the infection rate of females is larger than the infection rate of males ($\lambda_f > \lambda_m$) and the duration of infection is larger in females than in males ($d_f > d_m$). As the parameter λ_f increases in this interval, the number of infective individuals (I^*_f, I^*_m) increases continuously and gonorrhea remains endemic. Near the value $\lambda_f \approx 1.1035$ the saddle disease-free fixed point E_1 : (0,0) becomes non-hyperbolic ($\lambda_1 = -0.9999$, $\lambda_2 = 1.8516$) and for $\lambda_f > 1.1035$ is an unstable node. The value $\lambda_f \approx 1.2961$ is a bifurcation point at which a “flip” bifurcation occurs: At $\lambda_f \approx 1.2961$ the endemic fixed point E_2 : (0.8329, 0.3845) undergoes a “Flip bifurcation” and becomes non-hyperbolic with eigenvalues of the Jacobian matrix ($\lambda_1 = -0.9999 \approx -1$, $\lambda_2 = -0.0207$). For $1.2961 < \lambda_f < 1.59$ the endemic fixed point E_2 becomes unstable (saddle) and a stable cycle of period 2 appears in the system. Both infective males and females, now, converge to different 2-period cycles, while both periodic cycles become wider, as the parameter increases at this particular interval.

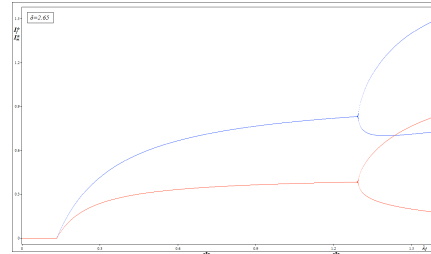
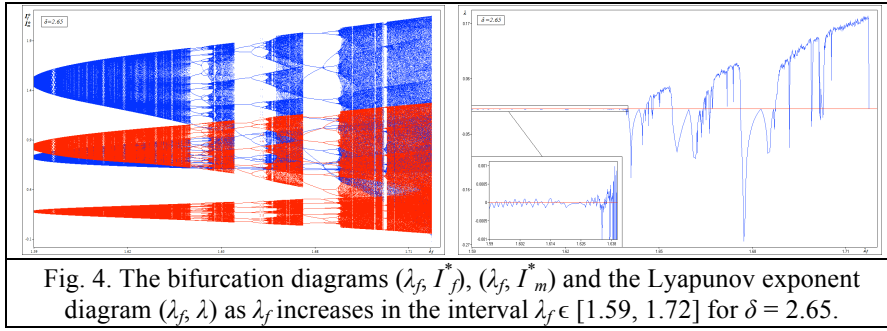


Fig. 3. The bifurcation diagrams (λ_f, I^*_f) and (λ_f, I^*_m) for $\delta = 2.65$ as λ_f increases in the interval $\lambda_f \in [0, 1.59]$.

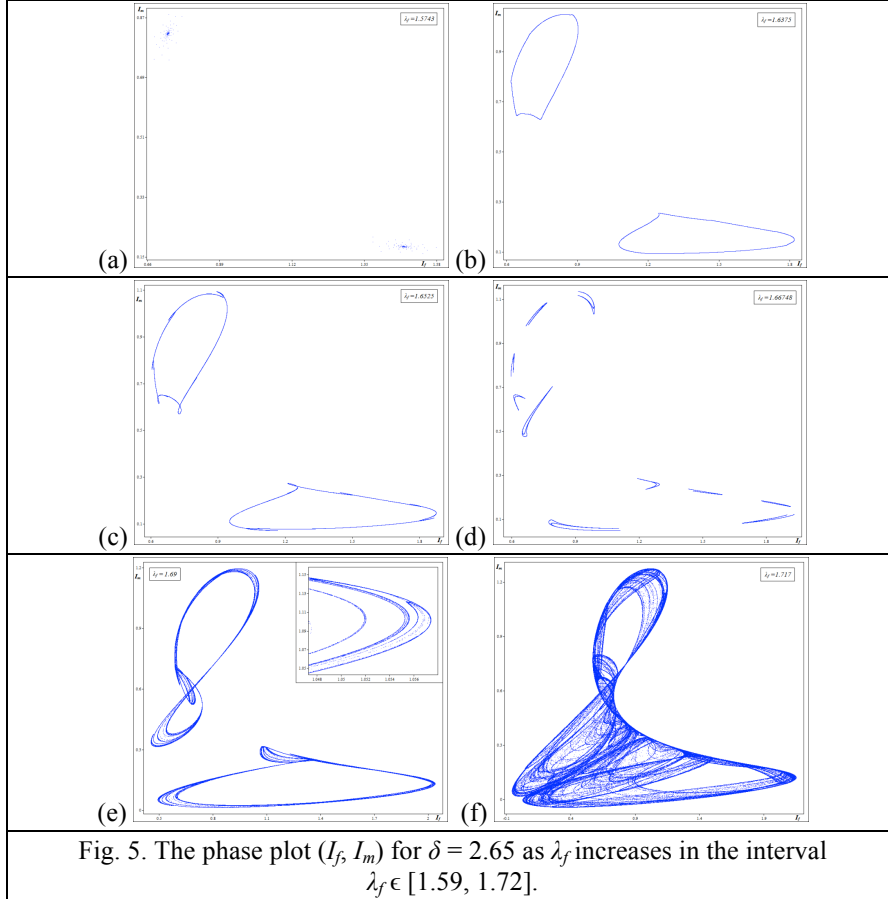
For higher values of the rate of infection of susceptible females $\lambda_f \in [1.59, 1.72]$, we come across the phenomenon of “*intermittency route to chaos*”, which according to Manneville and Pomeau [24], is characterized by regular (laminar) phases alternating with irregular bursts. In particular, as the varying parameter increases, the endemic fixed point remains unstable (saddle), while periodic behavior of high periods, cascades of period-doubling bifurcations and deterministic chaos appear eventually in both infected males and females (Figure 4). For $1.59 < \lambda_f < 1.6402$ the Lyapunov exponents vary among negative and exceptionally small positive values $\lambda_i^+ < 0.001$ and the behavior of solutions appears to be slightly chaotic. For $1.6402 < \lambda_f < 1.6544$ the map exhibits the familiar infinite sequence of period-doubling bifurcations ($32 \cdot 2^n$): (32-period

cycle, 64-period cycle, 128-period cycle, etc.) followed by chaotic oscillations, where the Lyapunov exponents take higher positive values $\lambda_i^+ < 0.05$. At $\lambda_f \approx 1.6544$ a second series of period-doubling bifurcations ($10 \cdot 2^n$): (10-period cycle, 20-period cycle, 40-period cycle, etc.) route to chaos once again, while the Lyapunov exponents at this parameter interval ($1.6544 < \lambda_f < 1.6763$) vary among larger positive values $\lambda_i^+ < 0.1$. At $\lambda_f \approx 1.6763$ another series of period-doubling bifurcations ($12 \cdot 2^n$): (12-period cycle, 24-period cycle, 48-period cycle, etc.) lead to even more chaotic behavior, where the oscillations in the density of infected individuals can be hard to predict. The Lyapunov exponents take even larger positive values and reach the maximum value $\lambda_{\max} \approx 0.1849$ for the parameter value $\lambda_f \approx 1.7172$ for which the variations in the number of gonorrhea cases are the less predictable (fully developed chaos). At this point, the exceptionally high infection rate of susceptible females leads the number of infected individuals sometimes close to extinction and other times close to overgrowth (i.e. gonorrhea outbreaks).



Furthermore, as the rate of infection of susceptible females increases in the interval $\lambda_f \in [1.59, 1.72]$ for the same time interval between clinical cases ($\delta = 2.65$), the system goes through quasi-periodicity and a strange attractor appears in the system (Figure 5). The stable period-2 orbit (Figure 5.a) near the value $\lambda_f \approx 1.59$ loses stability via a supercritical Neimark-Sacker bifurcation, giving rise to two attracting closed invariant curves. At this point the number of infected males and females oscillates between all the states of the two invariant curves. The invariant curves grow in size (i.e. the amplitudes of oscillations in the number of infected individuals are increasing), interact with the saddle non-trivial fixed point $(I_f^*, I_m^*) \approx (0.86, 0.39)$ and near the value $\lambda_f \approx 1.6375$ become noticeably kinked (Figure 5.b). The kinked curves have a split, lock into a stable periodic orbit due to the first sequence of period-doubling occurring in the system ($32 \cdot 2^n$) and reappear slightly deformed (Figure 5.c). They have another split, due to the second series of period-doubling ($10 \cdot 2^n$), which gives rise to a motion of period-10 (Figure 5.d). The motion of period-10 forms into two weakly chaotic contiguous bands (Figure 5.e), while successive enlargements of the attractor can show its fine structure, which looks identical in all scales (i.e. self-similarity). The chaotic contiguous bands become more and more

complicated, merging to form a strange attractor (Figure 5.f) for a value of the varying parameter ($\lambda_f \approx 1.717$) in the chaotic domain (Figure 4). For higher values of the infection rate parameter, the successive iterates diverge to infinity (i.e. both infected males and females become extinct through some kind of catastrophe) and the attractor disappears.



So, we observe that the behavior of the discrete-time gonorrhea model (3) differs significantly from its continuous counterpart (2). Particularly, a time period $2 < \delta < 4$ days between successive clinical cases of gonorrhea and a sufficiently large infection rate of susceptible females allow for infinite sequences of period-doubling and chaotic behavior in the density of infected individuals.

6 Chaos Control

Chaos may be undesirable, as the chaotic oscillations in the density of infected individuals can make the disease uncontrollable and, consequently, harmful to the people's health throughout the world. Therefore, the number of infected individuals needs to be under control. A method of controlling chaos has been proposed by Güémez and Matias [18], known as the G.M. algorithm⁵, which performs changes in the system variables allowing the stabilization of chaotic behavior. In addition, Codreanu and Danca [11] applied the G.M. method to a prey-predator model supporting its use in biological systems. The G.M. control algorithm consists of the application of a proportional feedback⁶ (γ) to the variables of the system in the form of pulses [18]. We apply the G.M. control algorithm to the discrete map (3) by modifying the system variables I_n^f, I_n^m in the following form: $I_n^f \rightarrow I_n^f(1+\gamma_1)$, $I_n^m \rightarrow I_n^m(1+\gamma_2)$. Hence, our discrete-time gonorrhea model (3) becomes:

$$\begin{cases} I_{n+1}^f = I_n^f(1+\gamma_1) + \delta \left(\left(\lambda_f / r \right) (1 - I_n^f(1+\gamma_1)) I_n^m(1+\gamma_2) - (I_n^f(1+\gamma_1)/d_f) \right) \\ I_{n+1}^m = I_n^m(1+\gamma_2) + \delta \left(r \lambda_m (1 - I_n^m(1+\gamma_2)) I_n^f(1+\gamma_1) - (I_n^m(1+\gamma_2)/d_m) \right) \end{cases} \quad (4)$$

where, γ_1, γ_2 represent the strength of the feedback for I_f, I_m . For sexually active persons, male latex condoms are the most commonly used contraceptive method to prevent⁷ sexually transmitted infections [10]. So from a practical point of view, the modification in the system variables could be interpreted as the use of male latex condoms during each sexual intercourse. Hence, the new terms $\gamma_1 I_n^f, \gamma_2 I_n^m$ are associated with condom use during sexual intercourse protecting males and females from gonorrhea transmission and reducing the number of infected individuals ($-1 \leq \gamma_1, \gamma_2 < 0$), while the terms I_n^f, I_n^m are associated with sexual intercourse without condom use. Furthermore, for the sake of simplicity, we assume that the protection from gonorrhea transmission by condom use from female to male and vice versa is the same ($\gamma_1 = \gamma_2 = \gamma$). The condition $\gamma = -1$ corresponds to an ideal situation where all sexually-active individuals use latex condoms during sexual intercourse consistently and correctly.

Thus, in order to see how the condom use affects the incidence of gonorrhea, we apply the G.M. method for the parameter values $\delta = 2.65$ and $\lambda_f = 1.717$ (the other parameters remain unchanged) for which the system's behavior is chaotic (Figure 5.f). Let the control parameter (γ) to vary. We illustrate the results by plotting the bifurcation diagram (Figure 6) along with the time series before ($\gamma = 0$) and after ($\gamma < 0$) the action of chaos control algorithm (Figure 7). Without condom use during sexual intercourse ($\gamma = 0$) the number of infective males and females appears irregular oscillations (Figure 7). As the intensity of pulses increases (i.e. condom use increases), the control parameter (γ) is taking smaller

⁵ Güémez and Matias [18] considered the logistic map and the exponential map.

⁶ Depending on the sign of γ , in particular, some part of the system variables is injected or withdrawn depending on the value of the variables at the moment n [18].

⁷ In vitro studies indicate that latex condoms provide an effective mechanical barrier to passage of infectious agents comparable in size to or smaller than STI pathogens [8].

and smaller negative values, some part of I_f or I_m is injected from the map depending on the value of I_n^f or I_n^m at that moment and through sequences of reverse period-doubling bifurcations, the chaotic domains give rise to regular behavior (Figure 6), where the oscillations in the density of infected individuals become predictable. Particularly, near the value $\gamma \approx -0.066$ the behavior of solutions becomes periodic (cycle of period-2). In the parameter interval $-0.5432 < \gamma < -0.2091$ solutions converge to endemic equilibrium (Figure 7).

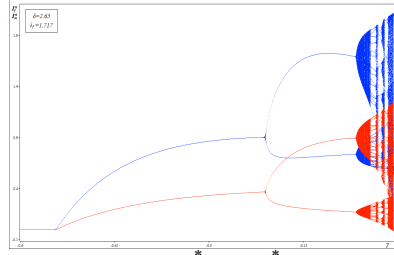


Fig. 6: The bifurcation diagrams (γ, I_f^*) , (γ, I_m^*) as γ decreases in the interval $\gamma \in [-0.6, 0]$, for $\delta = 2.65$ and $\lambda_f = 1.717$.

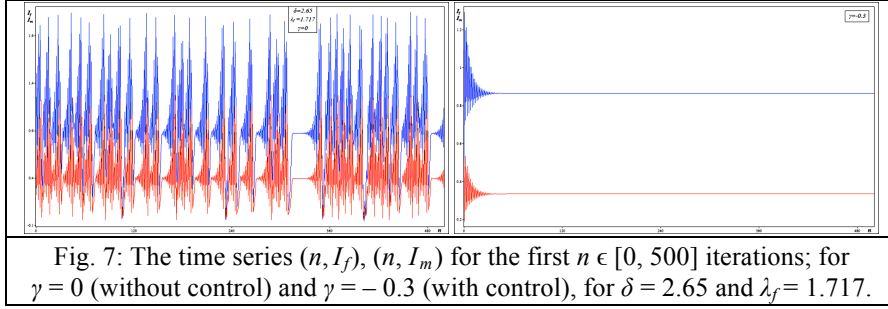


Fig. 7: The time series (n, I_f) , (n, I_m) for the first $n \in [0, 500]$ iterations; for $\gamma = 0$ (without control) and $\gamma = -0.3$ (with control), for $\delta = 2.65$ and $\lambda_f = 1.717$.

Finally, the decline in the number of infective individuals leads to the end of the disease (gonorrhea-free equilibrium) for $-1 < \gamma < -0.5432$ (Figure 6). Hence, for exceptionally high infection rate of susceptible females and time interval between clinical cases $2 < \delta < 4$ days, as the condom use during sexual intercourse increases slowly among individuals, the oscillations in the number of infective males and females decrease rapidly, leading to the reduction of gonorrhea incidence and the control of disease. So, we observe that condom use, just by a fraction of the population 50%, can reduce substantially the risk of gonorrhea transmission even for exceptionally high infection rates.

Concluding Remarks and Discussion

In this paper we have discretized the gonorrhea model of Hethcote and Yorke [20] and studied its dynamical characteristics using as a discrete-time step the interval between successive clinical cases (i.e. serial interval). We showed that the discrete-time model could result in a much richer set of patterns than the corresponding continuous-time model. The analytical stability analysis and the

numerical simulation results showed that the discrete-time model undergoes: “fold”, “flip” bifurcations and the number of infective males and females can behave chaotically. In particular, we showed that: (a) for low rate of infection of susceptible females gonorrhea remains endemic or dies out, while (b) for high rate of infection of susceptible females chaotic oscillations and gonorrhea outbreaks appear in the system.

The results of our study reflect the real-world large fluctuations, which appear in the number of gonorrhea cases throughout the years. For instance, in Sweden from 2007 to 2011 the number of gonorrhea cases increased by 48% (from 642 to 951 cases) [35]. The factors that might have been contributed to this increase in gonorrhea incidence seem to be: (a) the increased number of sexual partners over time, (b) the increased number of new casual sexual partners and (c) the low level of condom use with casual sexual partners [33]. Moreover, Alaska’s outbreak of *Neisseria gonorrhoeae* (GC) infection began in 2008 and peaked in 2010 with a total 1,273 GC cases reported to Alaska Section of Epidemiology [2]. The 2009 case rate demonstrated a 69% increase from the 2008 rate, representing the greatest single-year increase in reported GC infection in Alaska since the 1970s; the rate increased in both sexes, among all races, in all age groups and in nearly all regions of the state [1]. Another example is the variations in the number of gonorrhea cases in the Onondaga County, NY, USA. According to the Onondaga County Health Department (OCHD) the number of cases of gonorrhea more than doubled in the county between 2011 and 2012. There were 602 cases in the first nine months up from 253 cases for the same period of 2011 [32]. Hence, the proposed discrete-time model seems to be more effective in practice and gonorrhea, despite the fact that it is a non-fatal disease, is likely to have a strong negative effect on life history evolution. Moreover, the results of our study show that the time interval between successive clinical cases is important in case of gonorrhea emergency situations. However, few are known about clinical onset serial intervals of gonorrhea. Therefore, collected data on serial intervals of gonorrhea could provide useful information to guide any public health action.

Moreover we have stabilized the unstable periodic orbits, existing within the strange attractor and the unstable steady states (both endemic and disease-free), using a series of proportional feedbacks on the system’s variables. The chaos control results could be definitely regarded as those, which are obtained with the use of male latex condom during sexual intercourse. Our chaos control results show that condom use reduces the risk of gonorrhea transmission to a point where the number of infected individuals remains stable and is significantly small or zero. This reflects what many studies have shown, such as Barlow’s study [6], which showed that a 71% reduction in gonorrhea was associated with consistent and correct condom use (i.e., for every 100 cases of gonorrhea infection that would happen without condom use, only 29 would happen when condoms are used consistently). However, one of the paradoxes in modeling infectious diseases is that, despite their quantitative nature, the best that we can often expect is qualitative insights [15]. Quantifying the relation between the

number of condoms used and the incidence of gonorrhea is often difficult. For instance, Warner et al. [36] reviewed studies, published from 1966 to 2004, to assess risk reduction for gonorrhea associated with male condom use. They found that, although most studies showed that condom use was associated with reduced risk for gonorrhea among men and women, however the exact magnitude of risk reduction is difficult to quantify because of limitations and variations in the methods and design of these studies.

References

1. Alaska Section of Epidemiology (SOE). Statewide Increase in Gonococcal Infection - Alaska, 2009. Bulletin no. 6, March 9, 2010.
2. Alaska Section of Epidemiology (SOE). Gonococcal Infection - Alaska, 2011. Bulletin no. 11, June 21, 2012.
3. L.J.S. Allen, M.A. Jones and C.F. Martin. A discrete-time model with vaccination for a measles epidemic. *Mathematical Biosciences*, 105, 1, 111{131, 1991.
4. L.J.S. Allen, N. Kirupaharan and S.M. Wilson. SIS Epidemic Models with Multiple Pathogen Strains. *Differential Equations & Applications*, 10, 1, 53{75, 2004.
5. N.T.J. Bailey. *The Mathematical Theory of Infectious Diseases*. Hafner Press, 2nd edition, New York, 1975.
6. D. Barlow. The condom and gonorrhoea. *The Lancet*, 310, 8042, 811{813, 1977.
7. R.E. Berger, E.R. Alexander, J.P. Harnisch, C.A. Paulsen, G.D. Monda, J. Ansell and K.K. Holmes. Etiology, manifestations and therapy of acute epididymitis: prospective study of 50 cases. *Journal of Urology*, 121, 6, 750{754, 1979.
8. R.F. Carey, C.D. Lytle and W.H. Cyr. Implications of laboratory tests of condom integrity. *Sexually Transmitted Diseases*, 26, 4, 216{220, 1999.
9. Centers for Disease Control and Prevention (CDC). Tracking the Hidden Epidemic: Trends in STDs in the United States. 2000.
10. Centers for Disease Control and Prevention (CDC). Sexually transmitted diseases treatment guidelines. *MMWR Recommendations and Reports*, 51, RR-6, 1{78, 2002.
11. S. Codreanu and M. Danca. Control of Chaos in a Nonlinear Prey-Predator Model. *Polish Journal of Environmental Studies*, 6, 1, 21{24, 1997.
12. C. Diks, C. Hommes, V. Panchenko and R. van der Weide. E&F Chaos: A user-friendly software package for nonlinear economic dynamics. *Computational Economics*, 32, 1-2, 221{244, 2008.
13. Y. Enatsu, Y. Nakata and Y. Muroya. Global stability for a discrete SIS epidemic model with immigration of infectives. *Journal of Difference Equations and Applications*, 18, 11, 1913{1924, 2012.
14. P.E.M. Fine. The interval between successive cases of an infectious disease. *American Journal of Epidemiology*, 158, 11, 1039{1047, 2003.
15. G.P. Garnett. An introduction to mathematical models in sexually transmitted disease epidemiology. *Sexually Transmitted Infections*, 78, 7{12, 2002.
16. A.C. Gerbase, J.T. Rowley, D.H. Heymann, S.F. Berkley and P. Piot. Global prevalence and incidence estimates of selected curable STDs, *Sexually Transmitted Infections*, 74, 1, S12{S16, 1998.
17. Government of New Brunswick (GNB). Public Information Fact Sheet Gonorrhea, 2010.
18. J. Güémez and M.A. Matias. Control of chaos in unidimensional maps. *Physics Letters A*, 181, 1, 29{32, 1993.

19. K.P. Haderler and I. Gerstmann. The discrete Rosenzweig model. *Mathematical Biosciences*, 98, 1, 49{72, 1990.
20. H.W. Hethcote and J.A. Yorke. *Gonorrhea Transmission Dynamics and Control*. Heidelberg: Springer, 1984.
21. E.I. Jury. *Inners and Stability of Dynamic Systems*. Wiley, New York, 1974.
22. A. Lajmanovich and J.A. Yorke. A deterministic model for gonorrhea in a nonhomogeneous population. *Mathematical Biosciences*, 28, 3-4, 221{236, 1976.
23. J. Li, J. Lou and M. Lou. Some discrete SI and SIS epidemic models. *Applied Mathematics and Mechanics*, 29, 1, 113{119, 2008.
24. P. Manneville and Y. Pomeau. Different ways to turbulence in dissipative systems. *Physica D*, 1, 2, 219{226, 1980.
25. J.M. Marrazzo, H.H. Handsfield and P.F. Sparling. *Neisseria gonorrhoeae*. In: G.L. Mandell, J.E. Bennett and R. Dolin. (Eds.) *Mandell, Douglas and Bennett's principles and practice of infectious diseases*. 7th ed., Churchill Livingstone, 2753{2770, 2010.
26. R. Nallaswamy and J.B. Shukla. Effects of dispersal on the stability of a gonorrhea endemic mode. *Mathematical Biosciences*, 61, 1, 63{72, 1982.
27. National Institute of Allergy and Infectious Diseases (NIAID). *Sexually transmitted diseases: 1980 status report*. NIH Publication, No. 81-2213, 1980.
28. A. Ramani, A.S. Carstea, R. Willox and B. Grammaticos. Oscillating epidemics: a discrete-time model. *Physica A*, 333, 278{292, 2004.
29. T.G. Scalia, A. Svensson, T. Asikainen and J. Giesecke. Some model based considerations on observing generation times for communicable diseases. *Mathematical Biosciences*, 223, 1, 24{31, 2010.
30. P. Shil, Y.K. Gurav, M.S. Chadha and A.C. Mishra. Transmission dynamics of novel influenza A/H1N1 2009 outbreak in a residential school in India. *Current Science*, 100, 8, 1177{1183, 2011.
31. W. Smith. What I Didn't Know About Sexual Health: Reflections From a New Perch. National Coalition of STD Directors (NCSD), RH Reality Check, April 15, 2010.
32. Syracuse. Onondaga County sees big outbreak of gonorrhea, Public health officials are investigating a sharp increase in gonorrhea in Onondaga County. November 29, 2012. (<http://www.syracuse.com>)
33. R.H. Tikkanen, J. Abellsson and M. Forsberg. UngKAB09 - Knowledge, attitudes and sexual practices among young people. Gothenburg University, Swedish, 2011.
34. H. Trottier and P. Philippe. *Deterministic Modeling of Infectious Diseases: Theory and Methods*. Internet Journal of Infectious Diseases, 1, 2, 2001.
35. I. Velicko and M. Unemo. Recent trends in gonorrhoea and syphilis epidemiology in Sweden: 2007 to 2011. *Eurosurveillance*, 17, 29, 2012.
36. L. Warner, K.M Stone, M. Macaluso, J.W. Buehler and H.D. Austin. Condom Use and Risk of Gonorrhea and Chlamydia: A Systematic Review of Design and Measurement Factors Assessed in Epidemiologic Studies. *Sexually Transmitted Diseases*, 33, 1, 36{51, 2006.
37. P.J. Wiesner and S.E. Thompson III. Gonococcal diseases. *Disease-a-Month*, 27, 5, 1{44, 1980.
38. Wisconsin Division of Public Health. *Gonorrhea (Neisseria gonorrhoeae)*. Disease Fact Sheet Series, Department of Health Services (DHS).
39. World Health Organization (WHO). *Global Prevalence and Incidence of Selected Curable Sexually Transmitted Infections: Overview and Estimates*. Geneva, 2001.
40. World Health Organization (WHO). Urgent action needed to prevent the spread of untreatable gonorrhoea. June 6, 2012. (http://www.who.int/mediacentre/news/notes/2012/gonorrhoea_20120606/en/index.html)

Nonlinear Self-organization Dynamics of a Metabolic Process of the Krebs Cycle

Valerii Grytsay¹, Iryna Musatenko²

¹ Bogolyubov Institute for Theoretical Physics, 14b, Metrolohichna Str., Kyiv 03680
(E-mail: vgrytsay@bitp.kiev.ua)

² Taras Shevchenko National University of Kyiv, Faculty of Cybernetics, Department of Computational Mathematics, 64, Volodymyrska Str., Kyiv, Ukraine
(E-mail: ivmusatenko@gmail.com)

Abstract. The present work continues studies of the mathematical model of a metabolic process of the Krebs cycle. We study the dependence of its cyclicity on the cell respiration intensity determined by the formation level of carbon dioxide. We constructed the phase-parametric characteristic of the consumption of a substrate by a cell depending on the intensity of the metabolic process of formation of the final product of the oxidation. The scenarios of all possible oscillatory modes of the system are constructed and studied. The bifurcations with period doubling and with formation of chaotic modes are found. Their attractors are constructed. The full spectra of indices and divergencies for the obtained modes, the values of KS-entropies, horizons of predictability, and Lyapunov dimensions of strange attractors are calculated. Some conclusions about the structural-functional connections of the cycle of tricarboxylic acids and their influence on the stability of the metabolic process in a cell are presented.

Keywords: *Krebs cycle, metabolic process, self-organization, strange attractor, bifurcation, Feigenbaum scenario.*

1 Introduction

One of the possible problems of synergetics is the study of the internal dynamics of metabolic processes in cells. Its solution allows one to find the structural-functional connections defining the self-organization of these processes and to answer the question how the catalyzed enzymatic reactions create the internal space-time ordering of the cell life.

The most general metabolic process in cells is the cycle of tricarboxylic acids [1]. This is the key stage of the respiration of all cells. In its course, the di- and tricarbon compounds, which are formed as intermediate products in the transformation of carbohydrates, fats, and proteins, are transformed up to CO₂. In this case, the released hydrogen is oxidized further up to water, by taking the direct participation in the synthesis of ATP, being the universal energy source.

Studies of the functioning of the Krebs cycle were carried out both experimentally and theretically in [2-10].

7th CHAOS Conference Proceedings, 7-10 June 2014, Lisbon Portugal

C. H. Skiadas (Ed)

© 2014 ISAST



In the study of the given process, we use the mathematical model of the growth of cells *Candida utilis* on ethanol, which was developed by Professor V.P. Gachok [11, 12]. With the help of this model, the unstable modes in the cultivation of cells observed in experiments were considered. The kinetic curves of the chaotic dynamics obtained with the help of computational experiments were in agreement with experimental data [13].

Then the given model was modified and refined in [14] due to the account for the influence of the CO_2 level on the respiration intensity. With the help of the model, the structural-functional connections of the metabolic process in a cell, which cause the appearance of complicated oscillations in the metabolic process, were investigated. It was concluded that the given oscillations arise on the level of redox reactions of the Krebs cycle, reflect the cyclicity of the process, and characterize the self-organization in a cell. The fractality of the dynamics of oscillations of the Krebs cycle was studied as well.

The analogous oscillatory modes were observed in the processes of photosynthesis and glycolysis, variations of the calcium concentration in a cell, oscillations in heart muscle, and other biochemical processes [15-19].

2 Mathematical Model

The general scheme of the process is presented in Fig. 1. According to it with regard for the mass balance, we have constructed the mathematical model given by Eqs. (1) - (19).

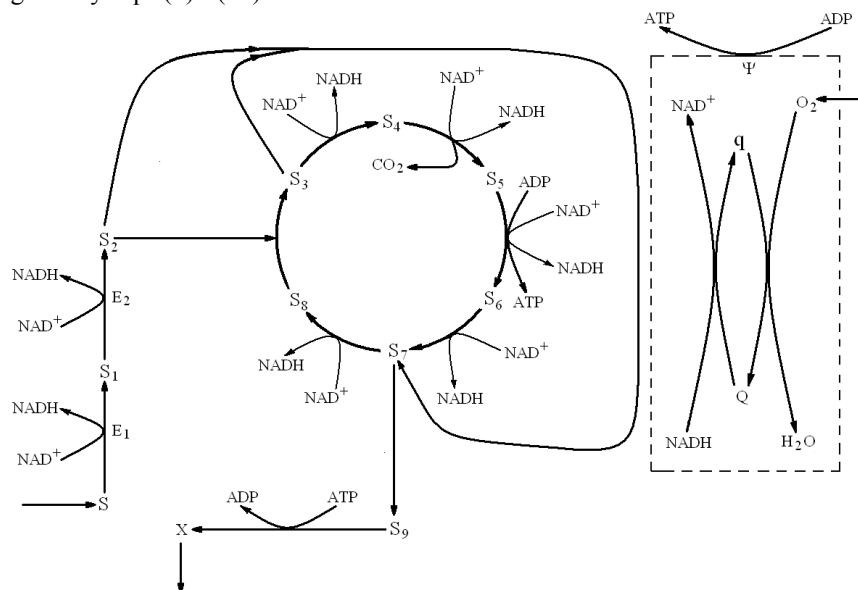


Fig. 1. General scheme of the metabolic process of growth of cells *Candida utilis* on ethanol.

$$\frac{dS}{dt} = S_0 \frac{K}{K+S+\gamma\psi} - k_1 V(E_1) \frac{N}{K_1+N} V(S) - \alpha_1 S, \quad (1)$$

$$\frac{dS_1}{dt} = k_1 V(E_1) \frac{N}{K_1+N} V(S) - k_2 V(E_2) \frac{N}{K_1+N} V(S_1), \quad (2)$$

$$\frac{dS_2}{dt} = k_2 V(E_2) \frac{N}{K_1+N} V(S_1) - k_3 V(S_2^2) V(S_3) - k_4 V(S_2) V(S_8), \quad (3)$$

$$\frac{dS_3}{dt} = k_4 V(S_2) V(S_8) - k_5 V(N^2) V(S_3^2) - k_3 V(S_2^2) V(S_3), \quad (4)$$

$$\frac{dS_4}{dt} = k_5 V(N^2) V(S_3^2) - k_7 V(N) V(S_4) - k_8 V(N) V(S_4), \quad (5)$$

$$\frac{dS_5}{dt} = k_7 V(N) V(S_4) - 2k_9 V(L_1 - T) V(S_5), \quad (6)$$

$$\frac{dS_6}{dt} = 2k_9 V(L_1 - T) V(S_5) - k_{10} V(N) \frac{S_6^2}{S_6^2 + 1 + M_1 S_8}, \quad (7)$$

$$\begin{aligned} \frac{dS_7}{dt} = & k_{10} V(N) \frac{S_6^2}{S_6^2 + 1 + M_1 S_8} - k_{11} V(N) V(S_7) - \\ & - k_{12} \frac{S_7^2}{S_7^2 + 1 + M_2 S_9} V(\psi^2) + k_3 V(S_2^2) V(S_3), \end{aligned} \quad (8)$$

$$\frac{dS_8}{dt} = k_{11} V(N) V(S_7) - k_4 V(S_2) V(S_8) + k_6 V(T^2) \frac{S^2}{S^2 + \beta_1} \cdot \frac{N_1}{N_1 + (S_5 + S_7)^2}, \quad (9)$$

$$\frac{dS_9}{dt} = k_{12} \frac{S_7^2}{S_7^2 + 1 + M_2 S_9} V(\psi^2) - k_{14} \frac{X T S_9}{(\mu_1 + T)[(\mu_2 + S_9 + X + M_3(1 + \mu_3 \psi))S]}, \quad (10)$$

$$\frac{dX}{dt} = k_{14} \frac{X T S_9}{(\mu_1 + T)[(\mu_2 + S_9 + X + M_3(1 + \mu_3 \psi))S]} - \alpha_2 X, \quad (11)$$

$$\frac{dQ}{dt} = -k_{15} V(Q) V(L_2 - N) + 4k_{16} V(L_3 - Q) V(O_2) \frac{1}{1 + \gamma_1 \psi^2}, \quad (12)$$

$$\frac{dO_2}{dt} = O_{2_0} \frac{K_2}{K_2 + O_2} - k_{16} (L_3 - Q) V(O_2) \frac{1}{1 + \gamma_1 \psi} - k_8 V(N) V(S_4) - \alpha_3 O_2, \quad (13)$$

$$\begin{aligned} \frac{dN}{dt} = & -k_7 V(N) V(S_4) - k_{10} V(N) \frac{S_6^2}{S_6^2 + 1 + M_1 S_8} - k_{11} V(N) V(S_7) - \\ & - k_5 V(N^2) V(S_3^2) + k_{15} V(Q) V(L_2 - N) - \\ & - k_2 V(E_2) \frac{N}{K_1 + N} V(S_1) - k_1 V(E_1) \frac{N}{K_1 + N} V(S), \end{aligned} \quad (14)$$

$$\begin{aligned}\frac{dT}{dt} = & k_{17}V(L_1 - T)V(\psi^2) + k_9V(L - T)V(S_3) - \alpha_4T - \\ & - k_{18}k_6V(T^2)\frac{S^2}{S^2 + \beta_1} \cdot \frac{N_1}{N_1 + (S_5 + S_7)^2} - \\ & - k_{19}k_{14}\frac{XTS_9}{(\mu_1 + T)[\mu_2 + S_9 + X + M_3(1 + \mu_3\psi)S]},\end{aligned}\quad (15)$$

$$\begin{aligned}\frac{d\psi}{dt} = & 4k_{15}V(Q)V(L_2 - N) + 4k_{17}V((L_1 - T)V(\psi^2) - \\ & - 2k_{12}\frac{S_7^2}{S_7^2 + 1 + M_2S_9}V(\psi^2) - \alpha\psi,\end{aligned}\quad (16)$$

$$\frac{dE_1}{dt} = E_{1_0}\frac{S^2}{\beta_2 + S^2}\frac{N_2}{N_2 + S_1} - n_1V(E_1)\frac{N}{K_1 + N}V(S) - \alpha_5E_1, \quad (17)$$

$$\frac{dE_2}{dt} = E_{2_0}\frac{S_1^2}{\beta_3 + S_1^2}\frac{N_3}{N_3 + S_2} - n_2V(E_2)\frac{N}{K_1 + N}V(S_1) - \alpha_6E_2, \quad (18)$$

$$\frac{dC}{dt} = k_8V(N)V(S_4) - \alpha_7C. \quad (19)$$

where $V(X) = X/(1 + X)$ is the function that describes the adsorption of the enzyme in the region of a local coupling. The variables of the system are dimensionless [11, 12].

The internal parameters of the system are as follows:

$k_1 = 0.3$; $k_2 = 0.3$; $k_3 = 0.2$; $k_4 = 0.6$; $k_5 = 0.16$; $k_6 = 0.7$; $k_7 = 0.08$;
 $k_8 = 0.022$; $k_9 = 0.1$; $k_{10} = 0.08$; $k_{11} = 0.08$; $k_{12} = 0.1$; $k_{14} = 0.7$; $k_{15} = 0.27$;
 $k_{16} = 0.18$; $k_{17} = 0.14$; $k_{18} = 1$; $k_{19} = 10$; $n_1 = 0.07$; $n_2 = 0.07$; $L = 2$;
 $L_1 = 2$; $L_2 = 2.5$; $L_3 = 2$; $K = 2.5$; $K_1 = 0.35$; $K_2 = 2$; $M_1 = 1$; $M_2 = 0.35$;
 $M_3 = 1$; $N_1 = 0.6$; $N_2 = 0.03$; $N_3 = 0.01$; $\mu_1 = 1.37$; $\mu_2 = 0.3$; $\mu_3 = 0.01$;
 $\gamma = 0.7$; $\gamma_1 = 0.7$; $\beta_1 = 0.5$; $\beta_2 = 0.4$; $\beta_3 = 0.4$; $E_{1_0} = 2$; $E_{2_0} = 2$.

The external parameters determining the flow-type conditions are chosen as
 $S_0 = 0.05055$; $O_{2_0} = 0.06$; $\alpha = 0.002$; $\alpha_1 = 0.02$; $\alpha_2 = 0.004$; $\alpha_3 = 0.01$;
 $\alpha_4 = 0.01$; $\alpha_5 = 0.01$; $\alpha_6 = 0.01$; $\alpha_7 = 0.0001$.

The model covers the processes of substrate-enzymatic oxidation of ethanol to acetate, cycle involving tri- and dicarboxylic acids, glyoxylate cycle, and respiratory chain.

The incoming ethanol S is oxidized by the alcohol dehydrogenase enzyme E_1 to acetaldehyde S_1 (1) and then by the acetal dehydrogenase enzyme E_2 to acetate S_2 (2), (3). The formed acetate can participate in the cell metabolism and can be exchanged with the environment. The model accounts for this

situation by the change of acetate by acetyl-*CoA*. On the first stage of the Krebs cycle due to the citrate synthase reaction, acetyl-*CoA* jointly with oxalacetate S_8 formed in the Krebs cycle create citrate S_3 (4). Then substances $S_4 - S_8$ are created successively on stages (5)-(9). In the model, the Krebs cycle is represented by only those substrates that participate in the reduction of *NADH* and the phosphorylation $ADP \rightarrow ATP$. Acetyl-*CoA* passes along the chain to malate represented in the model as intramitochondrial S_7 (8) and cytosolic S_9 (10) ones. Malate can be also synthesized in another way related to the activity of two enzymes: isocitrate lyase and malate synthetase. The former catalyzes the splitting of isocitrate to succinate, and the latter catalyzes the condensation of acetyl-*CoA* with glyoxylate and the formation of malate. This glyoxylate-linked way is shown in Fig. 1 as an enzymatic reaction with the consumption of S_2 and S_3 and the formation of S_7 . The parameter k_3 controls the activity of the активность glyoxylate-linked way (3), (4), (8). The yield of S_7 into cytosol is controlled by its concentration, which can increase due to S_9 , by causing the inhibition of its transport with the participation of protons of mitochondrial membrane.

The formed malate S_9 is used by a cell for its growth, namely for the biosynthesis of protein X (11). The energy consumption of the given process is supported by the process $ATP \rightarrow ADP$. The presence of ethanol in the external solution causes the “ageing” of external membranes of cells, which leads to the inhibition of this process. The inhibition of the process also happens due to the enhanced level of the kinetic membrane potential ψ . The parameter μ_0 is related to the lysis and the washout of cells.

In the model, the respiratory chain of a cell is represented in two forms: oxidized, Q , (12) and reduced, q , ones. They obey the integral of motion $Q(t) + q(t) = L_3$.

A change of the concentration of oxygen in the respiratory chain is determined by Eq. (13).

The activity of the respiratory chain is affected by the level of *NADH* (14). Its high concentration leads to the enhanced endogenic respiration in the reducing process in the respiratory chain (parameter k_{15}). The accumulation of *NADH* occurs as a result of the reduction of NAD^+ at the transformation of ethanol and in the Krebs cycle. These variables obey the integral of motion $NAD^+(t) + NADH(t) = L_2$.

In the respiratory chain and the Krebs cycle, the substrate-linked phosphorylation of *ADP* with the formation of *ATP* (15) is also realized. The energy consumption due to the process $ATP \rightarrow ADP$ induces the biosynthesis of components of the Krebs cycle (parameter k_{18}) and the growth of cells on the substrate (parameter k_{19}). For these variables, the integral of motion

$ATP(t) + ADP(t) = L_1$ holds. Thus, the level of ATP produced in the redox processes in the respiratory chain $ADP \rightarrow ATP$ determines the intensity of the Krebs cycle and the biosynthesis of protein.

In the respiratory chain, the kinetic membrane potential ψ (16) is created under the running of reducing processes $Q \rightarrow q$. It is consumed at the substrate-linked phosphorylation $ADP \rightarrow ATP$ in the respiratory chain and the Krebs cycle. Its enhanced level inhibits the biosynthesis of protein and process of reduction of the respiratory chain.

Equations (17) and (18) describe the activity of enzymes E_1 and E_2 , respectively. We consider their biosynthesis (E_{1_0} and E_{2_0}), the inactivation in the course of the enzymatic reaction (n_1 and n_2), and all possible irreversible inactivations (α_5 and α_6).

Equation (19) is related to the formation of carbon dioxide. Its removal from the solution into the environment (α_7) is taken into account. Carbon dioxide is produced in the Krebs cycle (5). In addition, it squeezes out oxygen from the solution (13), by decreasing the activity of the respiratory chain.

The study of solutions of the given mathematical model (1)-(19) was performed with the help of the theory of nonlinear differential equations [20, 21] and the methods of mathematical modeling of biochemical systems applied and developed by the authors. in [22-38].

3 The results of Studies

For one cycle, there occurs the full oxidation of a molecule of acetyl- CoA up to malate and the formation of a new molecule of acetyl- CoA at the input. In such a way, the continuous process of functioning of the Krebs cycle is running. This process has the autooscillatory character.

The studies of the model with the help of computational experiments showed that if system's parameters vary, the appearance of autooscillations with various frequencies, as well as chaotic oscillations, becomes possible. Oscillations with the same frequency will occur in all components of the given metabolic process. In the present work, we will study the dependence of autooscillations of the system on the parameter k_8 , which determines the level of formation of CO_2 in the cycle of tricarboxylic acid.

The different types of obtained autooscillatory modes are studied with the help of the construction of phase-parametric diagrams. The abscissa axis shows the values of parameter k_8 , and the axis of ordinates gives the values of chosen variable $E_1(t)$, for example. Moreover, we used the method of cutting. In the phase space of trajectories of the system, we place the cutting plane $S_2 = 0.8$. Such a choice is explained by the symmetry of oscillations of acetate relative to this plane in a lot of earlier calculated modes. For every given value of k_8 , we

observe the intersection of this plane by the trajectory in a single direction, when it approaches the attractor. The value of $E_1(t)$ is put onto the phase-parametric diagram. In the case where a multiple periodic limiting cycle arises, a number of points can be observed on the plane, and they will be the same in the period. If the deterministic chaos arises, the points of the intersection of the plane by the oscillating trajectory will be positioned chaotically.

In Fig. 2,a-d, we show the phase-parametric diagrams for the variable $E_1(t)$ versus the parameter k_8 changing in the appropriate intervals.

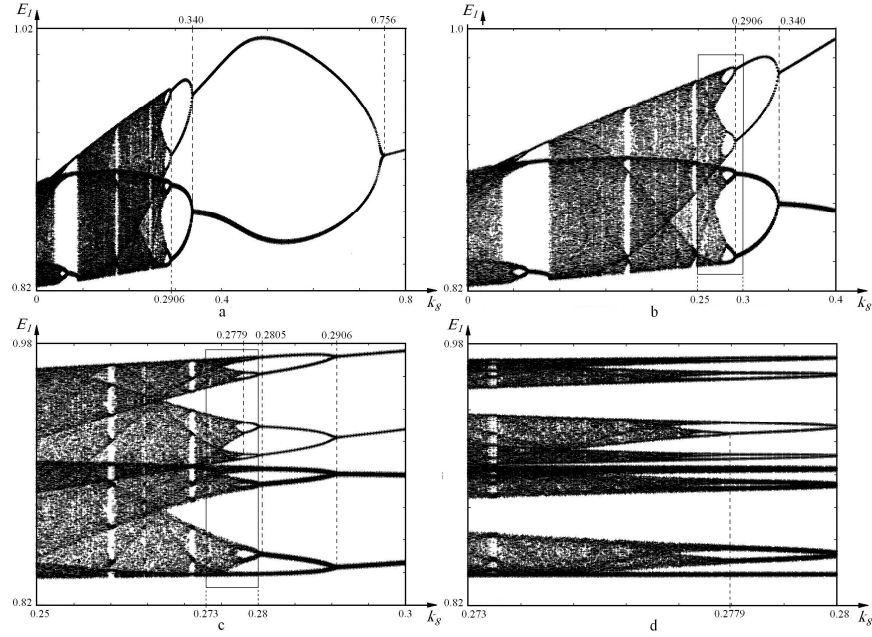


Fig. 2. Phase-parametric diagram for the variable $E_1(t)$: a - $k_8 \in (0, 0.8)$; b - $k_8 \in (0, 0.4)$; c - $k_8 \in (0.25, 0.3)$; d - $k_8 \in (0.273, 0.28)$.

As the parameter k_8 decreases, there occurs the subsequent doubling of the multilocity of the autoperiodic process. Such a sequence of the appearance of bifurcations creates a cascade of bifurcations, namely the Feigenbaum sequence [39]. After the multiple doubling of a period, the modes of aperiodic oscillations are eventually observed in the system. In other words, a chaos arises. As the parameter k_8 decreases further, we see the appearance of the windows of periodicity on the phase-parametric diagrams. The deterministic chaos is destroyed, and the periodic and quasiperiodic modes are established. The trajectory of a strange attractor in the chaotic mode is tightened to a regular attractor of the autoperiodic mode. We observe the self-organization in the system. Then the windows of periodicity are destroyed, and the chaotic modes arise again. Moreover, the transitions “order—chaos” and “chaos—order”

happen. There occurs the adaptation of the metabolic process to varying conditions.

It is seen from the presented figures that, as the scale decreases, every subsequent phase-parametric diagram with doubling of a cycle and its windows of periodicity are identical to those of the previous diagram, as the scale decreases. The given sequence of bifurcations has a self-similar fractal structure.

In Figs. 3,e-f and 4, we present the examples of the projections of phase portraits for some values of parameter k_8 , according to the phase-parametric diagram in Fig. 2.

In Fig. 5, we show the constructed kinetic curves for a strange attractor formed at $k_8 = 0.12$.

These figures indicate a variation of the dynamics of a metabolic process of the Krebs cycle, which depends on the intensity of formation of the final oxidation product, CO_2 .

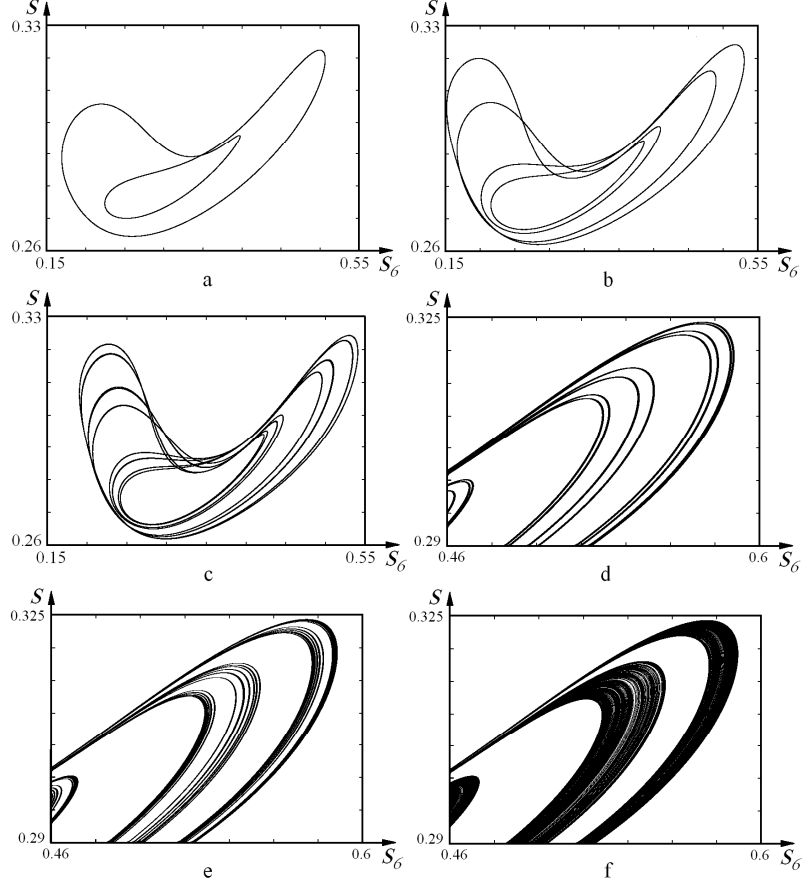


Fig. 3. Projections of system's phase portraits: a – regular attractor $2 \cdot 2^1$, $k_8 = 0.5$; b – regular attractor $2 \cdot 2^2$, $k_8 = 0.3$; c - regular attractor $2 \cdot 2^4$, $k_8 = 0.28$; d - regular attractor $2 \cdot 2^8$, $k_8 = 0.278$; e - regular attractor $2 \cdot 2^{16}$, $k_8 = 0.277$; f - strange attractor $2 \cdot 2^x$, $k_8 = 0.275$.

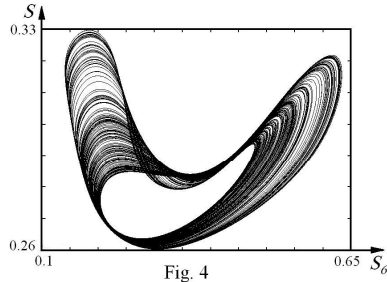


Fig. 4. Projection of the phase portrait of the strange attractor $2 \cdot 2^x$ for $k_8 = 0.12$.

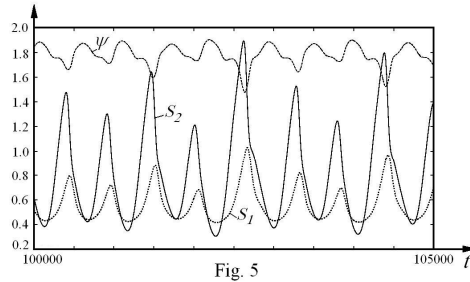


Fig. 5. Kinetic curve for the components S_1 , S_2 , and ψ of the Krebs cycle in the mode of the strange attractor $2 \cdot 2^x$ for $k_8 = 0.12$.

In order to uniquely identify the type of obtained attractors and to determine their stability, we calculated the full spectra of Lyapunov indices and their sum $\Lambda = \sum_{j=1}^{19} \lambda_j$ for the chosen points. The calculation was carried out by

Benettin's algorithm with the orthogonalization of the vectors of perturbations by the Gram-Schmidt method [21].

The calculation of Lyapunov indices from this multidimensional system on a personal computer meets certain difficulties. The mathematical model of the given biochemical system contains many variables and parameters. The limitations in the solution of such problems arise due to the insufficient random-access memory of a computer in the processing of the $n \times n$ matrix of small perturbations. In addition, any inaccuracy on the stage of programming will essentially affect the redefinition of the vectors of perturbations, their orthogonalization, and, as a consequence, the result of calculations. Nevertheless, we solved the problem and obtained certain results. Below for the sake of comparison, we present the spectra of Lyapunov indices for some modes of the system. For brevity without any loss of information, we give the values of indices up to the fourth decimal point.

The ratios of the values of Lyapunov indices $\lambda_1 > \lambda_2 > \lambda_3 > \dots > \lambda_{19}$ serve as the criterion of the validity of calculations. For a regular attractor, we have obligatorily $\lambda_1 \approx 0$. The remaining indices can be also ≈ 0 in some cases. In

some other cases, they are negative. The zero value of the first Lyapunov index testifies to the presence of a stable limiting cycle.

For a strange attractor, at least one Lyapunov index must be positive. After it, the zero index follows. The next indices are negative. The presence of negative indices means the contraction of system's phase space in the corresponding directions, whereas the positive indices indicate the dispersion of trajectories. Therefore, there occurs the mixing of trajectories in narrow places of the phase space of the system, i.e., there appears the deterministic chaos. The Lyapunov indices contain obligatorily the zero index, which means the conservation of the aperiodic trajectory of an attractor in some region of the phase space and the existence of a strange attractor.

For $k_8 = 0.01$, the strange attractor $2 \cdot 2^x$ arises. We have $\lambda_1 - \lambda_{19}$: .0007; .0000; -.0040; -.0125; -.0196; -.0200; -.0290; -.0299; -.0317; -.0416; -.0416; -.0416; -.0458; -.0816; -.0874; -.0874; -.1181; -.1539; -.2222; $\Lambda = -1.0672$.

For $k_8 = 0.075$ – regular attractor $3 \cdot 2^0$ (see the window of periodicity in Fig. 2,b). $\lambda_1 - \lambda_{19}$: .0000; -.0004; -.0040; -.0117; -.0194; -.0211; -.0285; -.0285; -.0326; -.0406; -.0406; -.0406; -.0451; -.0819; -.0883; -.0883; -.1182; -.1563; -.2241; $\Lambda = -1.0702$.

For $k_8 = 0.12$ – strange attractor $2 \cdot 2^x$; $\lambda_1 - \lambda_{19}$: .0008; .0000; -.0040; -.0125; -.0192; -.0210; -.0287; -.0300; -.0324; -.0406; -.0406; -.0406; -.0457; -.0822; -.0879; -.0879; -.1172; -.1542; -.2212; $\Lambda = -1.0653$.

For $k_8 = 0.27$ – strange attractor $2 \cdot 2^x$; $\lambda_1 - \lambda_{19}$: .0002; .0000; -.0040; -.0125; -.0192; -.0219; -.0281; -.0310; -.0320; -.0387; -.0387; -.0387; -.0436; -.0842; -.0889; -.0889; -.1185; -.1541; -.2209; $\Lambda = -1.0638$.

For $k_8 = 0.275$ – strange attractor $2 \cdot 2^x$; $\lambda_1 - \lambda_{19}$: .0001; .0000; -.0040; -.0125; -.0192; -.0219; -.0280; -.0312; -.0323; -.0383; -.0383; -.0383; -.0434; -.0842; -.0890; -.0890; -.1184; -.1540; -.2212; $\Lambda = -1.0631$.

For $k_8 = 0.278$ – regular attractor $2 \cdot 2^8$; $\lambda_1 - \lambda_{19}$: .0000; .0000; -.0041; -.0123; -.0193; -.0219; -.0283; -.0308; -.0320; -.0384; -.0384; -.0384; -.0435; -.0842; -.0890; -.0890; -.1187; -.1538; -.2212; $\Lambda = -1.0634$.

For $k_8 = 0.278$ – regular attractor $2 \cdot 2^8$; $\lambda_1 - \lambda_{19}$: .0000; .0000; -.0041; -.0123; -.0193; -.0219; -.0283; -.0308; -.0320; -.0384; -.0384; -.0384; -.0435; -.0842; -.0890; -.0890; -.1187; -.1538; -.2212; $\Lambda = -1.0634$.

For $k_8 = 0.28$ – regular attractor $2 \cdot 2^4$; $\lambda_1 - \lambda_{19}$: .0000; .0000; -.0041; -.0123; -.0193; -.0219; -.0282; -.0307; -.0322; -.0384; -.0384; -.0384; -.0436; -.0842; -.0890; -.0890; -.1186; -.1540; -.2212; $\Lambda = -1.0633$.

The presented results of calculations indicate that the sum Λ of all indices, which determine the flow divergencies and, hence, the evolution of the phase volume along the trajectory, is maximal for the regular attractor $3 \cdot 2^0$. It arises

in the window of periodicity for $k_8 = 0.075$ ($\Lambda = -1.0702$). For the strange attractors on the left and on the right (for $k_8 = 0.01$ and $k_8 = 0.12$), the divergencies are, respectively, $\Lambda = -1.0672$ and $\Lambda = -1.0653$. This means that the phase volume element for the given attractor is contracted, on the whole, stronger along the trajectory. Here, we observe the self-organization of a stable cycle from chaotic modes. The Krebs cycle is adapted to the varying conditions.

By the given Lyapunov indices for strange attractors, we determine the KS-entropy (the Kolmogorov--Sinai entropy) [40]. By the Pesin theorem [41], the KS-entropy h corresponds the sum of all positive Lyapunov characteristic indices:

The KS-entropy allows us to judge about the rate, with which the information about the initial state of the system is lost. The positivity of the given entropy is a criterion of the chaos. This gives possibility to qualitatively estimate the properties of attractor's local stability.

We determine also the quantity inverse to the KS-entropy, t_{\min} . This is the time of a mixing in the system. It characterizes the rate, with which the initial conditions will be forgotten. For $t \ll t_{\min}$, the behavior of the system can be predicted with sufficient accuracy. For $t > t_{\min}$, only a probabilistic description is possible. The chaotic mode is not predictable due to the loss of the memory of initial conditions. The quantity t_{\min} is called the Lyapunov index and characterizes the "predictability horizon" of a strange attractor.

In order to classify the geometric structure of strange attractors, we calculated the dimension of their fractality. The strange attractors are fractal sets and have the fractional Hausdorff-Besicovitch dimension. But its direct calculation is a very labor-consuming task possessing no standard algorithm. Therefore, as a quantitative measure of the fractality, we calculated the Lyapunov dimension of attractors by the Kaplan--Yorke formula [42, 43]:

$$D_{F_r} = m + \frac{\sum_{i=1}^m \lambda_i}{|\lambda_{m+1}|}, \quad (11)$$

where m is the number of the first Lyapunov indices ordered by their decreasing. Their sum $\sum_{i=1}^m \lambda_i \geq 0$, and $m+1$ is the number of the first Lyapunov index, whose value $\lambda_{m+1} < 0$.

For the above-considered strange attractors 2^∞ , we obtained the following indices.

For $k_8 = 0.01$: $h = 0.0007$, $t_{\min} = 1428.6$, $D_{F_r} = 2.175$.

For $k_8 = 0.12$: $h = 0.0008$, $t_{\min} = 1250$, $D_{F_r} = 2.2$.

For $k_8 = 0.27$: $h = 0.0002$, $t_{\min} = 5000$, $D_{F_r} = 2.05$.

For $k_8 = 0.275$: $h = 0.0001$, $t_{\min} = 10000$, $D_{F_r} = 2.025$.

By these indices, we can judge about the difference of the given strange attractors.

Conclusions

With the help of the mathematical model of the Krebs cycle, we have studied the dependence of the cyclicity of the metabolic process on the amount of a final product of the oxidation, i.e., on the amount of the formed carbon dioxide. The multiplicity of the cycle is doubled by the Feigenbaum scenario, until the aperiodic modes of strange attractors arise. From them as a result of the self-organization, the stable periodic modes appear. This means that the system is adapted to the varying conditions. We have calculated the full spectra of Lyapunov indices and the divergencies for various modes. For the strange attractors, we have determined the KS-entropies, “predictability horizons,” and Lyapunov dimensions of attractors. The results obtained allow us to study the structural-functional connections of the cycle of tricarboxylic acids, their influence on the cyclicity of metabolic oscillations in a cell, and the physical laws of self-organization in it.

The work is supported by the project No. 0113U001093 of the National Academy of Sciences of Ukraine.

References

1. H. A. Krebs and W. A. Johnson. The role of citric acid in intermediate metabolism in animal tissues. *Enzymologia*, 4, 148–156, 1937.
2. R. Bohnensack and E. E. Sel'kov. Stoichiometric regulation in the citric acid cycle. II. Non-linear interactions. *Studia biophysica*, 66, 47–63, 1977.
3. A. E. Lyubarev and B. I. Kurganov. Supermolecular organization of enzymes of the cycle of tricarboxylic acids. *Molek. Biol.*, 21, 5, 1286–1296, 1987.
4. M. N. Kondrashova. Structural kinetic organization of Supermolecular organization of enzymes of the cycle of tricarboxylic acids under the active functioning of mitochondria. *Biofiz.*, 34, 3, 450–457, 1989.
5. E. M. T. El-Mansi, G. C. Dawson and C. F. A. Bryce. Steady-state modelling of metabolic flux between the tricarboxylic acid cycle and the glyoxylate bypass in *Escherichia coli*. *Comput. Applic. Biosci.*, 10, 3, 295–299, 1994.
6. R. Ramakrishna, J.S. Edwards, A. McCulloch and B. O. Palsson. Flux-balance analysis of mitochondrial energy metabolism: consequences of systemic stoichiometric constraints. *Am. J. Physiol. Regul. Integr. Comp. Physiol.*, 280, 3, R695–R704, 2001.
7. S. Cortassa, M. A. Aon, E. Marban, R. L. Winslow and B. O'Rourke. An integrated model of cardiac mitochondrial energy metabolism and calcium dynamics. *Biophys. J.*, 84, 2734–2755, 2003.

8. K. Yugi and M. Tomita. A general computational model of mitochondrial metabolism in a whole organelle scale. *Bioinformatics*, 20, 1795–1796, 2004.
9. V. K. Singh and I. Ghosh. Kinetic modeling of tricarboxylic acid cycle and glyoxylate bypass in *Mycobacterium tuberculosis*, and its application to assessment of drug targets. *Theor. Biol. and Med. Model.*, 3, 27, 2006.
10. E. Mogilevskaya, O. Demin and I. Goryanin. Kinetic model of mitochondrial Krebs cycle: unraveling the mechanism of salicylate hepatotoxic effects. *J. of Biol. Phys.*, 32, 3-4, 245–271, 2006.
11. V. P. Gachok. *Kinetics of Biochemical Processes*, Naukova Dumka, Kiev, 1988 (in Russian).
12. V. P. Gachok. *Strange Attractors in Biosystems*, Naukova Dumka, Kiev, 1989 (in Russian).
13. W. B. Armiger, A. R. Moreira, J. A. Phillips and A. E. Humphrey. Modeling cellulose digestion for single cell protein. *Utilization of Cellulose Materials in Inconventional Food Production*, Plenum Press, New York, 1979, 111–117.
14. V. I. Grytsay and I. V. Musatenko. Self-organization and fractality in a metabolic processes of the Krebs cycle. *Ukr. Biokh. Zh.*, 85, 5, 191–199, 2013.
15. E. E. Selkov. Self-oscillations in glycolysis. *Europ. J. Biochem.*, 4, 79–86, 1968.
16. B. Hess and A. Boiteux. Oscillatory phenomena in biochemistry. *Annu. Rev. Biochem.*, 40, 237–258, 1971.
17. A. Goldbeter and R. Lefer. Dissipative structures for an allosteric model. Application to glycolytic oscillations. *Biophys J.*, 12, 1302–1315, 1972.
18. A. Goldbeter and R. Caplan. Oscillatory enzymes. *Annu. Rev. Biophys. Bioeng.*, 5, 449–476, 1976.
19. *Chaos in Chemical and Biochemical Systems*, edited by R. Field, L. Györgyi, World Scientific, Singapore, 1993.
20. V. S. Anishchenko. *Complex Oscillations in Simple Systems*, Nauka, Moscow, 1990 (in Russian).
21. S. P. Kuznetsov. *Dynamical Chaos*, Nauka, Moscow, 2001 (in Russian).
22. V. P. Gachok and V. I. Grytsay. Kinetic model of macroporous granule with the regulation of biochemical processes. *Dokl. Akad. Nauk SSSR*, 282, 51–53, 1985.
23. V. P. Gachok, V. I. Grytsay, A. Yu. Arinbasarova, A. G. Medentsev, K. A. Koshcheyenko and V. K. Akimenko. Kinetic model of hydrocortisone 1-en dehydrogenation by *Arthrobacter globiformis*. *Biotechn. Bioengin.*, 33, 661–667, 1989.
24. V. P. Gachok, V. I. Grytsay, A. Yu. Arinbasarova, A. G. Medentsev, K. A. Koshcheyenko and V. K. Akimenko. A kinetic model for regulation of redox reactions in steroid transformation by *Arthrobacter globiformis* cells. *Biotechn. Bioengin.*, 33, 668–680, 1989.
25. V. I. Grytsay. Self-organization in the macroporous structure of the gel with immobilized cells. Kinetic model of bioselective membrane of biosensor. *Dopov. Nats. Akad. Nauk Ukr.*, 2, 175–179, 2000.
26. V. I. Grytsay. Self-organization in a reaction-diffusion porous media. *Dopov. Nats. Akad. Nauk Ukr.*, 3, 201–206, 2000.
27. V. I. Grytsay. Ordered structure in a mathematical model biosensor. *Dopov. Nats. Akad. Nauk Ukr.*, 11, 112–116, 2000.
28. V. I. Grytsay. Self-organization of biochemical process of immobilized cells of bioselective membrane biosensor. *Ukr. J. Phys.*, 46, 1, 124–127, 2001.
29. V. V. Andreev and V. I. Grytsay. The modeling of nonactive zones in porous granules of a catalyst and in a biosensor. *Matem. Modelir.*, 17, 2, 57–64, 2005.

30. V. V. Andreev and V. I. Grytsay. Influence of heterogeneity of diffusion-reaction process for the formation of structures in the porous medium. *Matem. Modelir.*, 17, 6, 3–12, 2005.
31. V. I. Grytsay and V. V. Andreev. The role of diffusion in the active structures formation in porous reaction-diffusion media. *Matem. Modelir.*, 18, 12, 88–94, 2006.
32. V. I. Grytsay. Unsteady conditions in porous reaction-diffusion. *Medium. Romanian J. Biophys.*, 17, 1, 55–62, 2007.
33. V. I. Grytsay. The uncertainty in the evolution structure of reaction-diffusion medium bioreactor. *Biofiz. Visn.*, 2, 92–97, 2007.
34. V. I. Grytsay. Formation and stability of morphogenetic fields of immobilized cell in bioreactor. *Biofiz. Visn.*, 2, 25–34, 2008.
35. V. I. Grytsay. Structural instability of a biochemical process. *Ukr. J. Phys.*, 55, 5, 599–606, 2010.
36. V. I. Grytsay and I. V. Musatenko. Self-oscillatory dynamics of the metabolic process in a cell. *Ukr. Biochem. J.*, 85, 2, 93–104, 2013.
37. V. I. Grytsay and I. V. Musatenko. The structure of a chaos of strange attractors within a mathematical model of the metabolism of a cell. *Ukr. J. of Phys.*, 58, 7, 677–686, 2013.
38. V. I. Grytsay and I. V. Musatenko. A mathematical model of the metabolism of a cell. Self-organisation and chaos. Chaotic modeling and simulation. *CMSIM*, 4, 539–552, 2013.
39. M. J. Feigenbaum. Quantative universality for a class of nonlinear transformations. *J. Stat. Phys.*, 19, 1, 25–52, 1978.
40. A. N. Kolmogorov. On the entropy per unit time as a metric invariant of automorphisms. *DAN SSSR*, 154, 754–755, 1959.
41. Ya. B. Pesin. Characteristic Lyapunov indices and the ergodic theory. *Usp. Mat. Nauk*, 32, 4, 55–112, 1977.
42. J. L. Kaplan and J. A. Yorke. The onset of chaos in a fluid flow model of Lorenz. *Ann. N. Y. Acad. Sci.*, 316, 400–407, 1979.
43. J. L. Kaplan and J. A. Yorke. A chaotic behaviour of multidimensional differential equations. *Functional Differential Equations of Fixed Points*, edited by H. O. Peitgen, H. O. Walther, Springer, Berlin, 1979, 204–227.